Master's Thesis;

Bose-Einstein Condensates in an Optical Lattice

（光格子中のボース・アインシュタイン凝縮体の量子的振舞い）

Supervisor: Associate Professor Shin Inouye

Kai Noda

76524

Department of Applied Physics,
School of Engineering,
the University of Tokyo.

February, 2009

Dedicated to the memories of
^{87}Rb atoms
which were released from the dispenser,
captured in the MOT,
evaporatively cooled in the magnetic trap
until they Bose-Einstein condensed,
confined in the optical lattice,
shined by resonant light
to produce a shadow on the CCD,
and
dissapeared into the walls of the ion pumps.

謝辞 (Acknowledgements)

本論文は東京大学 工学系研究科 総合研究機構 井上研究室において行った研究をまとめたものです．何よりまず同研究室の主宰者である井上慎准教授に感謝します．井上先生は私を冷却原子の分野に導いて下さいました．私は学部 4 年で行う卒業研究の時点で初めて井上研究室に参加しましたが，参加して間もなくに冷却原子について井上先生から初めて習った知識は，光子の運動量と原子の遷移の自然幅を基にした MOT 中の原子の冷却レートの見積もりでした．以来，冷却原子の研究を通じて様々な知識と経験を蓄えることができましたが，それらはいずれも井上先生の導きによるものです．

また東京大学 理学系研究科の上田正仁教授にも感謝します．上田教授は JST, ERATO の上田マクロ量子制御プロジェクトの総括でおられ，井上研究室はそれを構成する一グループとして極低温極性分子生成を目指した実験を行っています．そのような時代の最先端を行く研究環境に身を置くことができたのは上田教授のご尽力のおかげです．またミーティング等を通じて上田教授から厳しくも示唆に富んだ指導をいただけたことは大きな財産となりました．

現在は電気通信大学 特任助教でおられる岸本哲夫博士には，岸本博士が井上研助手／助教でおられた時期から現在に至るまで，実験のあらゆる側面について多くを学ばせていただきました．ボール盤，旋盤，フライス盤の使用方法を始めとする私の金属加工の技能はいずれも岸本博士から習い，また岸本博士を目標として修練したものです．他にも挙げればきりがありませんが，そもそも本研究の実験を行う真空槽自体や，本研究の主題である光格子の光学系の配置が岸本博士の設計によるのを始め，手間のかかる光路の調整を効率化するための示唆等，本研究の多くを岸本博士に負うています．日頃から岸本博士の豊富な経験に基づく豊かな発想に触れることで優れた実験家たるには何を目指すべきか学ばせていただきました．

本研究を含む，私が井上研究室で行った実験の大部分は，現在の井上研助教でおられる小林淳博士の指導の下，BEC を扱う井上研究室 “E1” チームにおいて行われました．卒業研究生の頃に行った ^{39}K の飽和吸収分光から始め，岸本博士と共に行った翌夏の ^{41}K BEC の生成および翌春にかけての $|F = 1, m_F = 1\rangle$ 状態の ^{41}K 間の Feshbach 共鳴の観察，そして本研究に至るまで，いずれも小林博士と共に追求してきた結果です．当初はノートに実験系の設定パラメタを書き取る程度しかできませんでしたが，現在幾分なりとも系を把握して動かせるようになったのも，小林博士との研究活動を通じ揉まれたおかげです．実験上の困難を打開する糸口が見えない中でも様々な方策を提案する鋭い頭脳と，確固たる結果を求めて粘り強く実験に取り組む集中力には，常に驚嘆させられてきました．また両面テープがいかに実験系構築を簡略化するかについても学ばせていただきました．

学術振興会研究員として井上研究室に参加しておられた赤松大輔博士は量子光学のエキスパートでおられ，その最先端についての知識に触れることは，今だ多くの謎を湛える量子力学の本質に関し考えを深めるよい契機となりました．一見初等的な疑問をないがしろにせず追求する姿勢からは物理学徒の後輩として大いに薫陶を受けました．さらに埼玉県と浦和レッズに関する私の貧弱な理解を幾分か正していただきました．

現在，博士課程に所属し井上研究室で研究をなさっている 1 年先輩の相川清隆氏は，私が卒業研究生として立ち上げ間もなくの井上研究室に参加した時点よりやや早くから井上研究室で研究を行っておられました．当初から LD の準備や ^{39}K MOT 構築，また原子間ポテンシャルの計算においてたった 1 学年上とは思えぬ才覚を振るっていた様子を目にし，大学院生とはかくも水準が高い方々なのか，と衝撃を受けたのを記憶しています．相川氏の頭脳の回転の速さには圧倒されるばかりでしたが，そればかりでなく実験にも熱意と深い理解をもって取り組む姿を示していただくことで，気を引き締めて研究生活を送ることができました．

修士課程での同期生であった林正泰氏は井上研究室での所属チームこそ違うものの，物理を学ぶ学生としての苦楽を共にし，時おり根津の中華料理屋「楽翠荘」で夜食を取った同志でした．そして今も学生居室の

向かい合った席で修士論文を共に執筆しています．“E2” チームにおける分光実験や，それに引き続く分子の STIRAP において信号がノイズに埋もれ，そもそも広い範囲のどこに位置するのか分からないという逆境に置かれても，常に笑顔を絶やさない林氏の精神力は，共に過ごした 2 年間を通じ模範的なものとして私の目に映りました．それは今後も折に触れて思い出されることでしょう．

井上研究室での 1 年後輩である藤掛陽輔氏と山陸芳之氏は “E1” チームに対する熱意ある貢献振りで研究を加速させてくれました．藤掛氏は DDS を中核とする周波数生成・掃引システムの実装により，^{87}Rb BEC の実験をより完成度の高いものにしてくれました．第 3.5 節で触れたように，本研究でも ^{87}Rb 原子気体の蒸発冷却において当該システムを利用しています．山陸氏は勤勉な働きぶりで実験に不可欠な装置の構築に力を振るってくれました．^{87}Rb BEC 生成には各レーザーに対応して多数の AOM が必要とされますが，その制御回路の多くを山陸氏が製作してくれました．また本研究の次のステップに当たる，^{87}Rb-^{41}K 二原子種 BEC の効率的な光格子への閉じ込めに必要なパンケーキ形光双極子力トラップの実装に尽力してくれました．

2007 年度の卒業研究生として井上研に参加していた田野岡祐介氏，同じく 2008 年度の大島淳氏と森圭輔氏からは，溢れる若さのエネルギーを補充させていただきました．果たして私は，過去に私が知遇を得た方々のような良き先輩たり得たでしょうか？

上田マクロ量子制御プロジェクト 強相関量子制御グループのリーダーでおられる向山敬博士は，常に笑顔でハード・スケジュールの実験をこなす超人振りで，様子を横目で見ながら奮い立たせていただいたものです．また我々が現在光格子に使っているファイバ・レーザーの納品以前，向山グループ所有のファイバ・レーザーから数 W の出力を 40 m の光ファイバを通じて分けていただき，光学系のテストに使わせていただきました．他にも装置を融通していただくなど，多大な恩恵を受けました．

同グループの堀越宗一博士はアトムチップ上の BEC 干渉計に熟練した実験家でおられ，特に 1 次元光格子中の BEC に関してご自身の経験に基づく貴重な助言をいただきました．「s 波ハロー」についての議論は堀越博士からの助言が基になっています．また堀越博士にはしばしば 19 時前後に皆で夕食を食べに出かけるときのイニシアチブを取っていただきました．

同グループの Swarupananda Pradhan 博士からは 1 次元光格子中の原子の Kapitza-Dirac 散乱について，同グループにおける実験結果を基にアドバイスをいただきました．

同グループに参加なさっていた工学系研究科 五神研究室の稲田安寿氏は豊富な知識と豊かなユーモアを兼ね備えた尊敬すべき先輩でした．稲田氏は本研究と同時期に極低温 ^{6}Li 原子気体に関する博士論文を執筆しておられ，その姿を目標とさせていただきました．また稲田氏はしばしば我々の実験装置の置かれた奥の部屋を訪れ食事の誘いを伝えて下さいました．

同グループに参加なさっている理学系研究科 上田研究室の中島秀太氏からは冷却原子や超流動・超伝導の理論的側面について教えをいただきました．中島氏の修士論文は本論文の執筆において大いに参考とさせていただきました．またコヒーレンスの消失と復活に関し，ヘアスタイルを通じて示唆をいただきました．

上田マクロ量子制御プロジェクト 不確定性制御グループのリーダーでおられる東京工業大学の上妻幹旺准教授には定例ミーティング後や学生居室で議論に加わらせていただき，量子力学の基礎原理に関し様々な教えをいただきました．同時にそのフランクなお人柄にも感銘を受けました．また我々が現在 ^{87}Rb 原子の蒸発冷却に使っている 6.8 GHz 帯の rf 増幅器とスペクトラム・アナライザは上妻研究室からお借りしています．

同グループの竹内誠博士からは議論を通じ有益な情報をいただきました．本論文に関連する Mott 転移に関する私の理解の基礎となったのは竹内博士による講義でした．

現在は自然科学研究機構 分子科学研究所の助教でおられる武井宣幸博士からは，武井博士が同グループの研究員でいらした時期に量子光学の実験等に関し様々な教えをいただきました．

電気通信大学で冷却原子の実験をなさっている中川賢一准教授からも 6.8 GHz 帯の rf 増幅器をお借りしています．その rf 増幅器は我々の実験系における初の ^{87}Rb BEC 生成の鍵となりました．

上田マクロ量子制御プロジェクトの技術参事でおられる榎本陽一博士，また前任の技術参事でおられる金沢工業大学の山口敦史教授，同プロジェクト事務局の佐藤敏彦氏，塩田美奈子氏，国府田愛氏には研究の円滑な進行のためにご尽力いただきました．

最後に，両親に感謝します．

Contents

List of Figures

List of Tables

Chapter 1

Introduction

1.1 Historical overview

1.1.1 Developments of quantum many-body theory

In 1995, the first achievements of *Bose-Einstein Condensation* (BEC) in dilute atomic gases were reported almost simultaneously by three American groups (Anderson *et al.* [2], Davis *et al.* [3], Bradley *et al.* [4].) Since then, more and more atomic species have been cooled to reach quantum degeneracy (BEC for bosons and Fermi degeneracy for fermions.) Realization of BEC in a dilute atomic gas is often phrased as the "holy grail of physics," since it offers quite many opportunities in study of the quantum many-body systems. In order to appreciate its significance, we take a quick look at the history of the quantum theory of matters.

The efforts to study physical properties of solids and liquids (collectively termed as condensed matters) from the microscopic view of points dates back to the 1920's. At the turn of the 20th century, a completely novel branch of physics describing energy levels of electromagnetic radiations and atoms was born; quantum mechanics. Before its birth, the majority of physicists and mathematicians thought that physics is a "mature," or just "dead" branch of science. Ironically, among those scientists was Michelson, whose experimental work would later become the basis for the another revolution in physics; that is, the theory of relativity by Einstein (but we will not go further in this topic.) Feuer [5, Ch. 3] illustrates such an atomosphere by quoting memoirs by Millikan [6], who experienced the revolution in physics as a young physicist and himself made great contributions to it through measurement of the elementary charge:

> "My first view of Michelson was at the convocation [of the Ryerson Laboratory in 1894]. He gave the address on the place of very refined measurement in the progress of physics—an address in which he quoted someone else, I think it was Kelvin, as saying that it was probable that the great discoveries in physics had all been made, and that future progress was likely to be found in the sixth place of decimals."

However, the triumph of Bohr's atomic theory showed that there was large amount of problems to be investigated in the microscopic world. As shown in Table 1.1 (adapted from Brown *et al.* [7],) the "old" quantum theory, whose heart is Bohr's atomic theory based on simple quantization rule of electron orbits, successfully explained most of the phenomena found at that time with regard to atomic structure. Among them, the Stark shift, the (normal) Zeeman effect and the formation rule of periodic table of the elements are the most significant (the last one lead to finding of Pauli exclusion principle.) Note also that the basis for Bose-Einstein and Fermi-Dirac statistics was already found. However, as noticed by Pauli, the failure of Bohr theory in explanation of anomalous Zeeman effect had so deep root that the whole theory needed to be rebuild on a new solid foundation.

Schrödinger presented what is now called Schrödinger equation which describes time evolution of a wavefunction of a quantum state. It had a structure of wave equation, so his theory was called "wave mechanics." It correctly explained quantum phenomena discovered so far, including level structures of complex atoms such as sodium and the anomalous Zeeman effect. At the same time, Heisenberg formulated his quantum theory of electron orbits in terms of non-commuting position and momentum variables (at first defined in terms of Fourier coefficients.) With the help by Jordan, Born reformulated Heisenberg's theory into infinite-dimensional matrix algebra. Then their theory was called "matrix mechanics." Finally, Heisenberg realized that both of matrices and waves are representation of quantum states. That is, two formulations were equavalent. The success of unification of two different-looking theories convinced us the correctness of both of two theories.

Researcher	Year	Achievement
M. Planck	1900	Use of discrete energy levels in explaination of blackbody radiation spectrum
A. Einstein	1905	Introduction of "energy quanta" in explaination of the photoelectric effect
E. Rutherford	1910	Rutherford model of an atom consisting of a nucleus and orbiting electrons
N. Bohr	1913	Quantum theory of hydrogen energy spectrum; Bohr's quantization rule
J. Stark	1913	Observation of Stark shift
J. Franck and G. Hertz	1914	Franck-Hertz experiment of electron-atom inelastic scattering
P. Epstein / K. Schwarzschild	1916	Explanation of Stark shift in terms of Bohr theory
A. Einstein	1916	The concept of spontaneous emission
W. Kossel	1916	First trial to relate periodic table of the elements to Bohr theory
A. Sommerfeld / P. Debye	1916	Explanation of Zeeman[*1] effect in terms of Bohr theory
L. de Broglie	1923	The concept of matter waves
S. Bose	1924	Bose-Einstein stastistics of photons
A. Einstein	1925	Bose-Einstein statistics of massive particles; prediction of BEC for ideal bose gas
W. Pauli	1925	Pauli exclusion principle
C. J. Davisson / G. P. Thomson	1927	Electron beam diffraction

Table 1.1: Historical developments of "old" quantum theory ("pre-Schrödinger" era.) Their subject was electromagnetic radiation and energy structure of simple atoms, such as hydrogen. Note that this and subsequent tables slightly overlap in time.

Researcher	Year	Achievement
O. Stern and W. Gerlach	1922	Stern-Gerlach experiment of spin projection
G. Uhlenbeck and S. Goudsmit	1925	The concept of electron spin
W. Heisenberg	1925	Quantum theory in terms of non-commuting variables
M. Born and P. Jordan	1925	Reformulation of Heisenberg theory in terms of infinite-dimensional matrices
G. Uhlenbeck and S. Goudsmit	1925	The concept of electron spin

Table 1.2: Historical developments towards modern theory of quantum mechanics. The main subjects was energy structure of complex atoms. Formulations developed through these works endured the test of time and still plays the central role in modern physics.

As the correctness of quantum theory become more and more convincing, reseachers began to apply it to condensed matter systems. Matters should be in principle described by quantum mechanics, just like its ingredients, electrons and atoms. The application of quantum mechanics was first limited to one-body approximation. However, systematic approach to quantum many-body systems were gradualy developed. Recent topics attracting interests from many researchers are systems such that quantum nature of particles dominates the characteristics of the system.

In particular, a classical picture of matters breaks down if the phase space of the ensemble of particles is densely filled (see textbook by Leggett [8];) in other words, quantum mechanics becomes important in describing a many-body system if the *thermal de Broglie length* $\lambda_{\mathrm{dB}} \equiv h/\sqrt{2\pi m k_{\mathrm{B}} T}$ of particles is comparable or larger than the interparticle distance. In addition, we should take into account *indistinguishability* of particles and resultant *bosonic* and *fermionic statistics* if particles can exchange their positions and can overlap. In fact, in metals, that is the principal object in study of condensed matter systems, both of the above conditions are satisfied by electrons. Electrons in metals behave very much like an ideal degenerate Fermi gas (see classical monographs by Pines and Nozières [9, 10, 11].) They can move almost freely in a crystal, so statistical treatment is necessary. The density of electron gas is so high that they are almost always in a Fermi degeneracy. In fact, some of the properties of metals which could not be explained within the framework of classical physics were successfully understood by proper applications of quantum

mechanics. The first successes of quantum mechanics in condensed matters include derivation of the linear temperature dependence of the electronic heat capacity, and findings of the electronic band structure calculations of the kinetic coefficients in the transport phenomena, just to name a few.

However, as the research progresses, the novel form of the matter which did not allow application of simple quantum theory was discovered: the superfluidity in liquefied ^{4}He discovered by Kapitsa. For normal liquids at sufficiently low temperature T, the thermodynamic free energy $F = E - TS$ is minimized when kinetic energy E is minimized at the cost of low entropy S. However, ^{4}He atoms are so light that quantum fluctuations due to Heisenberg's uncertainty principle does not allow to form a crystalline structure. Although the ingenuity of Onsager captured its essence that the superfluidity is the result of BEC (1940), the high density of superfluid helium (or He-II) and resultant strong interactions between ^{4}He atoms prevented further theoretical investigations. Theoretical methods which successfully described its properties such as Ginzburg-Landau theory were to some extent phenomenological. There were Bogoliubov's theory for weak excitations of BEC, but it was not to meant to be a foundation of complete microscopic theory; it only predicts resultant various phenomena *provided* that macroscopic occupation will occur. Various methods based on perturbative techniques were developed, but they are hard to verify experimental agreements. In order to develop further understandings of the quantum nature of matter, reseachers dreamed of an ideal test bed for quantum many-body theories for long time.

The principal question is: how properties of a many-body system of interacting particles differ from those of non-interacting ones? First, ground state of each of them are different. Secondly, one may well look at elementary excitations from the ground states. They can be classifiend into two; that is, quasiparticles and collective modes. Moreover, one may hope to understand properties which are defined in thermal equilibrium states and are related to temperature of the system, or those whose manifestation are observed in irreversible phenomena to recover thermal equilibrium from inequilibrium states.

The historical remark was the BCS theory which describes a fermionic many-body system. Nextly, atomic nuclear theories accelerated its progress. Only a few phenomenology were known at that time, such as the shell-model describing the nuclear structure and a few kinds of collective modes of nucleons. However, applications of multiple scattering theory revealed the fact that strong short-range interactions between nucleons do not alter excitation spectra very much, and thus nucleons are best described as quasiparticles obeying the shell model. And findings in theories of superconductivity and electron gas were imported to the nuclear theory. Then collective modes were proved to occur from weak interaction between quasiparticles which originate from bare nucleons and interaction between them and are described by the shell model,

Lastly, theoretical models of many-body systems were developed to improve understandings of the essential characterics of many-body phenomena. Under appropriate assumptions, they give exact solutions whose analytic properties can be thoroughly investigated and be compared with experiments. An example is Tonks-Girardeau gas; a problem first raised for 1D classical bose gas by Tonks [12], and for quantum bose gas by Girardeau [13] more than 40 years ago. The physics of such a gas is dominated by the repulsive interactions between bosonic particles. Due to their mutual repulsion, the bosons cannot occupy the same position in space; thus the repulsive interaction between bosons is shown to have similar effect on the physics of the system as the Pauli exclusion principle for fermions (sometimes termed as "fermionization" of bosons.) As another example, we refer to the review by Tasaki [14] on mathematical results obtained for original (or, Fermi-) Hubbard model. A modified version of Hubbard model for bosons (Bose-Hubbard model) is also presented for superconducting currents in *Josephson Junction Arrays* (JJA) and it is also used for description of behavior of atoms confined in optical lattice. Lastly, we cite recent achievements in 2002 by Lieb and his coworkers which proved the existence of BEC in a weakly *interacting* (*i.e. non*-ideal) bose gas. For long time it has been believed that perturbation from ideal bosons works for interacting bosons, but no proof has been done before. However, starting from the expression of ground state energy for interacting bose gas, Note that, according to Baumgartner [15], there exists an interatomic potential such that its scattering length is positive and it can hold no two-body bound state, but leads to a many-body bound state. Such a complexity add a twist in the study of quantum many-body systems.

[*1] In fact, the phenomena observed by Zeeman was, in modern terminology, the anomalous Zeeman effect in which D1 and D2 lines of sodium split into four and six, respectively (Brown *et al.* [7].) However, Zeeman thought that the number of split lines was three. That erroneous observation accidentaly agreed well with the prediction based on the classical picture of motion of electrons and polarization of light. Later, Cornu correctly observed that the number of split lines was four, and the case in which splitting is more than three came to be termed as "anomalous" Zeeman effect. Today the case of three split lines is understood as a more special case than "anomalous" case, because such a splitting occurs only for atoms posessing electronic ground state with zero nuclear spin.

1.1.2 Quests for BEC in a dilute atomic gas

Here we look back at the history of quests for BEC in a dilute atomic gas, following Kleppner *et al.* [16]. In 1976, based on a phenomenology, Stwalley and Nosanow [17] predicted that a gas of spin-polarized hydrogen (H↑) might have a remarkable property in views of low temperature physics. Because there is no bound state in the triplet molecular potential between two H↑ atoms, a H↑ gas behaves like a simple monatomic gas. And because of the weak interaction between them and the atom's low mass, they would not liquefy even at absolute zero temperature. Consequently, it might be possible to cool H↑ to the quantum regime and achieve BEC. That paper essentially launched the search for BEC in an dilute atomic gas. Moreover, H↑ has three advantages over other atoms:

- BEC can be understood as overlapping of matter waves of atoms, whose scale of spacial length is thermal de Broglie length $\lambda_{\mathrm{dB}} \equiv h/\sqrt{2\pi m k_{\mathrm{B}} T}$. As it depends on the mass m of the atom as $m^{-1/2}$, use of the lightest atom H↑ is favorable.
- H↑ has anomalously small s-wave scattering length and thus can be regarded as a quite nearly ideal gas.
- The hydrogen plays a major role in fundamental physics as its energy structure can be calculated from first principle.

However, it was soon understood that the large dipolar loss in hydrogen gas was the major obstacle to cool hydrogen to reach BEC. Other reseachers began to seek other ways to cool atoms. In 1975, Hänsch and Schawlow [18] published the idea of laser cooling of neutral atoms, and in the same year, Wineland and Dehmelt [19] also published the same idea for trapped ions. Then it evolved into *Magneto-Optical Trap* (MOT) that not only cool atoms, but also trap them at the center of quadrupole magnetic field formed in free space. The first MOT was demonstrated by groups at Bell labs in 1987 (Raab *et al.* [20].) See Metcalf and van der Straten [21, Sec. 6.2 and 11.4], Weiner [22, Sec. 10.2] and references therein. Alkali and alkali earth atoms have only one electron in the outer shell, and thus have simple electronic energy structure. Laser cooling depends on repeated absorptions and spontaneous emissions of laser photons forming a closed cycle of electronic states, and thus the simple electronic energy structure is advantageous for other species. In fact, uses of so-called "repump" laser which put atoms which got out of the closed cycle again into the cycle are doable for them. However, the highest phase space density reachable by MOT is not enough to reach BEC. This is because a random walk of an atom caused by repeated scattering of photons balances at the velocity termed as Doppler velocity $v_{\mathrm{D}} \equiv \sqrt{\hbar\gamma/2m}$.

Thus one need another method for further cooling of atoms. The evaporative cooling, first proposed by Hess [23] in 1986, was soon demonstrated by the joint group of MIT and Bell labs in 1988 (Masuhara *et al.* [24].) So far all achievements of producing BEC in dilute atomic gases use evaporative cooling as the final step of the procedure.

After the first achievement of BEC, various kinds of its properties were investigated. Among them, the thermodynamic properties were the most basic. The agreement with theory was quite good for BEC of weakly interacting atoms. Collective modes which comes from interaction were also studied.

See Table 1.3 for list of the first achievements of quantum degeneracy for each atomic specie. Note that, most of them are alkalis and alkali earthes that have simple electronic energy structure and are suitable for laser cooling, but quantum degeneracy in other species is realized as well. The first success for a non-alkali atom is hydrogen[25] which was pre-cooled by a criogenic liquid helium chamber and then evaporatively cooled.

In 2003, reseachers at Innsbruck successfully produced BEC of ^{133}Cs (Weber *et al.* [26].) To circumvent the unwanted loss of atoms due to the atom's peculiar resonant scattering properties, they utilized Feshbach resonance (Chin *et al.* [27]) along with the usual optical trapping methods. The significance of cesium in modern physics and metrology is best understood when we look at atomic clocks. Modern atomic clocks that serve as frequency standard has cesium atoms in their heart to use its hyperfine transition as an oscillator. Currently the definition of second, established at the 13th meeting of CGPM[*1] in 1967 [28], is based on such cesium atomic clocks. Likewise, in 2007, Italian group successfully produced ^{39}K BEC (Roati *et al.* [29].) They circumvent problems due to the negative and small scattering length of ^{39}K ($-33\,a_0$) which leads to unstability of the condensate by utilizing Feshbach resonance (D'Errico *et al.* [30].) By inducing Feshbach resonance during evaporative cooling, they changed the scattering length to the large positive value ($150\,a_0$.) In fact, this is larger than that of ^{87}Rb, leading to a good efficiency of evaporative

[*1] CGPM (Conférence Générale des Poids et Mesures) is one of the three international organizations created by the Metre Convention.

Bosons

Isotope	Group	Year	N	n [cm^{-3}]	T [nK]
^{87}Rb	JILA and Colorado [2]	1995	2×10^3	2.5×10^{12}	170
^{7}Li	Rice [4, 31]	1995	1×10^5	3.7×10^{12}	300
^{23}Na	MIT [3]	1995	5×10^5	$> 10^{14}$	2000
^{1}H	MIT [25]	1998	1×10^9	4.8×10^{15}	5000
^{4}He*	Orsay [32]	2001	$> 5 \times 10^3$	10^{13}	160
^{41}K	LENS [33]	2001	1×10^4	6×10^{11}	160
^{133}Cs	Innsbruck [26]	2003	1.6×10^4	1.3×10^{13}	21
^{174}Yb	Kyoto [34]	2003	5×10^3	4.7×10^{14}	460
^{52}Cr	Stuttgart [35]	2005	5×10^4		700
^{170}Yb	Kyoto [36]	2007	1×10^4		200
^{39}K	LENS [29]	2007	3×10^4		100

Fermions

Isotope	Group	Year	N	n [cm^{-3}]	T/T_{F}
^{40}K	JILA and Colorado [37]	1995	7×10^5		0.5
^{6}Li	Rice [38]	1995	1×10^3	0.25	

Molecular BEC

Isotope	Group	Year
^{23}Na$_2$	MIT [39]	2003
^{6}Li$_2$	JILA, Colorado, and NIST [40]	2003

Table 1.3: Achievements of quantum degeneracy in a dilute atomic gas (mixture,) sorted by Year.

Homonuclear resonance

Isotope		Group	Year
Bosons	^{133}Cs	[27]	2000
	^{7}Li	[41, 42]	2002
	^{23}Na	[43]	1998
	^{85}Rb	[44]	1998
	^{87}Rb	[45]	2002
	^{52}Cr	[46]	2005
	^{41}K	[47]	2009
Fermions	^{6}Li	[48]	2002
	^{40}K	[49, 50]	2002

Heteronuclear resonance

	Isotopes	Group	Year
BF	^{85}Rb-^{87}Rb	[51]	2006
	^{7}Li- ^{87}Rb	[52]	2009
FF	^{6}Li- ^{40}K	Innsbruck, Amsterdam, Eindhoven, NIST, and Maryland [53]	2008

Table 1.4: Observations and theoretical predictions of Feshbach resonance in a dilute atomic gas (mixture,) sorted by Year.

cooling. Feshbach resonances observed for other atomic species such as also have similar possibilities to "tame" undesirable collisional properties for efficient evaporative cooling. Moreover, heteronuclear Feshbach resonances found for Bose-Fermi mixtures such as

1.1.3 Optical lattice: an ideal tool for simulating crystalline matters

The research of optical lattice was developed along with that of BEC. Various methods to form various kinds of periodic lattices are proposed using standing waves. See the reviews for "crystallography" of an optical lattice[54, 55]. Some of them have various advantages, such as insensitivity to phase fluctuations of the laser and approximate uniformness of the potential[56]. Moreover, an optical lattice can be used for cooling atoms[55, 57, 58] when combinated with optical methods producing dissipative force, such as PGC (polarization gradient cooling.)

Then two flows of researches combines as one; in 2002, the German groups announced their success in observation of the phase transition of dilute gas of atoms confined in an optical lattice. This is a mile-stone in the field of ultracold atoms, since this opens the way to simulate condensed matter systems in the real

world which consists of periodic lattice of ions and electrons spread inside it.

There are many possibilities for use of optical lattices exept for simulation of crystalline materials. For example, the variation of effective mass is observed in an optical lattice. Lastly, our group seeks the way towards the realization of ultracold polar molecules in the absolute (both electronic and rovibrational) ground state.

Our method goes as follows: first, we simultaneously create pure samples of ^{87}Rb and ^{41}K BECs by evaporative cooling in a magnetic trap. Then we adiabatically transfer them into a FORT (far-off-resonance optical dipole trap) to reduce their density to about 10^{13} cm^{-3}. Finally, we superimpose an optical lattice onto them. Here, the reduced densities of BEC assure unit filling factors of the lattice for each specie. Then we apply magnetic field to induce the heteronuclear Feshbach resonance to bind them into a single molecule. Such a kind of molecules, called *Feshbach molecules*, is not suitable for experiments in which interactions between electric dipole moments play dominant roles, because they are so shallowly bound that their electric dipole moments are small. Thus we use STIRAP (stimulated Raman adiabatic passage) to adiabatically transfer them into the absolute ground state. Note that, the fact mentioned above explains the need for an optical lattice during combination process by Feshbach resonance. Collisions between atoms and Feshbach molecules lead to dissociation of Feshbach molecules, since the kinetic energy of atoms in BEC is comparable (about tens of kilohertz times h, Planck constant) than the binding energy of Feshbach molecules (about hundreds of kilohertz.) Thus we need to confine BEC in the combined potential of a magnetic trap and an optical lattice to Then we will obtain a pure sample of BEC of ultracold polar molecules.

1.2 Contribution of this work

We constructed a 3D optical lattice which can be superimposed onto a mixture of ^{87}Rb and ^{41}K BECs in a magnetic trap. We used each axis of the 3D optical lattice as a 1D optical lattice to obtain interference patterns formed by a ^{87}Rb BEC released from the combined potential of the magnetic trap and the 1D optical lattice.

Moreover, we deepened the 1D optical lattice so that the interference patterns could be diminished and finally lost. This loss of the interference patterns may be attributed to suppression of tunneling of atoms between neighboring sites of the 1D optical lattice. We confirmed that the possibility of heating the atoms could be denied by shallowing the 1D optical lattice from the level at which there was no interference pattern, and then observing the recovery of the interference patterns. This assures that the whole procedure was done in an adiabatic manner.

Nextly, by using two of the three axes of the 3D optical lattice as a 2D optical lattice, we again obtained interference patterns that was 2D in this case. By adiabatic tuning of the depth of the 2D lattice, we observed similar loss of the interference pattern and its recovery.

These result suggests that the 3D optical lattice can be used to observe the superfluid to Mott insulator transition of ^{87}Rb BEC when we properly reduce the density of the BECs (an ongoing project in our group) and activate all axes of the 3D optical lattice simultaneously. Moreover, it can be adiabatically superimposed onto a mixture BEC of ^{87}Rb and ^{41}K that is already realized in our group so that for the mixture BEC with unit filling factors for each specie. Then we will be able to combine them into ultracold polar molecules in the absolute ground state using Feshbach resonance and STIRAP.

1.3 Structure of this thesis

First, the basic theoretical concepts are introduced (Chap. 2.) The main object of this field of research is an atom. Some formulas on interactions between an atom and electromagnetic fields used in subsequent sections are summarized (Sec. 2.1.) By cooling atomic gas, and thus reducing its degrees of freedom, we can observe a transition from the classical to the quantum degenerate state, namely, the Bose-Einstein condensation. Its properties relevant to our experiment are summarized (Sec. 2.2.) The macroscopic quantum nature of BEC is by itself so rich and attractive, but its significance in modern condensed matter physics can be much more enhanced by the combination with an optical lattice; that is why we choosen it as the main topic of this master's thesis. Physics governing a BEC in an optical lattice is explained, including important consequenses used in analysis of the experimental results (Sec. 2.3.)

Nextly, our experimental system is described (Chap. 3.) We describe the structure of our vacuum chamber, in which our experiments have been done (Sec. 3.1.) There we also describe a process to obtain ultra high vacuum to make a lifetime of the condensate long enough. As another basis of our experimental system, we describe optical system to provide frequency-locked lasers with various amounts of frequency

shift and having enough powers (Sec. 3.2.) We also describe our setup of MOT and the procedure of CMOT (Compressed MOT) for effective increase of phase space density (Sec. 3.3.) The procedure of optical pumping to prepare atoms in desirable spin states are also described there. After CMOT, further cooling of atomic cloud is done by rf-forced evaporative cooling. We use a magnetic trap in Ioffe-Pritchard configuration to confine atomic clouds. Its parameters and subsystems attached for various purposes are described (Sec. 3.4.) As its name suggests, rf-forced evaporative cooling needs rf (radio-frequency electromagnetic radiation) with a high power. The system to apply rf on atomic clouds are described (Sec. 3.5.) At the final stage of evaporative cooling, BEC is created and the optical lattice is superimposed on it. In order to suppress hopping of atoms between neighboring lattice sites, we need a deep potential. Our experiments heavily rely on visual image of the atomic cloud for measurement of its properties. The imaging system for absorption imaging of the cloud is described (Sec. 3.7.)

Then we describe our experimental results (Chap. 4.) Our final objective is creating ultracold polar molecules of ^{41}K-^{87}Rb and we are each step for its realization. Implementation of a 3D optical lattice is one step; and as one of other sub-goals, we created ^{41}K BEC.

Chapter 2

Theoretical Backgrounds

2.1 Interactions of Atoms and Electromagnetic Radiations

Here we summarize the theory of interaction of atoms and electromagnetic radiations which are relevant to use for the subsequent analysis of experiment results. Though one may work out in a fully quantum-mechanical treatment in which both atoms and electromagnetic waves are quantized and expressed as so-called "dressed" states, the semiclassical theory is known to give correct results (see, *e.g.* Grimm *et al.* [59].) So the following discussion is based on the semiclassical theory.

2.1.1 Optical Dipole Traps

To a first approximation, the interaction between a neutral atom and electric field $\boldsymbol{E}$ is the dipole interaction:

$$\Delta E = -\frac{1}{2}\boldsymbol{d}\cdot\boldsymbol{E}, \tag{2.1}$$

where $\boldsymbol{d}$ denotes the induced dipole of the atom. This energy shift ΔE is called (ac) Stark shift. Let α denote the polarizability of the atom: $\boldsymbol{d} = \alpha\boldsymbol{E}$. Assuming the classical model of an electron bound to the atomic nucleus by a harmonic potential, α generally depends on the driving frequency ω, and has complex value to describe absorption of photons by the atom. The energy shift ΔE, corresponding to the real part of α, give rise to the *optical dipole potential* U_{dip} felt by an atom. And the imaginary part corresponds to the *photon scattering rate* Γ_{sc}, which is the rate of spontaneous emission of a photon absorbed by the atom.

The expression for the depth of the dipole potential for the laser with intensity I is

$$U_{\mathrm{dip}}(I;\omega,\omega_X) = -\frac{3\pi c^2}{2\omega_X^3}\left(\frac{\Gamma}{\omega_X-\omega}+\frac{\Gamma}{\omega_X+\omega}\right)I, \tag{2.2}$$

where c is the speed of light, $\omega = 2\pi c/\lambda$ is the (angular) frequency[*1] of the laser of wavelength λ, ω_X is the resonant frequency of atom X (X = K or Rb in our case,) and Γ is the natural linewidth of that transition, which is the measure of expectation value of the dipole matrix element. The values of Γ are tabulated for major species[*2] and for alkali atoms, but the approximated value $\Gamma/2\pi \approx 6$ MHz usually suffices. Then we can use the well-known rotating-wave approximation in which $\Gamma/(\omega_X+\omega) \sim 10^{-8}$ is set to zero, obtaining

$$U_{\mathrm{dip}}(I;\omega,\omega_X) \approx \frac{3\pi c^2}{2\omega_X^3}\frac{\Gamma}{\Delta}I \equiv U_{\mathrm{dip}}(\omega,\omega_X)\cdot I. \tag{2.3}$$

Here, $\Delta \equiv \omega-\omega_X$ is the detuning of the laser frequency from the resonant frequency of the atom. From this definition of the detuning, we see that the red-detuned laser, for which the detuning is negative, creates an attracting potential for atoms. And in the last formula, we defined the propoptional coefficient $U_{\mathrm{dip}}(\omega,\omega_X)$ to separate dependence of the potential depth on ω from linear dependence on I.

Similarly, the expression for the photon scattering rate is

$$\begin{aligned}\Gamma_{\mathrm{sc}}(I;\omega,\omega_X) &= \frac{3\pi c^2}{2\hbar\omega_X^3}\left(\frac{\omega}{\omega_X}\right)^3\left(\frac{\Gamma}{\omega_X-\omega}+\frac{\Gamma}{\omega_X+\omega}\right)^2 I \approx \frac{3\pi c^2}{2\hbar\omega_X^3}\left(\frac{\omega}{\omega_X}\right)^3\frac{\Gamma^2}{\Delta^2}I \\ &\equiv \Gamma_{\mathrm{sc}}(\omega,\omega_X)\cdot I,\end{aligned} \tag{2.4}$$

[*1] We use s^{-1} as the unit of angular frequency and Hz as frequency. We also use s^{-1} as the unit of rate of events in probabilistic phenomena; Hz is only used for periodic phenomena.

[*2] See, *e.g.* Steck [60] for ^{87}Rb, ^{85}Rb, ^{23}Na, and ^{133}Cs. And see Gehm [61] and cLeBlanc [62] for ^{6}Li and ^{40}K, respectively.

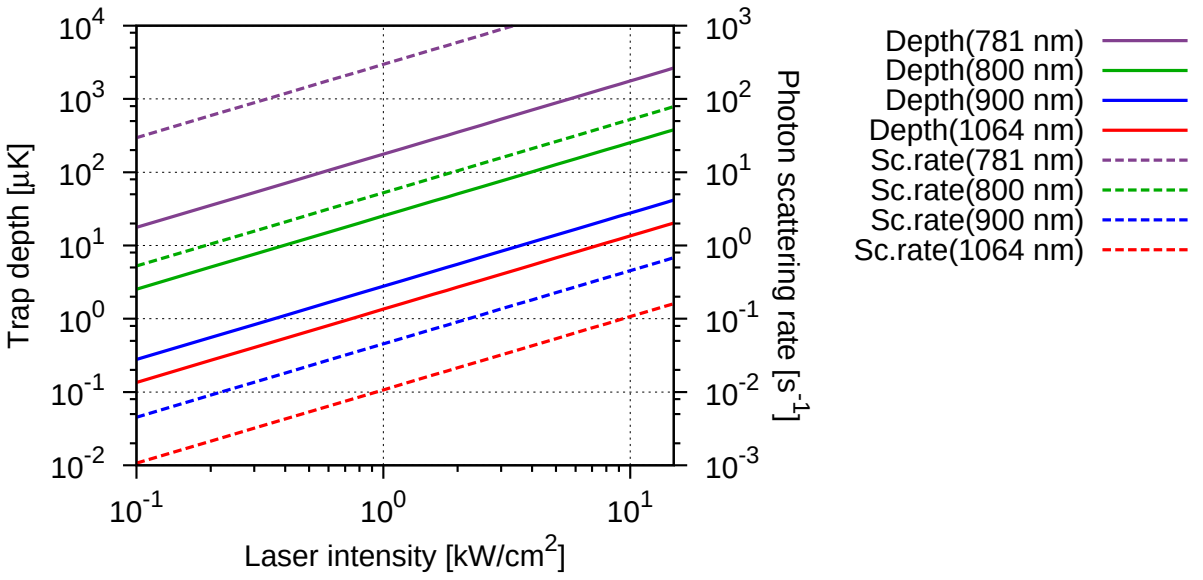

Figure 2.1: $U_{\rm dip}(I;\omega,{\rm Rb})$ and $\Gamma_{\rm sc}(I;\omega,{\rm Rb})$ plotted for several laser frequencies.

where we again used the rotating-wave approximation and separated linear dependence on I. The spontaneous emission is an incoherent process leading to the unwanted heating of the atomic cloud. In order to supress the photon scattering rate to the level at which it does no harm during experiments, we can use the far-detuned ($|\Delta| \gg \Gamma$) laser for the optical dipole traps. It is worthwhile to compare dependences of $U_{\rm dip}$ on Δ and I, and that of $\Gamma_{\rm sc}$:

$$U_{\rm dip} \propto \frac{I}{\Delta} \quad \text{vs.} \quad \Gamma_{\rm sc} \propto \frac{I}{\Delta^2}, \tag{2.5}$$

where ω/ω_X is approximated to unity. As $|\Delta|$ increases, $\Gamma_{\rm sc}$ decreases faster than $|U_{\rm dip}|$. Thus we can find the optimal point in the Δ-I plane at which $|U_{\rm dip}|$ is high enough (about 10 μK) and $\Gamma_{\rm sc}$ is low enough ($1/\Gamma_{\rm sc} \gg t_{\rm exp}$, where the length of experiment $t_{\rm exp}$ is about 0.1 s.) In Figure 2.1, we plotted the dependencies of $U_{\rm dip}(I;\omega,{\rm Rb})$ and $\Gamma_{\rm sc}(I;\omega,{\rm Rb})$ on laser intensity I for several values of laser frequencies $\omega = 2\pi c/\lambda$ corresponding to $\lambda = 781$, 800, 900, 1064 nm. Here we took into account of D_1 line (explained later,) though it does not significantly alter the shapes of the curves. We clearly see that the photon scattering rates (dashed lines) decays faster than the potential depth (solid lines) as we increase detuning from 781 nm to 1064 nm. Moreover, under the constraint that the photon scattering rate is kept at a constant value G, we can numerically solve $\Gamma_{\rm sc}(I;\omega,\omega_X) = G$ for ω to obtain laser frequency $\omega(I,G;\omega_X)$ which gives the necessary amount of detuning for that particular value of the photon scattering rate. The resultant function $U_{\rm dip}(I,G) \equiv U_{\rm dip}(I;\omega(I,G;\omega_X),\omega_X)$ is plotted in Figure 2.1 for $G = 0.1$ s^{-1} and $X =$ Rb. As we increase the intensity, we need larger (red) detuning, thus longer wavelength, to keep the photon scattering rate constant. But resultant depth of the optical dipole potential increases almost linearly with I in the region shown in the Figure.

For application to the trapping of alkali atoms, we need to take into account both of D_1 ($^2S_{1/2} \to {}^2P_{1/2}$) and D_2 ($^2S_{1/2} \to {}^2P_{3/2}$) transitions, because our optical lattice uses a far-detuned laser with wavelength of 1064 nm. The detuning is larger than the difference between the frequencies of two lines, as can be seen in Figure 2.3. In the figure, the lower and upper horizontal axis shows wavenumbers and corresponding wavelengths of transitions, respectively. The *area* of the bars indicates the relative intensity of observed signal with wavenumbers ranging from 9000 cm^{-1} to 17000 cm^{-1}, adapted from NIST database[63]. The largest and the second largest bars are D_2 and D_1 line, respectively. The vertical broken line shows the wavenumber of the optical lattice. We clearly see that both of the D_1 and D_2 lines have dominant contribution to optical dipole interaction potential of the optical lattice, and that contributions from other transitions are negligible. Other alkali atoms have similar wavenumbers for D_1 and D_2 transitions. Then the depth of the optical dipole trap with linear polarization is calculated from the following formula:

$$U_{\rm dip}(\omega, X) = \frac{\pi c^2}{2\omega_X^3}\left(\frac{2\Gamma}{\Delta_2} + \frac{\Gamma}{\Delta_1}\right), \tag{2.6}$$

where Δ_i denotes the detuning from the D_i line of the atom X. Here, the hyperfine structures of both the ground and the excited states are assumed to be unresolved because of the large detunings. For example,

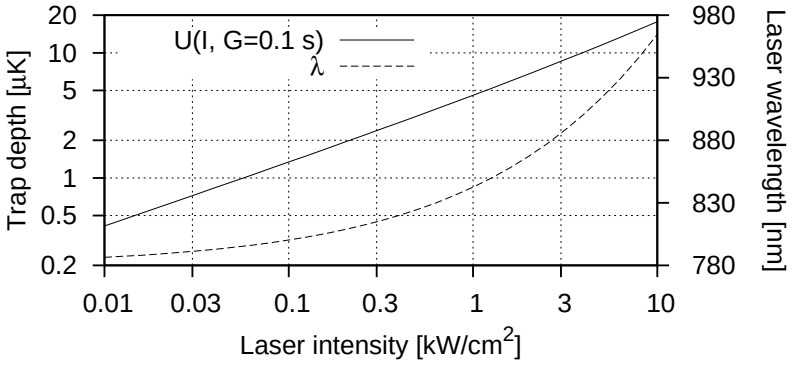

Figure 2.2: Plot of $\lambda(I) \equiv 2\pi c/\omega(I, G; \omega_X)$ and $U_{\rm dip}(I; G)$ for $G = 0.1$ s^{-1} and $X =$ Rb.

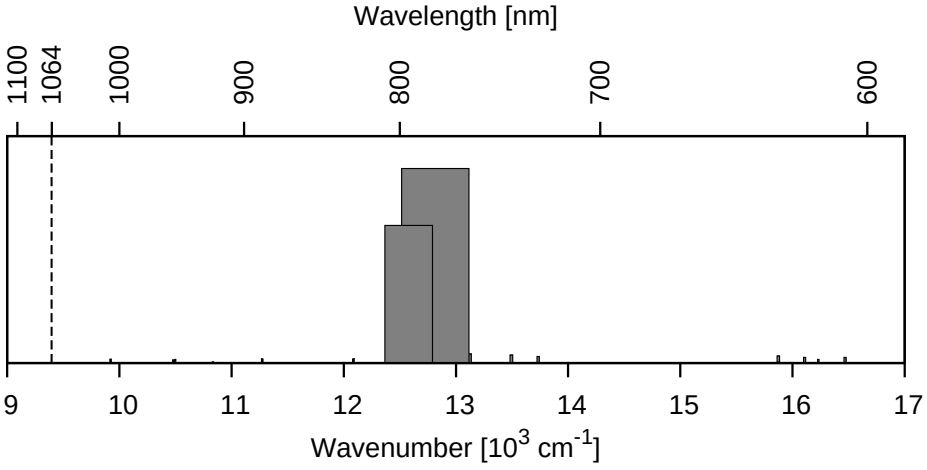

Figure 2.3: Schematic view of spectroscopic line data on ^{87}Rb known so far.

in the case of ^{87}Rb and the laser with wavelength of 1064 nm, we have

$$\frac{\Delta_2}{2\pi} = \frac{c}{1064\ \text{nm}} - \frac{c}{780\ \text{nm}} = (282 - 384)\ \text{THz} = -103\ \text{THz}, \tag{2.7}$$

$$\frac{\Delta_1}{2\pi} = \frac{c}{1064\ \text{nm}} - \frac{c}{795\ \text{nm}} = (282 - 377)\ \text{THz} = -95\ \text{THz}, \tag{2.8}$$

for respective lines (remember that negative values of Δ means red-detuning.) The two terms in brackets of eq. (2.6) represent the contributions of two lines to the total dipole potential. Likewise, the expression for the photon scattering rate is

$$\Gamma_{\rm sc}(\omega, X) = \frac{\pi c^2}{2\hbar\omega_X^3}\left(\frac{2\Gamma^2}{\Delta_2^2} + \frac{\Gamma^2}{\Delta_1^2}\right). \tag{2.9}$$

Assuming again the laser with wavelength $\lambda = 1064$ nm (corresponding to $\omega = 1.77 \times 10^{15}$ s^{-1},) we set

$$\begin{aligned} U_{\rm dip}^{(\rm Rb)} &\equiv U_{\rm dip}[(\omega, \omega_{\rm Rb,1}, \omega_{\rm Rb,2})/2\pi = (282, 377, 384)\ \text{THz}] \\ &= k_{\rm B} \cdot [4.45\ \mu\text{K}/(\text{W/cm}^2)] \quad = h \cdot [3.68\ \text{MHz}/(\text{W/cm}^2)] \quad = [46.2/(\text{W/cm}^2)] \cdot E_{\rm rec}^{(\rm Rb)}, \end{aligned} \tag{2.10a}$$

$$\begin{aligned} U_{\rm dip}^{(\rm K)} &\equiv U_{\rm dip}[(\omega, \omega_{\rm K,1}, \omega_{\rm K,2})/2\pi = (282, 389, 391)\ \text{THz}] \\ &= k_{\rm B} \cdot (4.01\ \mu\text{K/W}) \quad = h \cdot (3.31\ \text{MHz/W}) \quad = 19.6\, E_{\rm rec}^{(\rm K)} \end{aligned} \tag{2.10b}$$

For the definition of the recoil energy $E_{\rm rec}$, see Sec. 2.3.

2.1.2 Rabi frequency

Basics: Rabi frequency of the two-level system (without decay)

Here, we consider the two-level system coupled to a coherent monochromatic eletromagnetic wave. The wavefunction of the system $|\psi(t)\rangle$ is expressed by two time-dependent coefficients $c_{\rm g}(t)$ and $c_{\rm e}(t)$, whose square represent the probability of finding a system in the ground state $|{\rm g}\rangle$ or the excited state $|{\rm e}\rangle$, respectively; that is,

$$c_{\rm g}(t) \equiv \langle {\rm g}|\psi(t)\rangle, \qquad c_{\rm e}(t) \equiv \langle {\rm e}|\psi(t)\rangle. \tag{2.11}$$

We are going go use the time-dependent perturbation theory explained in App. A.2. The unperturbed Hamiltonian $\mathcal{H}_0$ is represented by the following matrix:

$$\mathcal{H}_0 = \begin{pmatrix} 0 & \\ & \hbar\omega_0 \end{pmatrix} \tag{2.12}$$

The upper-left zero means that we measure energies from that of the ground state $|{\rm g}\rangle$. The perturbation Hamiltonian V is represented by the following matrix:

$$V = \begin{pmatrix} & \hbar\Omega\cos(\omega t) \\ \hbar\Omega\cos(\omega t) & \end{pmatrix} \tag{2.13}$$

Here we used the so-called *electric dipole approximation* in which the spatial dependence is neglected in, *e.g.*,

$$\langle {\rm e}|V|{\rm g}\rangle = \langle {\rm e}|[\boldsymbol{\epsilon} E_0\cos(kz-\omega t)\cdot(-e\boldsymbol{r})]|{\rm g}\rangle \tag{2.14}$$

and thus

$$-eE_0\cos(\omega t)\boldsymbol{\epsilon}\cdot\langle {\rm e}|\boldsymbol{r}|{\rm g}\rangle = \hbar\Omega\cos(\omega t) \tag{2.15}$$

is used instead. Here, we defined the (one-photon) *Rabi frequency* Ω such that

$$\hbar\Omega \equiv -eE_0\boldsymbol{\epsilon}\cdot\langle {\rm e}|\boldsymbol{r}|{\rm g}\rangle. \tag{2.16}$$

Suppose that the two-level system under consideration is a hydgrogen atom. Then the numerical value for the Rabi frequency can be computed from the first principle. Denoting the wavefunctions of the $1\,^2{\rm S}_{1/2}$ state and the $2\,^2{\rm P}_{3/2}$ state by $\phi_{\rm g}(\boldsymbol{r})$ and $\phi_{\rm e}(\boldsymbol{r})$, respectively, we have

$$\langle {\rm e}|\boldsymbol{r}|{\rm g}\rangle = \int \phi_{\rm e}^*(\boldsymbol{r})\boldsymbol{r}\psi_{\rm g}(\boldsymbol{r})d\boldsymbol{r}. \tag{2.17}$$

However, we rarely do such a calculation and alwasy use the experimental value. The state vector $|\psi(t\rangle$ can be represented by the following 2-dimensional column vector:

$$|\psi(t)\rangle = \begin{pmatrix} \langle {\rm g}|\psi(t)\rangle \\ \langle {\rm e}|\psi(t)\rangle \end{pmatrix} = \begin{pmatrix} c_{\rm g}(t) \\ c_{\rm e}(t) \end{pmatrix}. \tag{2.18}$$

Then we go to the interaction picture. From Eq. (2.12), we have

$$e^{i\mathcal{H}_0 t/\hbar} = \begin{pmatrix} 1 & \\ & e^{i\omega_0 t} \end{pmatrix}. \tag{2.19}$$

Thus, in the interaction picture, the state vector $|\psi^{\rm I}(t)\rangle$ and the perturbation Hamiltonian $V^{\rm I}(t)$ is respectively represented as

$$|\psi^{\rm I}(t)\rangle = \begin{pmatrix} 1 & \\ & e^{i\omega_0 t} \end{pmatrix}\begin{pmatrix} c_{\rm g}(t) \\ c_{\rm e}(t) \end{pmatrix} = \begin{pmatrix} c_{\rm g}(t) \\ e^{i\omega_0 t}c_{\rm e}(t) \end{pmatrix} \equiv \begin{pmatrix} d_{\rm g}(t) \\ d_{\rm e}(t) \end{pmatrix}, \tag{2.20}$$

$$\begin{aligned} V^{\rm I}(t) &= \begin{pmatrix} 1 & \\ & e^{i\omega_0 t} \end{pmatrix}\begin{pmatrix} & \hbar\Omega\cos(\omega t) \\ \hbar\Omega\cos(\omega t) & \end{pmatrix}\begin{pmatrix} 1 & \\ & e^{-i\omega_0 t} \end{pmatrix} \\ &= \begin{pmatrix} & \hbar\Omega e^{-i\omega_0 t}\cos(\omega t) \\ \hbar\Omega e^{i\omega_0 t}\cos(\omega t) & \end{pmatrix}. \end{aligned} \tag{2.21}$$

Here, for each of $i = {\rm g}, {\rm e}$, we defined $d_i(t) \equiv e^{i\epsilon_i t/\hbar}c_i(t)$, where $\epsilon_i \equiv \langle i|\mathcal{H}_0|i\rangle$ is 0 for $|{\rm g}\rangle$ and $\hbar\omega_0$ for $|{\rm e}\rangle$. Moreover, we use the so-called *rotating-wave approximation* (RWA); that is, we neglect oscillating term with

a high frequency such as $e^i(\omega+\omega_0)$, as its frequency is so high that its effects is averaged out and it never have influence on physically observable quantities. We can do such an approximation for the matrix-element of $V^{\mathrm{I}}(t)$. For example, we have

$$e^{-i\omega_0 t}\cos(\omega t) = \frac{1}{2}\left[e^{i(\omega-\omega_0)t} + e^{-i(\omega+\omega_0)t}\right] \approx \frac{1}{2}e^{i(\omega-\omega_0)t} \equiv \frac{1}{2}e^{i\Delta t}. \tag{2.22}$$

Here, we defined the *detuning* Δ as $\Delta \equiv \omega - \omega_0$. Then the perturbation Hamiltonian can be written as

$$V^{\mathrm{I}}(t) \approx \frac{\hbar\Omega}{2}\begin{pmatrix} & e^{i\Delta t} \\ e^{-i\Delta t} & \end{pmatrix}. \tag{2.23}$$

Then the explicit solution of the coupled linear differential equations

$$i\hbar\partial_t|\psi^{\mathrm{I}}(t)\rangle = V^{\mathrm{I}}(t)|\psi^{\mathrm{I}}(t)\rangle \iff \begin{pmatrix}\dot{d}_{\mathrm{g}}(t)\\ \dot{d}_{\mathrm{e}}(t)\end{pmatrix} = -\frac{i\Omega}{2}\begin{pmatrix} & e^{i\Delta t} \\ e^{-i\Delta t} & \end{pmatrix}\begin{pmatrix} d_{\mathrm{g}}(t)\\ d_{\mathrm{e}}(t)\end{pmatrix}. \tag{2.24}$$

can be obtained by standard techniques. Here, we denote the time-derivative by the dot over a variable. First, we apply simple substitutions:

$$\begin{aligned}\ddot{d}_{\mathrm{e}}(t) &= -i\Delta\left[-\frac{i\Omega}{2}e^{-i\Delta t}d_{\mathrm{g}}(t)\right] - \frac{i\Omega}{2}e^{-i\Delta t}\dot{d}_{\mathrm{g}}(t) = -i\Delta\dot{d}_{\mathrm{e}}(t) - \frac{i\Omega}{2}e^{-i\Delta t}\cdot\left[-\frac{i\Omega}{2}e^{i\Delta t}d_{\mathrm{e}}(t)\right].\\ \therefore\ &\ddot{d}_{\mathrm{e}}(t) + i\Delta\dot{d}_{\mathrm{e}}(t) + \frac{\Omega^2}{4}d_{\mathrm{e}}(t) = 0.\end{aligned} \tag{2.25}$$

The uncoupled equation for $d_{\mathrm{g}}(t)$ is a second-order linear differential equation with constant coefficients. Thus it can be solved by looking at the characteristic equation:

$$\alpha^2 + i\Delta\alpha + \frac{\Omega^2}{4} = 0 \iff \alpha = -\frac{i}{2}\left(\Delta \pm \Omega'\right), \tag{2.26}$$

where we defined the *effective Rabi frequency* Ω' under the detuning Δ as $\Omega' \equiv \sqrt{\Omega^2+\Delta^2}$. Using the above α's, we can write down the general solution using two coefficients D_+ and D_-:

$$d_{\mathrm{e}}(t) = D_+e^{-i(\Delta+\Omega')t/2} + D_-e^{-i(\Delta-\Omega')t/2}. \tag{2.27}$$

The values of these two coefficients are determined by the initial conditions, typically at $t=0$. For example, we specify that $d_{\mathrm{g}}(0)=1$ and $d_{\mathrm{e}}(0)=0$; that is, all the population accumlates in the ground state. Then, using the latter condition, we have

$$d_{\mathrm{e}}(0) = D_+ + D_- = 0 \quad \therefore d_{\mathrm{e}}(t) = -2D_+e^{-i\Delta t/2}\sin\left(\frac{\Omega' t}{2}\right). \tag{2.28}$$

Then, using the former, we have

$$d_{\mathrm{g}}(0) = \frac{2i}{\Omega}e^{i\Delta t}\dot{d}_{\mathrm{e}}(t)\Big|_{t=0} = -\frac{2i}{\Omega}D_+\Omega' = 1 \quad \therefore D_+ = \frac{i}{2}\frac{\Omega}{\Omega'}. \tag{2.29}$$

Finally, we have

$$c_{\mathrm{e}}(t) = e^{-i\omega_0 t}d_{\mathrm{e}}(t) = -i\frac{\Omega}{\Omega'}e^{-i(\omega+\omega_0)t/2}\sin\left(\frac{\Omega' t}{2}\right), \tag{2.30a}$$

$$c_{\mathrm{g}}(t) = d_{\mathrm{g}}(t) = \frac{2i}{\Omega}e^{i\Delta t}\dot{d}_e(t) = e^{i\Delta t/2}\left(\cos\frac{\Omega'}{2}t - i\frac{\Delta}{\Omega'}\sin\frac{\Omega' t}{2}\right). \tag{2.30b}$$

Thus, the population of each state is as follows:

$$|c_{\mathrm{e}}(t)|^2 = \frac{\Omega^2}{\Omega^2+\Delta^2}\frac{1-\cos\Omega' t}{2}, \tag{2.31a}$$

$$|c_{\mathrm{g}}(t)|^2 = \frac{\Omega^2}{\Omega^2+\Delta^2}\frac{1+\cos\Omega' t}{2} + \frac{\Delta^2}{\Omega^2+\Delta^2} \tag{2.31b}$$

The dynamics of this system is illustrated in Metcalf and van der Straten [21]. Note that, though the population for each state goes back to the the initial state after the time of $2\pi/\Omega'$ passed, the wavefunction of the system acquires the extra factor of -1. This is the remarkable feature of the spin-1/2 system.

Note that, if we take into account of the decays from the excited states to lower states, then the process needs to be described by the density matrix, since the decay is an incoherent process and the resultant statistical mixture of the states cannot be written by a state vector in any Hilbert space. We do not discuss such cases; refer to the standard textbooks on quantum mechanics.

Advanced: Rabi frequency of the symmetric V-shaped system (without decay)

Now we calculate the three-level case. However, we restrict ourselves to the case of symmetric V-shaped structure. There are a ground state $|\mathrm{g}\rangle$ and two excited states $|\mathrm{e1}\rangle$ and $|\mathrm{e2}\rangle$ whose energies are degenerate. Let $\hbar\omega_0$ denote such energies. Then the unperturbed Hamiltonian $\mathcal{H}_0$ and perturbation Hamiltonian V are respectively represented as

$$\mathcal{H}_0 = \begin{pmatrix} \hbar\omega_0 & & \\ & 0 & \\ & & \hbar\omega_0 \end{pmatrix}, \tag{2.32a}$$

$$V = \begin{pmatrix} & \hbar\Omega\cos(\omega t) & \\ \hbar\Omega\cos(\omega t) & & \hbar\Omega\cos(\omega t) \\ & \hbar\Omega\cos(\omega t) & \end{pmatrix}, \tag{2.32b}$$

in the Schrödinger picture. Here, Ω again denotes the one-photon Rabi frequency. In the following, we see how the shape of the level structrue makes the effective Rabi frequency differs from Ω. From Eq. (2.32a), we have

$$e^{i\mathcal{H}_0 t/\hbar} = \begin{pmatrix} e^{i\omega_0 t} & & \\ & 1 & \\ & & e^{i\omega_0 t} \end{pmatrix}. \tag{2.33}$$

Thus, in the interaction picture, we have

$$|\psi^{\mathrm{I}}(t)\rangle = e^{i\mathcal{H}_0 t/\hbar}\begin{pmatrix} \langle \mathrm{e1}|\psi(t)\rangle \\ \langle \mathrm{g}|\psi(t)\rangle \\ \langle \mathrm{e2}|\psi(t)\rangle \end{pmatrix} = \begin{pmatrix} e^{i\omega_0 t} & & \\ & 1 & \\ & & e^{i\omega_0 t} \end{pmatrix}\begin{pmatrix} c_{\mathrm{e1}}(t) \\ c_{\mathrm{g}}(t) \\ c_{\mathrm{e2}}(t) \end{pmatrix} \equiv \begin{pmatrix} d_{\mathrm{e1}}(t) \\ d_{\mathrm{g}}(t) \\ d_{\mathrm{e2}}(t) \end{pmatrix}. \tag{2.34}$$

And the perturbation Hamiltonian is

$$\begin{aligned} V^{\mathrm{I}}(t) &= \begin{pmatrix} e^{i\omega_0 t} & & \\ & 1 & \\ & & e^{i\omega_0 t} \end{pmatrix}\begin{pmatrix} & \hbar\Omega\cos(\omega t) & \\ \hbar\Omega\cos(\omega t) & & \hbar\Omega\cos(\omega t) \\ & \hbar\Omega\cos(\omega t) & \end{pmatrix}\begin{pmatrix} e^{-i\omega_0 t} & & \\ & 1 & \\ & & e^{-i\omega_0 t} \end{pmatrix} \\ &= \hbar\Omega\begin{pmatrix} & e^{i\omega_0 t}\cos(\omega t) & \\ e^{-i\omega_0 t}\cos(\omega t) & & e^{-i\omega_0 t}\cos(\omega t) \\ & e^{i\omega_0 t}\cos(\omega t) & \end{pmatrix} \approx \frac{\hbar\Omega}{2}\begin{pmatrix} & e^{-i\Delta t} & \\ e^{i\Delta t} & & e^{i\Delta t} \\ & e^{-i\Delta t} & \end{pmatrix} \end{aligned} \tag{2.35}$$

Again, we used RWA in the last equation. Then we again try to solve the coupled linear differential equations with respect to $d_i(t)$'s ($i = \mathrm{g}$, e1, e2.) However, to simplify subsequent calculations, we assume the special initial condition: $d_{\mathrm{g}}(0) = 1$ and $d_{\mathrm{e1}}(0) = d_{\mathrm{e2}}(0) = 0$. Then the time-evolution is symmetric with respect to $i = \mathrm{e1}$ and e2. Thus we rename those coefficients as follows:

$$d_0(t) \equiv d_{\mathrm{g}}(t), \qquad d_1(t) \equiv d_{\mathrm{e1}}(t) = d_{\mathrm{e2}}(t). \tag{2.36}$$

Then the coupled differential equations are rather simplified:

$$\begin{pmatrix} \dot{d}_0(t) \\ \dot{d}_1(t) \end{pmatrix} = -\frac{i\Omega}{2}\begin{pmatrix} & 2e^{i\Delta t} \\ e^{-i\Delta t} & \end{pmatrix}\begin{pmatrix} d_0(t) \\ d_1(t) \end{pmatrix}. \tag{2.37}$$

It is worthwhile to compare the above quation with Eq. (2.24). The factor of two in the matrix element appears because there are in fact two final states for the transition *from* the ground state. Solving the coupled equations with the above initial condition, we have

$$c_{\mathrm{e1}}(t) = c_{\mathrm{e2}}(t) = e^{-i\omega_0 t}d_1(t) = -i\frac{\Omega}{\Omega'}e^{-i(\omega+\omega_0)t/2}\sin\left(\frac{\Omega' t}{2}\right), \tag{2.38a}$$

$$c_{\mathrm{g}}(t) = d_0(t) = \frac{2i}{\Omega}e^{i\Delta t}\dot{d}_1(t) = e^{i\Delta t/2}\left(\cos\frac{\Omega'}{2}t - i\frac{\Delta}{\Omega'}\sin\frac{\Omega' t}{2}\right). \tag{2.38b}$$

These solutions are same with Eq. 2.30 except the definition of the effective Rabi frequency, $\Omega' \equiv \sqrt{2\Omega^2 + \Delta^2}$. Note that, even under the resonance condition $\Delta = 0$, the maximal population in the excited states is 1/2.

2.2 Bose-Einstein condensation of ideal bosons

Here we present a few properties of BEC which are relevant to the subsequent analysis of their behavior in a optical lattice.

The condensate fraction N_0/N can be expressed as a function of temperature T:

$$\frac{N_0}{N} = 1 - \left(\frac{T}{T_c}\right)^3. \tag{2.39}$$

Thus by the measurement of the condensate fraction, we know the temperature of the atomic cloud consisting of the condensate and thermal gas.

Quite many aspects of BEC can be explained in terms of Gross-Pitaevskii equation:

$$i\hbar\frac{\partial}{\partial t}\Psi(\boldsymbol{r},t) = \left[-\frac{\nabla^2}{2m} + U(\boldsymbol{r}) + \frac{4\pi a\hbar^2}{m}|\Psi|^2\right]\Psi(\boldsymbol{r},t). \tag{2.40}$$

This is a time-dependent nonlinear Schrödinger equation. By separation of variables $\Psi(\boldsymbol{r},t) \equiv e^{\mu t/(i\hbar)}\Phi(\boldsymbol{r})$, we have time-independent one:

$$\mu\Phi(\boldsymbol{r}) = \left[-\frac{\nabla^2}{2m} + U(\boldsymbol{r}) + \frac{4\pi a\hbar^2}{m}|\Phi|^2\right]\Phi(\boldsymbol{r}). \tag{2.41}$$

Here μ have the meaning of the chemical potential of the condensate.

In Thomas-Fermi approximation, one ignores the kinetic term of the Gross-Pitaevskii equation, obtaining

$$\mu\Phi(\boldsymbol{r}) = \left[U(\boldsymbol{r}) + \frac{4\pi a\hbar^2}{m}|\Phi|^2\right]\Phi(\boldsymbol{r}) \tag{2.42}$$

for the time-independent case. Then we can define the so-called "Thomas-Fermi radius" l of the condensate for which trapping potential $U(l)$ equals the chemical potential μ and thus density term ($\propto |\Phi|^2$) vanishes. Due to the anisotropy in the trapping potential, Thomas-Fermi radius generally depends on the direction. Thus, by l_i we denote Thomas-Fermi radius for the direction i ($= r$ or z.)

For each direction of the trap, Thomas-Fermi radius of the condensate can be calculated from the corresponding trap frequency using the following formula:

$$l_i = \frac{1.72}{\omega_i}\left(\frac{Na\hbar^2\bar{\omega}^3}{m^2}\right)^{1/5} = \begin{Bmatrix} 5.62 & (^{87}\mathrm{Rb}) \\ 6.82 & (^{41}\mathrm{K}) \end{Bmatrix} \times \frac{100}{\omega_i/2\pi}\left[\frac{(\bar{\omega}/2\pi)^3}{5\times 10^5}\cdot\frac{N}{10^5}\right]^{1/5} \mu\mathrm{m}. \tag{2.43}$$

Here, $\bar{\omega} \equiv (\omega_x\omega_y\omega_z)^{1/3}$ is the geometric mean of trapping frequencies for three directions of the trap. Coefficients for respective atoms are calculated using these values:

$$a_{\mathrm{Rb}} = 100\, a_0 \qquad a_{\mathrm{K}} = 60\, a_0 \tag{2.44}$$

$$m_{\mathrm{Rb}} = 86.9\ \mathrm{u} = 1.44\times 10^{-25}\ \mathrm{kg} \qquad m_{\mathrm{K}} = 41.0\ \mathrm{u} = 6.80\times 10^{-26}\ \mathrm{kg} \tag{2.45}$$

2.3 Optical lattice

By utilizing a standing wave formed by two counter-propagating laser beams, one can form an optical analogue of the periodic lattice of ions in a crystal. Here we discuss the behavior of atoms confined inside it.

2.3.1 Periodic potential formed by a standing wave of two counter-propagating lasers

For simplicity, our discussion begins with the case of plane waves. Suppose that two plane waves $\boldsymbol{E}$ and $\boldsymbol{E}'$ have same frequency ω and opposite direction of propagation $\boldsymbol{k}$ and $-\boldsymbol{k}$, respectively. Then the electric field $\boldsymbol{E}_{\mathrm{tot}}$ formed by superposition of the two is

$$\begin{aligned}\boldsymbol{E}_{\mathrm{tot}}(\boldsymbol{r},t) &= \boldsymbol{E}(\boldsymbol{r},t) + \boldsymbol{E}'(\boldsymbol{r},t) \\ &= \left(\sum_i \boldsymbol{\epsilon}_i E_i \cos(\omega t - \boldsymbol{k}\cdot\boldsymbol{r} + \delta_i)\right) + \left(\sum_i \boldsymbol{\epsilon}_i E_i' \cos(\omega t + \boldsymbol{k}\cdot\boldsymbol{r} + \delta_i + \Delta_i)\right),\end{aligned} \tag{2.46}$$

where $\boldsymbol{\epsilon}_i$'s are unit vectors pointing to the direction of polarization (hereafter i varies over two symbols "s" and "p" representing s- and p-polarization, respectively,) δ_i's are initial phases for each linearly polarized wave with wave vector $\boldsymbol{k}$, and Δ_i's are additional terms to represent initial phases for waves with wave vector $-\boldsymbol{k}$. Such treatment implies that the waves with $-\boldsymbol{k}$ originates from retroreflection of those with $\boldsymbol{k}$. In the following, we will discuss in a very general manner in that both amplitudes and initial phases are treated as independent eath other, unless otherwise stated.

According to the classical theory of interaction between atoms and electric fields, the energy shift U_{dip} due to an electric dipole moment induced by the electric field is proportional to the squared amplitude of the electric field:

$$\begin{aligned} U_{\mathrm{dip}} \propto |\boldsymbol{E}_{\mathrm{tot}}|^2 &= \sum_i \big[E_i^2 \cos^2(\omega t - \boldsymbol{k}\cdot\boldsymbol{r} + \delta_i) + E_i'^2 \cos^2(\omega t + \boldsymbol{k}\cdot\boldsymbol{r} + \delta_i + \Delta_i) \\ &\qquad + 2E_iE_i' \cos(\omega t - \boldsymbol{k}\cdot\boldsymbol{r} + \delta_i)\cos(\omega t + \boldsymbol{k}\cdot\boldsymbol{r} + \delta_i + \Delta_i)\big] \\ &= \sum_i \Bigg\{ \frac{E_i^2}{2} + \frac{E_i'^2}{2}\cos[2(\omega t - \boldsymbol{k}\cdot\boldsymbol{r} + \delta_i)] + \frac{E_i'^2}{2} + \frac{E_i'^2}{2}\cos[2(\omega t + \boldsymbol{k}\cdot\boldsymbol{r} + \delta_i + \Delta_i)] \\ &\qquad + E_iE_i'[\cos(2\omega t + 2\delta_i + \Delta_i) + \cos(2\boldsymbol{k}\cdot\boldsymbol{r} + \Delta_i)]\Bigg). \end{aligned} \tag{2.47}$$

Here, we used the identity

$$\cos A \cos B = \frac{1}{2}[\cos(A+B) + \cos(A-B)] \tag{2.48}$$

and its corollary $\cos^2 A = (1+\cos 2A)/2$, obtained by setting $A = B$.

The frequency of light as an electromagnetic wave is so large as several hundreds of THz[*3], so only their time-average can physicaly affect atoms, or in particular, the electrons which are its ingredients. Denoting the time-averaged value of a physical quantity A by $\langle A\rangle$, we have

$$\langle|\boldsymbol{E}_{\mathrm{tot}}|^2\rangle = \sum_i \left[\frac{E_i^2}{2} + \frac{E_i'^2}{2} + E_iE_i'\cos(2\boldsymbol{k}\cdot\boldsymbol{r} + \Delta_i)\right], \tag{2.49}$$

since all terms containing $\cos 2\omega t$ are averaged out to zero.

Idealized case

In an idealized case in which $\Delta_i = 0$, $E_{\mathrm{s}}' = E_{\mathrm{s}}$ and $E_{\mathrm{p}}' = E_{\mathrm{p}}$, we have

$$\langle|\boldsymbol{E}_{\mathrm{tot}}|^2\rangle = \left(\sum_i E_i^2\right)[1 + \cos(2\boldsymbol{k}\cdot\boldsymbol{r})]. \tag{2.50}$$

That is, we have a periodic (in particular, sinusoidal) potential for atoms with period of $2\pi/(2k) = \lambda/2$. Here, λ is the wavelength of the laser. The origin of the coordiate system is understood to lie on the plane of retroreflection, since the boundary condition[*4]

$$\langle|\boldsymbol{E}_{\mathrm{tot}}(\boldsymbol{r},t)|^2\rangle\big|_{\boldsymbol{r}\cdot\boldsymbol{k}=0} = 0 \tag{2.51}$$

is satisfied for any t. Note that the (anti)nodes for the both directions of polarization agrees regardless of the initial phases δ_i. Thus we set $E_{\mathrm{p}} = 0$ and write E_{s} as just E. Shifting the origin by multiples of $\lambda/2$, that is, to one of the antinodes at which the potential takes its minimum (for red-detuned case,) we expand the above expression to obtain its harmonic approximation:

$$2E^2\cos(2\boldsymbol{k}\cdot\boldsymbol{r}) = 2E^2\left[1 - (\boldsymbol{k}\cdot\boldsymbol{r})^2 + O(\boldsymbol{k}\cdot\boldsymbol{r})^4\right]. \tag{2.52}$$

This result will be used to calculate the frequency of a small oscillation of atoms confined in an optical lattice.

[*3] For example, IR (infrared) light with wavelength of 1064 nm has frequency of 282 THz.

[*4] Here we assumed the use of metallic mirrors made of metallic material having a nearly infinite conductivity ($\sigma = 4.9\times10^7$ $(\Omega\cdot\mathrm{cm})^{-1}$ for gold, for example) for the boundary condition. The same also applies for dielectric mirrors that are used in part of our experimental system.

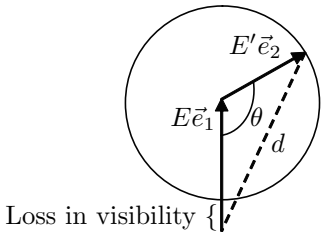

Figure 2.4: Geometric interpretation of the effect of broadening of a retroreflected beam.

Considerations on non-ideal case I: broadening of beams

For evaluation of the effect of misalignment, consider the case in which $E_{\rm p} = E'_{\rm p} = 0$ and $\Delta_i = 0$, but $E'_{\rm s} \equiv E' < E \equiv E_{\rm s}$. The physical meaning of this is as follows: we assume Gaussian beams which have nonzero curvature for their wavefront. Thus their intensity decays like $1/z^2$ as it propagates through free space ($z \to \infty$.) In order to compensate this decay, we use a concave mirror for retroreflection. The radius of curvature R is chosen so that foci of the two beams coincide at the center of a magnetic trap. That is, the distance d between the beam waist of the forward beam and the concave mirror should be set as $d = R$ (or equivalently, $d = 2f$, if we use the focal length f.) Nevertheless, a real experiment cannot be free from deviations from ideal conditions. One need to evaluate effects of mismatch between d and R on visibility of an optical lattice.

First, we give an intuitive image of the problem under consideration. Under the above assumpiton, we have

$$\langle|\boldsymbol{E}_{\rm tot}|^2\rangle = \frac{1}{2}[E^2 + E'^2 + 2EE'\cos(2\boldsymbol{k}\cdot\boldsymbol{r})] = \frac{1}{2}|E\vec{e}_1 + E'\vec{e}_2|^2. \tag{2.53}$$

In the last equation, we used two abstract 2D geometric vectors $\vec{e}_{1,2}$ of unit length such that the mutual angle between them is $2\boldsymbol{k}\cdot\boldsymbol{r}$ modulo 2π (as depicted in Figure. 2.4.) Imagine that the root of $E'\vec{e}_2$ is set at the tip of $E\vec{e}_1$, and $E'\vec{e}_2$ changes its orientation in a circular motion. Then the distance between the root of $E\vec{e}_1$ and the tips of $E'\vec{e}_2$ changes accordingly, and the square of the distance gives the depth of the periodic potential of a non-ideal optical lattice.

For example, we analyze experimental data taken at our lab. An example plot is shown in Figure 2.5. The cross-shaped markers are measured values of $1/e^2$ diameter of intensity of an output beam from a fiber coupler F230FC-C used at Path (A) of the optical lattice. Least-square fit of those by a phenomenological fitting function

$$f(z; w_0, z_0, z_{\rm R}) = 2 \times w_0\sqrt{1 + \left(\frac{z - z_0}{z_{\rm R}}\right)^2} \tag{2.54}$$

yielded parameters of $w_0 = 0.14(1)$ mm, $z_0 = 520(4)$ mm, and $z_{\rm R} = 61(6)$ mm. The fitting function $f(z; w_0, z_0, z_{\rm R})$ given above is "phenomenological" because it treats beam radius w_0 at the beam waist and Rayleigh length $z_{\rm R}$ of the beam as two independent parameters, though the latter is given by $\pi w_0^2/\lambda$, where λ is the wavelength. Such a treatment is often nesessary for better prediction of far-field properties of the beam because of existence of higher order TEM modes. In this case, however, we obtained $z_{\rm R} = 61$ mm. This agrees well with $z_{\rm R} = 58$ mm predicted from $w_0 = 0.14$ mm, and thus the influence of higher order TEM modes can be ignored. The broken curve is the most important entity in the figure, the diameter of the retroreflected beam. The position of its beam waist and its radius at the waist is calculated using the "thin lens equation for Gaussian beams" ($\to$ Appendix)

$$\tilde{b}(\tilde{a}, z_{\rm R}; f) = \frac{\tilde{a}(\tilde{a}-1) + \tilde{z_{\rm R}}^2}{(\tilde{a}-1)^2 + \tilde{z_{\rm R}}^2}, \quad \text{where } \tilde{a} \equiv \frac{a}{f},\ \tilde{b} \equiv \frac{b}{f},\ \text{and } \tilde{z_{\rm R}} \equiv \frac{z_{\rm R}}{f}, \tag{2.55a}$$

$$w'_0(\tilde{a}, z_{\rm R}; f) = \frac{w_0}{\sqrt{(\tilde{a}-1)^2 + \tilde{z_{\rm R}}^2}} \tag{2.55b}$$

$$\iff z'_{\rm R}(\tilde{a}, z_{\rm R}; f) = \frac{z_{\rm R}}{(\tilde{a}-1)^2 + \tilde{z_{\rm R}}^2}, \quad \text{where } z'_{\rm R} \equiv \frac{\pi(w'_0)^2}{\lambda}. \tag{2.55c}$$

For concave mirrors, a relationship $f = R/2$ is used[64]. Then we can estimate visibility of the optical lattice for a given distance d between the beam waist and the concave mirror. Assuming that the waist

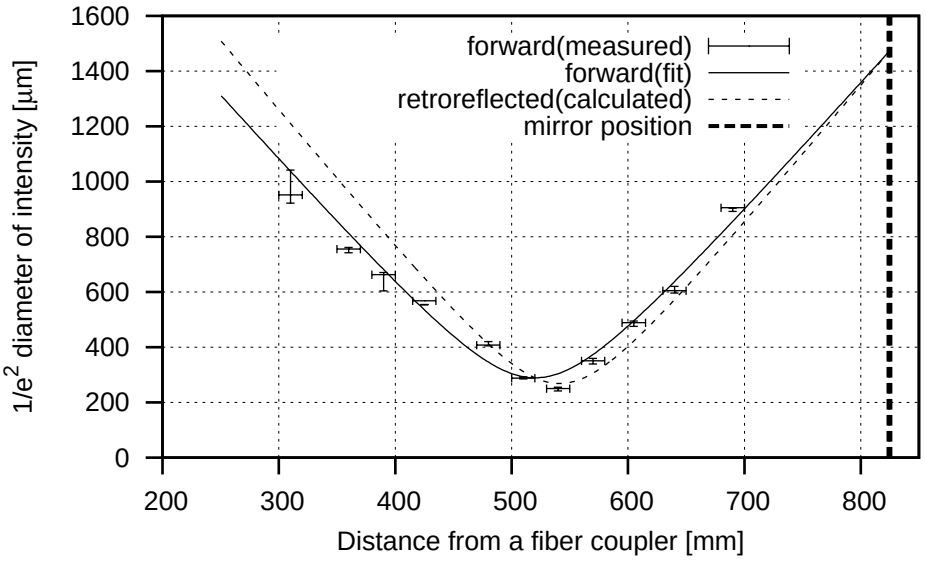

Figure 2.5: Plot of $1/e^2$ diameter of forward- and backward-propagating Gaussian beams.

Figure 2.6: Calculated visibilities at a few points on the standing wave corresponding to Figure 2.5. (a) $z = z_0$, that is, at the beam waist. (b) $z = z_0 + 0.1z_{\mathrm{R}}$. (c) $z = z_0 - 0.1z_{\mathrm{R}}$.

Figure 2.7: The effect of broadening.

of the forward beam is made coincide with the center of the magnetic trap within error whose order of magnitude is Rayleigh length, we substitute E with

$$E_0 \frac{w_0}{w(z)} \exp\left[-\frac{r^2}{w^2(z)}\right] \exp\left[-ik\left(z + \frac{r^2}{2R(z)}\right) + i\zeta(z)\right]\Big|_{z=0}. \tag{2.56}$$

Note that the origin of coordiate system is shifted to make it coincide with the beam waist. This is justified by the fact that the intensity of Gaussian beams decays very slowly compared with the period of a standing wave formed by superposition of them. Thus we may safely forget about the boundary condition (2.51). And simultaneously we substitute E' with

$$E_0 \frac{w_0'}{w'(z-b)} \exp\left[-\frac{r^2}{w'^2(z-b)}\right] \exp\left[-ik\left(z - b + \frac{r^2}{2R'(z-b)}\right) + i\zeta(z-b)\right]\Big|_{z=d},$$
$$\text{where } b \equiv f \cdot \tilde{b}(d/f, z_{\mathrm{R}}, R/2), \tag{2.57}$$

and variables with primes are understood as transformed ones. By computing numelical values for realistic experimental conditions, we can estimate the effect of power imbalance between two beams. The resultant decrease in visibility is about 10–20 %.

Considerations on non-ideal case II: extra reterdation

Dielectric mirrors are formed by many thin layers of dielectric materials with different values of dieletric constants. Their values are designed so that destructive interference causes transmitted light to vanish, leading to reflectivity as high as 99.9 %. Such an high reflectivity is not attainable with metal mirrors that cannot be free from absorption, and leads to the great advantage of dieletric mirrors over metal mirrors. However, this subtle mechanism often leads to unwanted effect of retardation of phase[*5]. That is, dieletric mirrors works as reterdation plate with small but unspecifield retardation δ. Therefore when the incident wave is linearly polarized but whose direction is neither parallel nor orthogonal to the plane of incidence, then the reflected wave is no longer linearly polarized. (As a corollary, the ellipticity of the elliptically polarized wave changes upon reflection by dielectric mirrors.)

[*5]There exist phase retarders (such as half-wave plates or quarter-wave plates) which utilize this effect positively. Such products are called "geometric" or "reflection-mode" phase retarders and differs from traditional phase retarders that are made of birefrengent crystals having different indeces of refraction for "ordinary" and "extraordinary" light in that even when the direction of polarization of the incident wave is rotated along the axis of propagation, its functionality is not affected.

Quantity	Ours	Michigan
Total number of atoms [10^4]	40	5–8
Radial and axial trap frequency $(\omega_r, \omega_z)/2\pi$ [Hz]	(225,10)	(45,15)
Density of atoms [cm^{-3}]		
Wavelength of the optical lattice beam [nm]	1064	852
Maximal power of the 1D lattice beam [mW]	800	200
Diameter of the 1D lattice beam [μm]	280 (e^{-2})	80 (FWHM)

Table 2.1: Comparison between our and Michigan group's experimental conditions. Note that, our value for the beam diameter in the last column refers to the e^{-2} diameter at which the intensity falls to e^{-2} of the peak value, while that of Michigan's group refers to the FWHM (full width at the half maximum) at which the intensity falls to a half of the peak value. For a gaussian beam, the former is about 1.700 times wider than the latter.

Figure 2.8: Diffraction relation of atom and the principle of Bragg diffraction.

Similar effect is observed for the AR- (anti-reflection) coatings on lenses and surfaces of the glass cell of our vacuum chamber. The AR-coating has almost similar structure as dielectric mirrors except that constr the transmitted wave is no longer linearly polarized in the situation stated above.

Therefore we need to treat Δ_i's as nonzero, or specifically, $\Delta \equiv \Delta_\mathrm{p} - \Delta_\mathrm{s}$ as nonzero. Assuming, in turn, that $E_i' = E_i$ for simplicity, we have

$$\begin{aligned}\langle |\boldsymbol{E}_\mathrm{tot}|^2 \rangle &= \sum_i E_i^2 \left[1 + \cos(2\boldsymbol{k}\cdot\boldsymbol{r} + \Delta_i)\right] \\ &= E_\mathrm{s}^2 + E_\mathrm{p}^2 + E_\mathrm{s}^2 \cos(2\boldsymbol{k}\cdot\boldsymbol{r} + \Delta_\mathrm{s}) + E_\mathrm{p}^2 \cos(2\boldsymbol{k}\cdot\boldsymbol{r} + \Delta_\mathrm{s} + \Delta),\end{aligned} \tag{2.58}$$

and in the worst case such that $E_\mathrm{s} = E_\mathrm{p} \equiv E$ and $\Delta = -\pi/4$, we have

$$\langle |\boldsymbol{E}_\mathrm{tot}|^2 \rangle = E^2 + E^2 + E^2 \cos(2\boldsymbol{k}\cdot\boldsymbol{r} + \Delta_\mathrm{s}) + E^2 \sin(2\boldsymbol{k}\cdot\boldsymbol{r} + \Delta_\mathrm{s}) = 3E^2. \tag{2.59}$$

That is, there is no standing wave at all! This circumstance rather resembels *P*olarization *G*radient *C*ooling (PGC), or Sisyphus cooling, in which two counter-propagating, circularly polarized lasers form a "standing wave" of polarization.

Michigan group (Sapiro *et al.* [65]) exploited the *Kapitza-Dirac* KD diffraction to calibrate the depth of the lattice potential. They observed the population oscillation of the undiffracted ($p = 0$) state, and fitted the oscillation by the zeroth-order Bessel function $J_0(x)$, thereby obtaining the Rabi frequency Ω_0 of the Bragg pulse from the first zero $z_0 = \pi/\Delta \approx 2.405$ of $J_0(x)$. Alternatively, one might use the ratios between populations of diffraction peaks of higher orders. However, Michigan group's method is advantageous in practice, because the populations of the peaks of higher orders often have large deviations from the theoretical prediction. And they also observed the reversible loss of superfluidity of BEC. As they deepen the 1D lattice, the sharp interference peaks which was originally present dissapeared around the depth of $30\,E_\mathrm{rec}$. Their experimental conditions (adapted from Sapiro *et al.* [65] and Zhang *et al.* [66]) are summarized and compared with ours in Table 2.1.

Moreover, was obtained experimentaly counterintuitive result on interference patterns from periodic arrays of BECs (Hadzibabic *et al.* [67].)

Ideally, ToF imaging of trapped atoms corresponds to the *Fraunhofer diffraction* (FD) in classical optics. However, Gerbier *et al.* [68] points out that the FD condition is often not met in current BEC experiments. They propose the criterion

$$t_\mathrm{ToF} \gg \tau_\mathrm{FF} \equiv \frac{m l_\mathrm{coh} R_0}{\hbar}, \tag{2.60}$$

where t_ToF denotes the expansion time of ToF, m the mass of the atom, l_coh the characteristic coherence length, and R_0 the characteristic size of the cloud before expansion.

Last but not least, the dissertation by Greiner [69] contains much useful information.

One may consult Weiner [70, Sec. 5.7] for a table summarizing a number of scattering lengths, especially those between two identical alkali atoms. As of February, 2009, the newest reports for rubidium, potassium and cesium are Falke *et al.* [71] and Lange *et al.* [72], respectively. For an accurate determination of scattering lengths, PA (*photoassociation*) spectroscopy is widely used (see, for example, Jones *et al.* [73],

Stwalley and Wang [74], and references therein.) Especially it can produce the so-called *purely-long-range* molecules in which the *Born-Oppenheimer* (or, *adiabatic*) potential of the relative vibrational motion of two nuclei has a minimum located an order of magnitude further than that of ordinary molecules (Stwalley *et al.* [75].) Therefore the entire vibrational motions for low-lying vibrational levels take place in a long-range manner; in particular, the inner classical turning point is located at a distance of more than $50\,a_0$ (a_0 is the Bohr radius.) Then the energy levels for such molecules are solely determined by the van der Waals interaction and one can neglect the interactions due to exchange and overlap of valence electrons that leads to relatively lower accuracy of theoretical analysis.

Component	Company	Product Name
Ion pump (1st; 20 ℓ/s)	Varian	StarCell
(2nd; 75 ℓ/s)	Varian	StarCell
^{87}Rb dispenser		
^{41}K dispenser	Homemade	

Table 3.1: Components used in the vacuum chamber.

Chapter 3

Experimental Setup and Procedure

3.1 Vacuum chamber

3.1.1 Structure

Our BEC machine employs a double-stage MOT design for efficient loading of atoms into MOT. Thus our vacuum chamber can be regarded as composed of two sections, connected by a thin pressure-differential tube. A vapor-loaded MOT in the 1st section of the chamber (hereafter "1st MOT") serves as a high-flux atom source for a MOT in the 2nd section ("2nd MOT.") The 1st section has relatively higher vapor pressure (low vacuum.) On the other hand, the 2nd section is kept at an UHV (ultra-high vacuum) Low conductance of the pressure-differential tube, via which atoms are transferred, is responsible for keeping pressure difference between the two section.

Our vacuum chamber is illustrated in Figure 3.1 and 3.2. On each of the two opposite side of the 1st section of the chamber, An AR- (anti-reflection) coated glass cell (10 cm $\times$ 2.5 cm $\times$ 2.5 cm) and a pressure-differential tube are mounted. Moreover, a hot-filament ionization vacuum gauge and several dispensers of atomic vapor are contained in the 1st section. Vacuum is drawn by a 20 ℓ/s ion getter pump dedicated for the 1st section. Inside the ion pumps, high voltage (usually 2 kV; 7 kV at maximum) is applied so that junk molecules are ionized and absorbed into titanium walls of the pump.

The dispensers release atomic vapor by chemical reaction when heated by current of 4.2 A. To minimize release of junk molecules when they are heated by 4.2 A, they are always moderately heated by 3 A; otherwise junk molecules might be absorbed into the dispensers when the dispensers are as cold as the chamber at the room temperature, rather than drawn by the ion pump. The vapor pressure of the 1st section is kept relatively high (about 1×10^{-9} torr) by vapor from the dispenser so that it works as a high-flux atomic source ($\rightarrow$ Sec. 3.3.1.) On the other hand, that of the 2nd section is kept as low as possible (lower than the detection limit of a gauge, 2×10^{-11} torr,) to make lifetime of a condensate longer.

We can understand the effect of the pressure-differential tube as follows: For dry air at the room temperature in the molecular flow regime, conductance C of a long tube is given by

$$C = \frac{12.1\underline{D}^3/\underline{L}}{1 + (4/3)\underline{D}/\underline{L}}\ \ell/\mathrm{s}, \tag{3.1}$$

by taking account into finite sizes of openings[76]. Here, $\underline{D}$ and $\underline{L}$ are numerical values of the diameter and length of a pipe, respectively, measured in cm. In our case, $\underline{D} = 0.8$ [cm] and $\underline{L} = 14$ [cm], yielding $C = 0.36$ ℓ/s. When we make pressure difference between 1st and 2nd section, the ratio P_1/P_2 between pressures at those sections are related to the ratio between pumping speed P at the 2nd section and conductance C

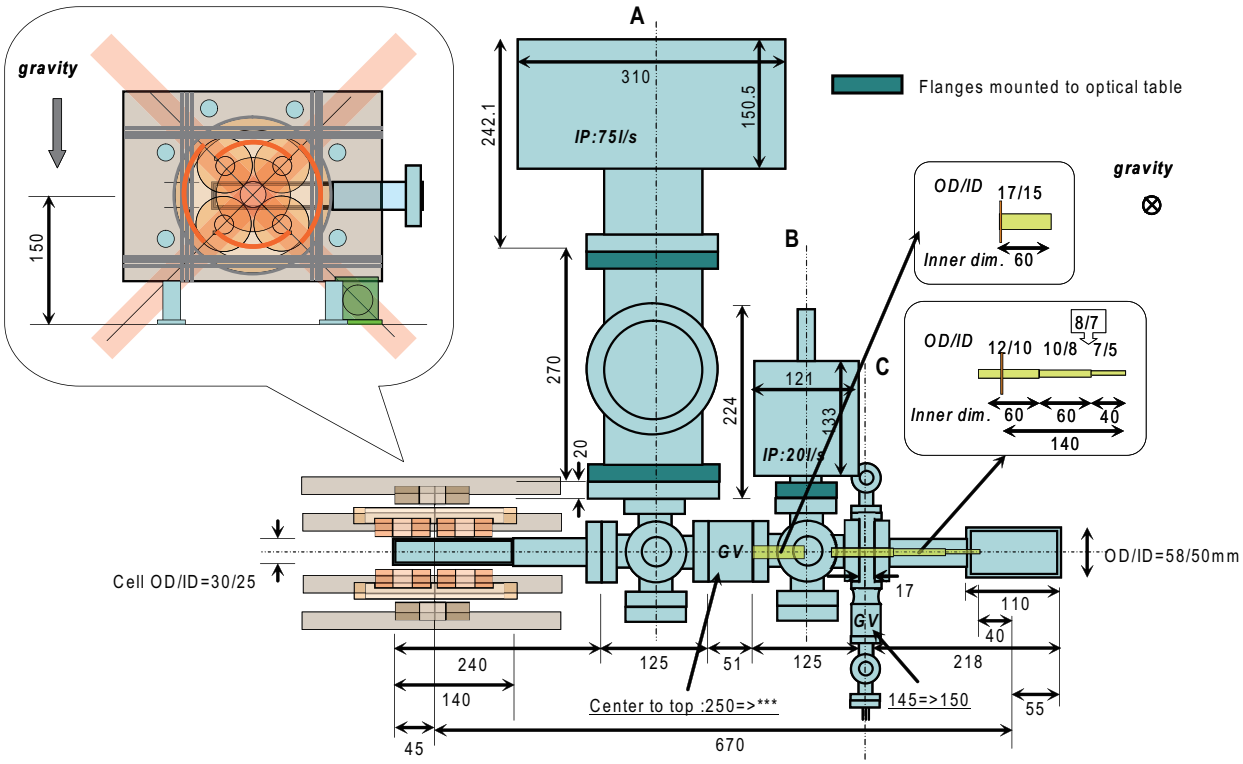

Figure 3.1: Design of the vacuum chamber by Dr. Kishimoto.

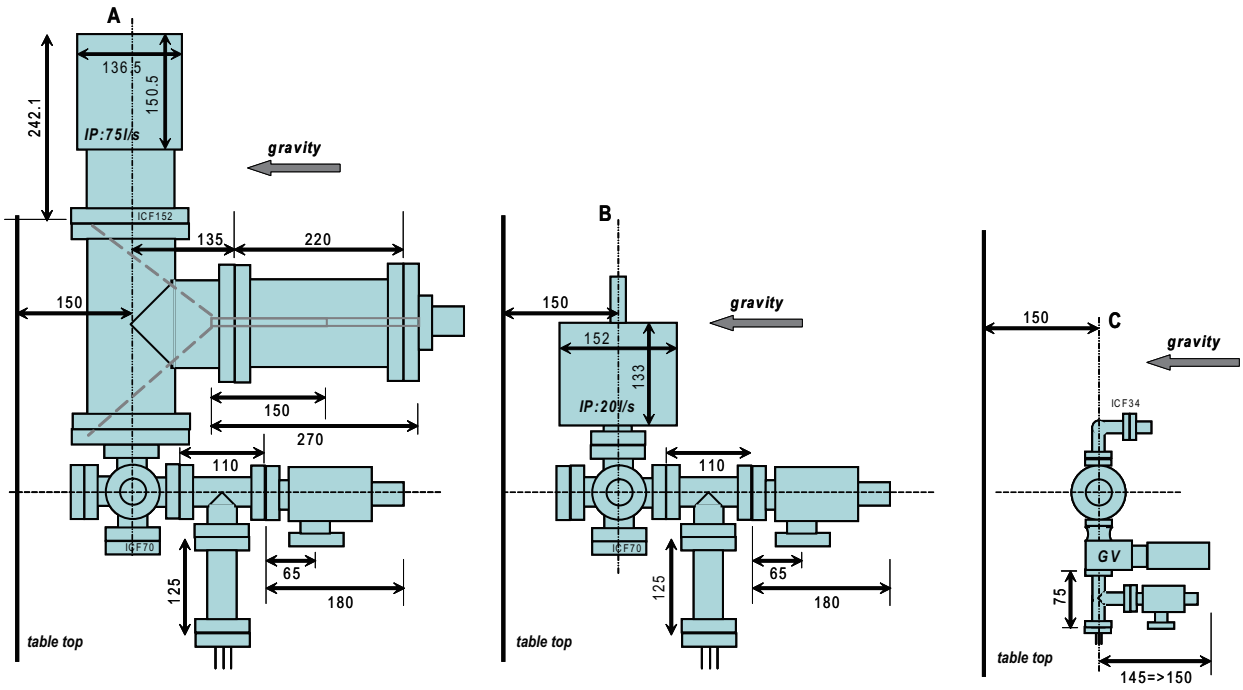

Figure 3.2: Detailed view of Figure 3.1. (A) 2nd section except a glass cell. (B) 1st section, six-way block around atomic vapor dispensers. (C) 1st section, connection gate to a TMP via a bellows.

between the two as $P_1/P_2 = P/C$. In our case, we have

$$\frac{P_1}{P_2} = \frac{10^{-9}\ \text{torr}}{10^{-11}\ \text{torr}} = 10^2 \tag{3.2a}$$

$$\frac{P}{C} = \frac{75\ \ell/s}{0.36\ \ell/s} = 210. \tag{3.2b}$$

Thus we can expect that the desired pressure difference is safely maintained.

3.1.2 Preparation of ultra-high vacuum

Here, we briefly summarize procedures to draw ultra-high vacuum of the chamber.

First, the chamber was roughly drawn by rotary pumps until the pressure went down below 1×10^{-7} torr. Then TMPs (turbomolecular pumps) were operated and the whole chamber was baked for higher vacuum.

The temperature was slowly raised to 200 °C for a day to avoid leakage at flanges or angle valves. Those components are made of stainless-steels that has relatively low thermal conductivity (about 16 $\text{W/m} \cdot \text{K}$) compared with other metals like Duralumin or steel (about 140 $\text{W/m} \cdot \text{K}$ and 50 $\text{W/m} \cdot \text{K}$, respectively.) When one side of such a component is heated, which is unavoidable because of limited number of heaters, and the temperature raise is too fast, they may be strained due to acute temperature gradient and may lead to leakage. Therefore we need to wait long until temperature becomes almost uniform over the whole component. In our case, the angle valve located between the two section determined the upper limit of rate of heating. We baked the chamber for a week, so that we surely removed most of the molecules absorbed into inner walls of the chamber by enhanced detachments of them at the high temperature. Then the temperature was lowerd, again slowly, to the room temperature.

The resultant pressure after baking (5×10^{-11} torr) was an order of magnitude higher than the ideal value. So, as a final stage, we ran a TSP (titanium sublimation pump) for several times. The 2nd section has a large pipe dedicated to the TSP, in order to provide wide surface near filaments of the TSP. We passed the current of more than 40 A to the filament for about 30 seconds. Then the filament sublimates due to Joule heat, and the resultant titanium vapor coats nearby surfaces. The fresh surface coated with titanium absorbs junk molecules. Thus it operates as a pump (getter pump.)

After the pressure at the 2nd section reached 3×10^{-11} torr, we closed the gate valve to isolate the 1st section from the 2nd, and passed current of 5 A to the dispenser for degassing. Then the pressure of the 1st section increased to 8×10^{-7} torr at maximum. However, because of the operation of the ion pump, the pressure decreased to 3×10^{-11} torr within an hour. The degassing was repeated for a few times for each dispenser.

During the time, we sprinkled methanol on the chamber several times to locate the leakage, especially from flanges. When we sprinkled methanol on leakage, it was absorbed into the chamber and raised the pressure inside the chamber. So we could know that the place where we sprinkled methanol had a leakage. Then we tighten bolts of that flange again with care that all bolts are tighten by equal torque ($20\ \text{N} \cdot \text{m}$.) For this purpose, we used a digital torque wrench.

The chamber have been kept closed for one and half year. We have maintained stable ultra-high vacuum though we had several planned power outage of the building. In such a case, we used portable gasoline generator of AC 20 A instead of mains power outlet of the building.

3.2 Frequency-locked lasers

In Figure 3.5, we show a schematics of the optical system to provide lasers whose frequency is locked to ^{87}Rb D2 line. We apply SA (saturated absorption) spectroscopy with FM sideband technique for frequency locking. We separately prepare two subsystems (lower left of the figure) of SA spectroscopy for each of trap and repump laser. For trap laser, the frequency of the master laser is locked to the center of the crossover signal of $|5\,^2\text{S}_{1/2}, F = 2\rangle \to |5\,^2\text{P}_{3/2}, F' = 3\rangle$ and $|5\,^2\text{S}_{1/2}, F = 2\rangle \to |5\,^2\text{P}_{3/2}, F' = 2\rangle$ transitions. The master laser is emitted from an ECLD (external cavity laser diode) whose frequency is tunable via current and angle of a PZT (piezoelectric transducer) attached to a diffration grating which is a part of the ECLD (details are described elsewhere[77].) A PI- (proportional-integral) control circuit is used to stabilize the frequency against its random fluctuation (typical timescale being several kHz) and drift (typical timescale being an hour.) Likewise, the frequency of the repump laser is locked to the crossover signal of $|5\,^2\text{S}_{1/2}, F = 1\rangle \to |5\,^2\text{P}_{3/2}, F' = 2\rangle$ and $|5\,^2\text{S}_{1/2}, F = 1\rangle \to |5\,^2\text{P}_{3/2}, F' = 1\rangle$ transitions.

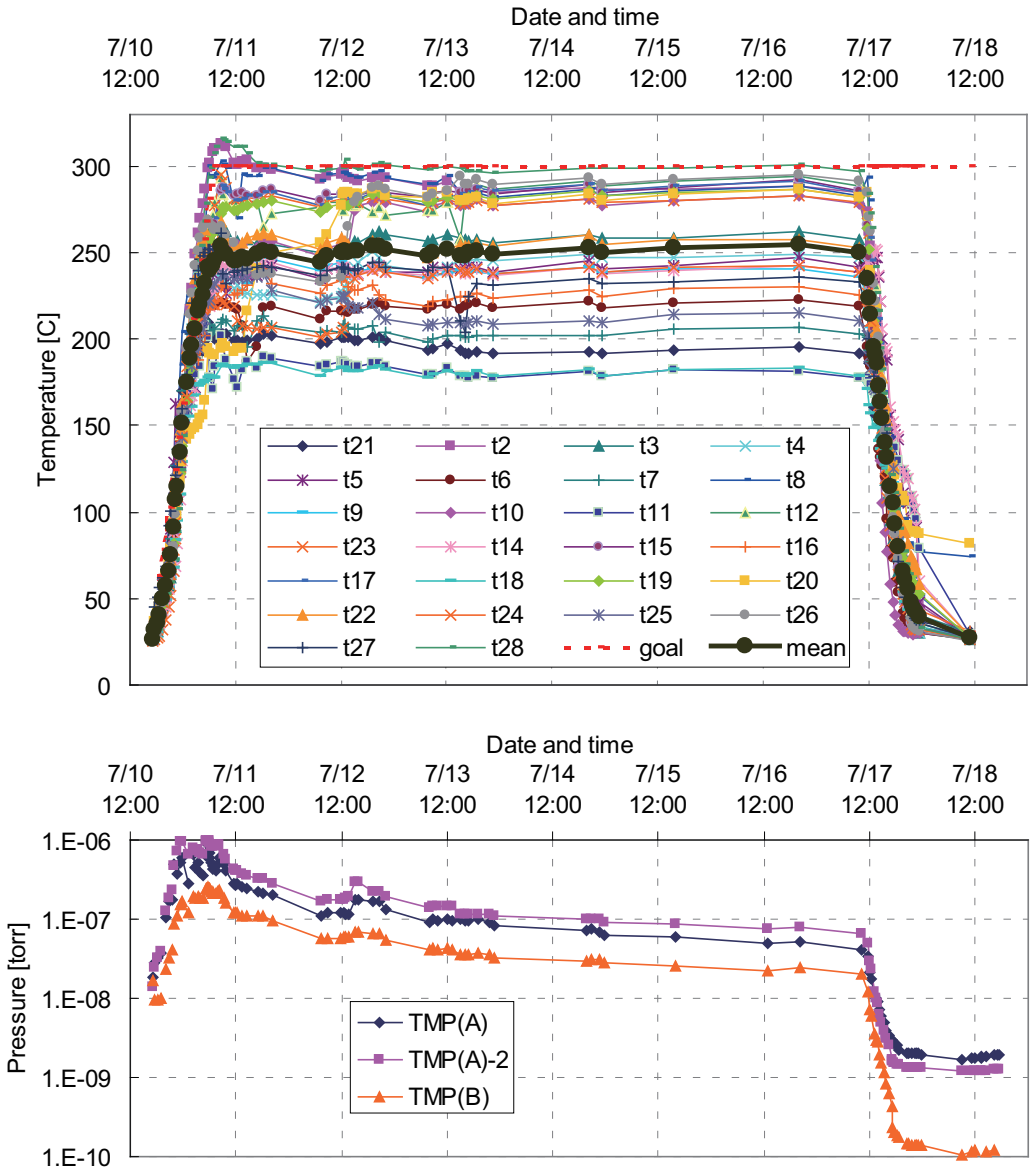

Figure 3.3: A typical sequence of baking the vacuum chamber.

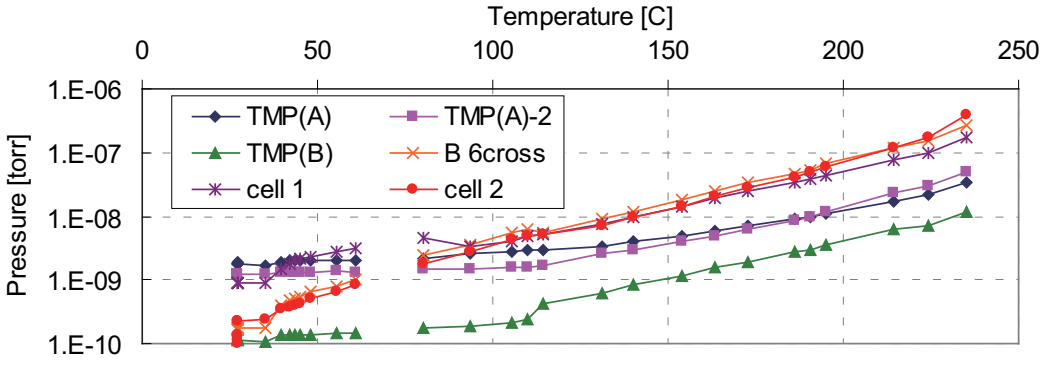

Figure 3.4: Decrease of the pressure during gradual cooling of the chamber.

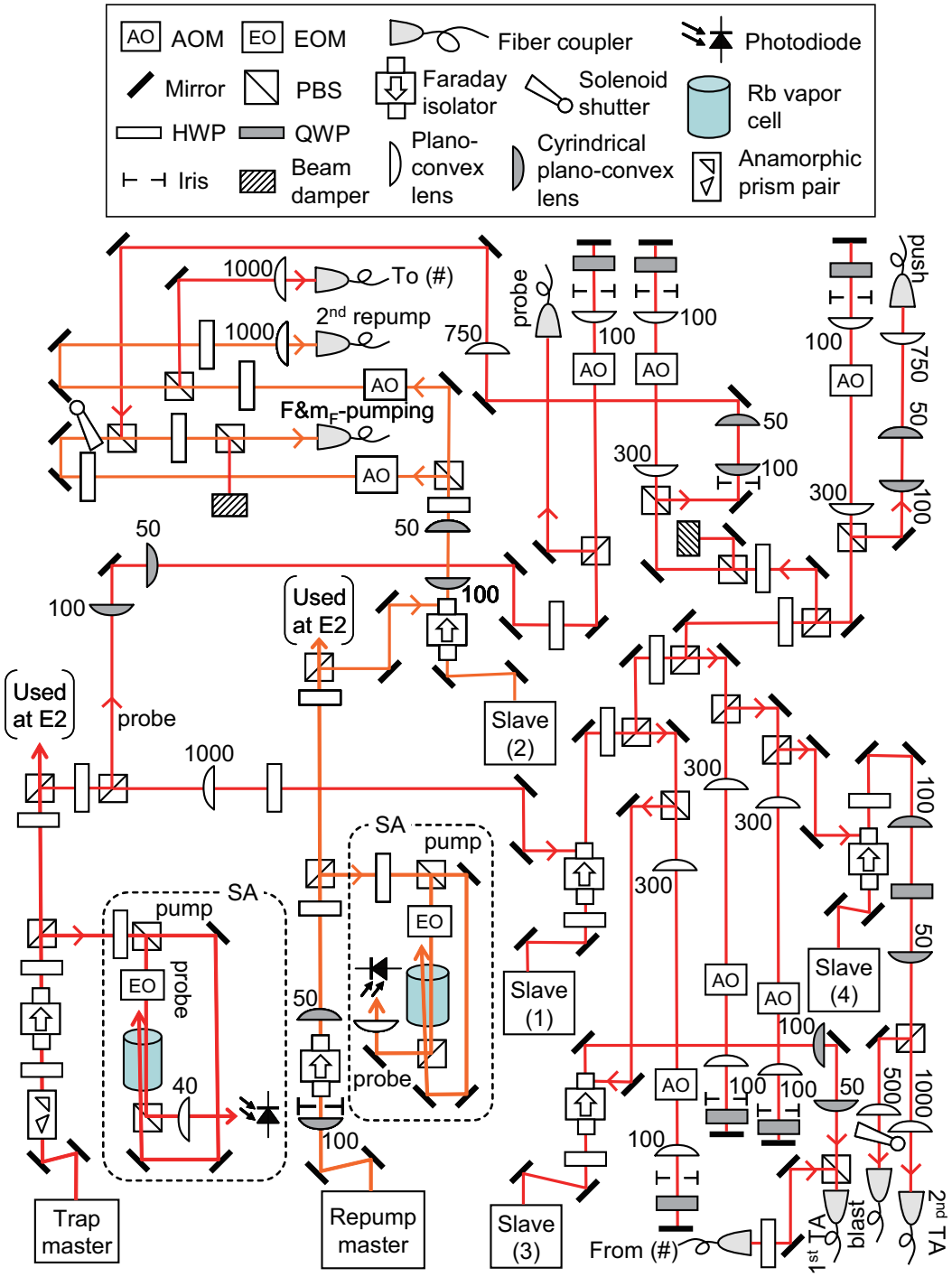

Figure 3.5: Schematics of the optical system to provide frequency-locked lasers.

The master laser is first split into two: one for probe beam and the other for further amplification. Considering the importance of the probe beam, we used a beam directly emitted from the master ECLD and did not use injection locking method (described later) here. Possible imperfection of injection locking may leads to self-sustained pulsation with broad spectrum from a slave ECLD. If such a pulsation light is mixed with an amplified laser whose spectral width is narrow enough (≈ 8 MHz,) OD (optical density[*1]) of images taken by absorption imaging method is reduced by a few times smaller. The split beam for probe passes a double-path AOM (acoustico-optical modulator) and its frequency is shifted by $+67 \times 2 = +134$ MHz. The amount of shift is experimentally determined to maximize absorption by the atomic cloud in MOT. As we tune the detuning, OD of the cloud varies as shown in Figure 3.6. The maximizing value

[*1] OD is defined to be logarithm of ratio of transmitted power to incident power; $\mathrm{OD} \equiv \ln P_\mathrm{t}/P_\mathrm{i}$.

Figure 3.6: The dependence of OD of an atomic cloud of ^{87}Rb on detuning of the probe beam.

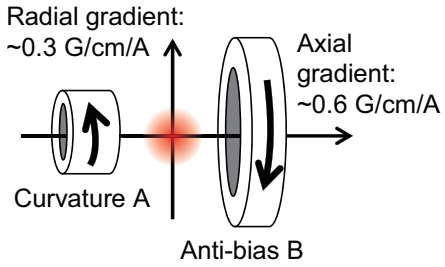

Figure 3.7: Schematics showing "MOT operation" of the coils of the Ioffe-Pritchard magnetic trap.

agrees well with the theoretical value

$$\frac{133.3}{2} = 66.5 \text{ MHz}. \tag{3.3}$$

The other beam is injected to a slave ECLD for amplification by injection locking method. In the figure, injection locking is denoted by incidenting of a beam on the side of the second PBS (polarizing beamsplitter) of a Faraday isolator. Faraday rotation is a phenomenon in which plane of polarizing is rotated because of circular birefrengence (difference in the index of refraction for two circular polarized rays) of the crystal. Circular birefrengence is caused by ferromagnetic resonance and thus depends on the strength of bias magnetic fields. Remembering that magnetic field is antisymmetric under time-reversal, we can use reciprocity theorem to conclude that, in order to have effect on only one of the two rays of opposite directions, we need a phenomenon which involves magnetic field. Utilizing Faraday rotation, we can inject a beam from the master ECLD into the slave ECLD at normal incidence, without a beam emitted from the slave ECLD going back to the master ECLD. If it happens, lasing of the master ECLD may become unstable, because the modes other than one selected by a diffraction grating may become dominant by the influence of the incoming beam in the competition to consume population inversion of the laser medium. On the other hand, the repump

For each of trap ($|5\,^2\mathrm{S}_{1/2}, F = 2\rangle \to |5\,^2\mathrm{P}_{3/2}, F' = 3\rangle$) and repump ($|5\,^2\mathrm{S}_{1/2}, F = 1\rangle \to |5\,^2\mathrm{P}_{3/2}, F' = 2\rangle$) transition,

3.3 Magneto-optical trap

As stated in the last section, our BEC machine employs a double-stage MOT design. Here we describe the detailed properties of each MOT.

3.3.1 1st MOT

The 1st MOT is used as a high-flux atom source for the 2nd MOT. First we made MOT with $N = 7 \times 10^9$. However, it was tuned to optimize the loading rate of the 2nd MOT under the influence of push beam. Thus, currently, the number of atoms, density, and temperature of the 1st MOT itself is not even measured precisely, much less optimized.

Besides the 1st cell, we mount a pair of anti-Helmholtz coils for MOT with their symmetry axis oriented parallel to gravity. They are rigidly fixed to cope with Lorentz force to attract the coils.

The coils were capable of producing a quadrupole magnetic field with linear gradients per 1 A of $(B_r, B_z) = (15, 7)$ G/cm in the radial and horizontal direction, respectively. We usually operate the MOT coil at 1.5 A.

As a result, the time constant of loading into the 1st MOT is so fast as about 0.5 s.

Atoms were initially collected from the background vapor into the 1st MOT. Each of the MOT laser beams has a diameter of about 3 cm, an peak intensity of $10I_{\mathrm{sat}}$, and was tuned 9 MHz to the red of the $|5\mathrm{S}_{1/2}, F = 2\rangle \to |5\mathrm{P}_{3/2}, F' = 3\rangle$ transition of ^{87}Rb. Here, I_{sat} is the saturation intensity for the $|F = 2, m_F = 2\rangle \to |F' = 3, m'_F = 3\rangle$ transition. Another laser beam of intensity $0.2I_{\mathrm{sat}}$, tuned 2.5 MHz below the F51to F852 tran- sition, was used to repump atoms. A 4-mm-diam dark spot in the center of this beam, lled with a second beam tuned to the F52to F852 transition, was used to mitigate

Loading time		0.4 s
Beam Diameter		5 cm
Total power	Trap	200 mW
	Repump	5 mW

Table 3.2: Properties of the 1st MOT.

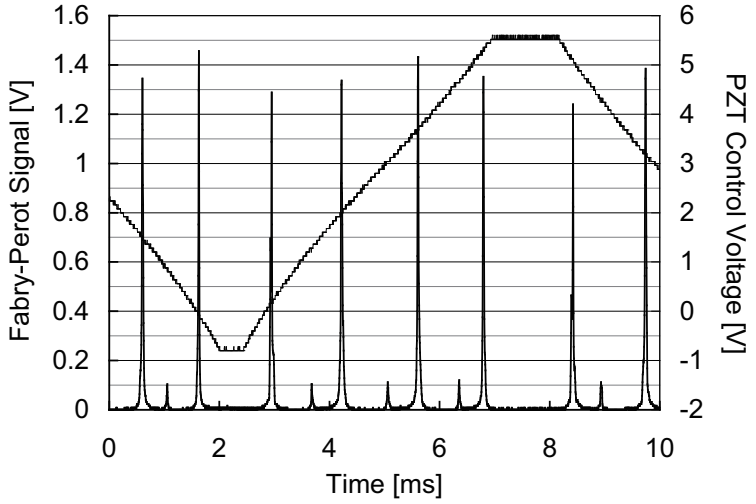

Figure 3.8: A typical signal from a etalon coupled with the injection laser of the TA for the 1st MOT.

Loading time		50 s
Beam Diameter		5 cm
Total power	Trap	250 mW
	Repump	5 mW

Table 3.3: Properties of the 2nd MOT. See also remarks on the Table 3.2.

We summarize properties of the 1st MOT in Table 3.2. In the table, total power is measued just after the optical fiber from which six beams for each direction are split. $I_{\rm sat}$ is the saturation intencity 3.2 mW/cm^2 for D2 line of ^{87}Rb. Note that, direct measurement of each of trap and repump beam is impossible for the 1st MOT, because they are amplified by the TA as a single combined beam and cannot be split for measurement after amplification. Their powers shown in the table are obtained from scaling of total power by relative magnitude of signals of a photodiode located after a Fabry-Perot etalon to which part of the 1st MOT beam is coupled. See Figure 3.8 for a typical signal of the etalon. In the figure, larger (smaller) peaks correspond to the trap (repump) laser, respectively. The width of the etalon is scanned by varying the voltage applied to a PZT on which one of the high-reflectivity mirrors of the etalon is attached. The FSR (free spectral range) of the etalon is estimated to be about 1.24 GHz. Note that, the etalon and the scanning system are homemade and they are not intended to realize exactly linear scanning.

3.3.2 2nd MOT

The 2nd MOT is created inside the ultra-high vacuum chamber in order to prevent collisions from the background gas with the condensate. The velocity of atoms pushed from the 1st MOT is about 20 m/s.

In Figure 3.9, we show a typical loading into the 2nd MOT. The curve is shown with offset (≈ 0.02 V) subtracted. Curve fitting with exponential yielded the time constant of 8.23 s. However, one can observe a strong saturation of the curve after 12 s of loading. In fact, the curve becomes completely flat after 12 s with height of 395 mV. This is far lower than the estimated final value (522 mV) of the loading part of the curve.

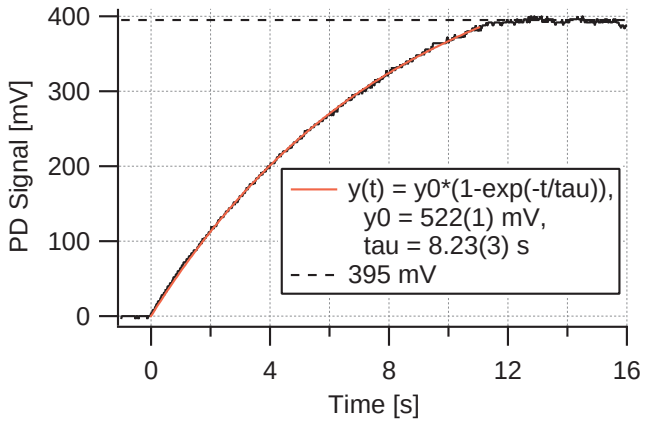

Figure 3.9: A typical loading of pushed ^{87}Rb atoms into the 2nd MOT.

3.4 Magnetic trap

The magnetic trap used for evaporative cooling were constructed as a part of the author's undergraduate research project. For convenience of the readers, we describe its properties here.

Wing[78] showed that, in a free space, the strength of a static magnetic field can have local minima but not local maxima. Thus, by using a dc magnetic field,

One of the most successful design for such traps is Ioffe-Pritchard type[79][80, Sec. 3.5], which we employ for our magnetic trap. It is made of four pairs of cloverleaf coils, a pair of curvature coils, and a pair of anti-bias coils. The roles of each set of coils are as follows:

Cloverleaf coils for radial confinement. They are four pairs of coils. Each pair consists of two coils sharing a common axis in which current flows in the opposite direction. Axes of those pairs are all parallel. Centers of those pairs forms a square around the center of the Ioffe-Pritchard trap in a plane parpendicular to the center axis. Current flows in the same direction for the two pairs in a diagonal line of the square, but in the opposite direction for the other two pairs. Thus they produce a quadrupole magnetic field in that plane: $\boldsymbol{B}_{\rm clv} \approx B'(x\hat{\boldsymbol{x}} - y\hat{\boldsymbol{y}}) = B'r[\cos(2\phi)\hat{\boldsymbol{r}} - \sin(2\phi)\hat{\boldsymbol{\phi}}]$[*2]. Here, B' is a proportional constant to express linear dependence of magnitude on r: $|\boldsymbol{B}_{\rm clv}| \approx B'r$. The dependence of B' on coil current is shown in Table 3.5. Note that $\boldsymbol{B}_{\rm clv}$ does not produce axial confinement.

Curvature coils for axial confinement. They are just a pair of coils which share a common axis with the whole trap itself and in which current flows in the same direction. However, they do not form so-called "Helmholtz" pair. When we look at only one of these, the magnetic field decays as $z^{-2/3}$ as the distance z from the center increases along the center (z-)axis. Let $\boldsymbol{B}_{\rm curv}$ denote the combined magnetic field by the pair. Since the center of the Ioffe-Pritchard trap is the middle point of the centers of two coils (each having radius R and located at $\pm a$,) we see that $|\boldsymbol{B}_{\rm curv}| \propto \sum_{\pm}[(z \pm a)^2 + R^2]^{-3/2}$ along the center axis, and thus axial confinement is realized. In Figure 3.10, we plotted $|\boldsymbol{B}_{\rm curv}|$ for a unit current versus z in the unit of R. Precisely speaking, the combined magnetic field of two coils is written as $\boldsymbol{B}_{\rm curv}(r,z) \approx -(B''_{\rm curv}z/2)(x\hat{\boldsymbol{x}} + y\hat{\boldsymbol{y}}) + \left[B_{\rm curv,0} + B''_{\rm curv}z^2/2 - B''_{\rm curv}(x^2+y^2)/4\right]\hat{\boldsymbol{z}}$. Here the typical value of $B_{0,\rm curv}$ is so large as hundreds of Gauss.

Anti-bias coils to compensate for loosening effect by curvature coils on radial confinement. The combination of the above two sets of coils do not suffice for strong confinement of the atomic cloud. By noting that the value of the combined magnetic field $\boldsymbol{B}_{\rm clv+curv}$ at the center is commont for both r and z directions, we see that the dependence of $\boldsymbol{B}_{\rm clv+curv}$ on r is significantly alterd from that of $\boldsymbol{B}_{\rm clv}$ by the presence of $B_{0,\rm curv}$. Actually it can be approximated as $|\boldsymbol{B}_{\rm clv+curv}(r,z)| \approx \sqrt{B_{B'r+0,\rm curv}}$. The magnetic field produced by curvature coils for axial confinement have the side effect to loosen radial confinement. The strength of magnetic field is proportional to r From calculation, radial confinement can be shown to be proportional to $B'^{4/3}/B_0^{1/3}$. Therefore it is better to lower B_0 for strong confinement. However, it must be lager than 1 or 2 gauss to avoid Majorana spin flipping that leads to loss of the atoms.

The components used to build the trap is listed in Table 3.5 for convenience of the reader.

[*2]Here, for example, $\hat{\boldsymbol{x}}$ is the unit vector parallel to the x-axis.

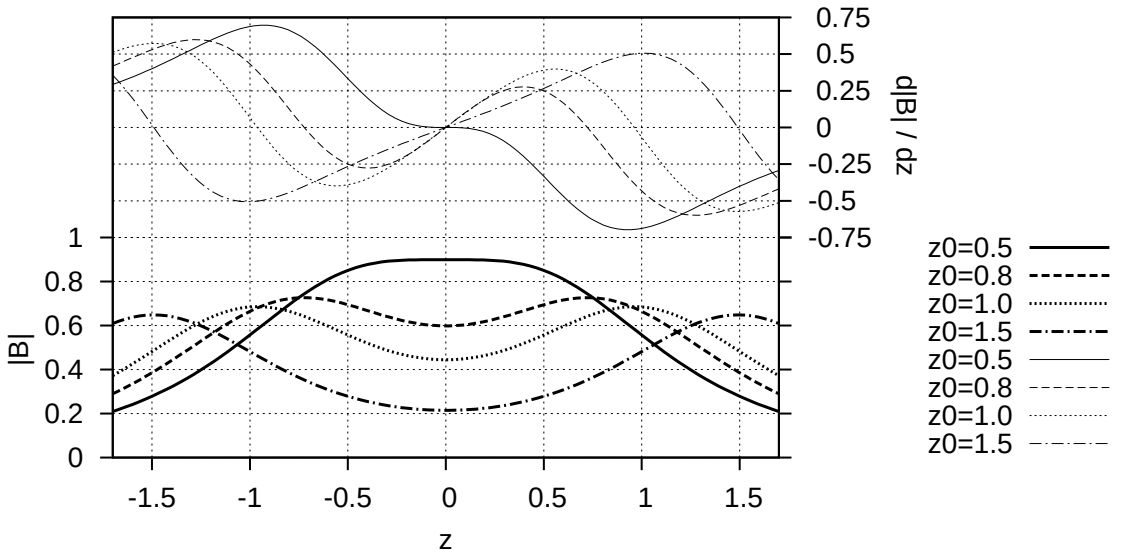

Figure 3.10: Magnetic field produced by a pair of coils sharing a common axis.

Component	Company	Product ID
DC power supply	Agilent Technology	6691A
IGBT	Mitsubishi Electric	CM600HA-24H
IGBT driver	Isahaya Electronics Industry	M57962CL-01
Diode	International Rectifier	SD400N/R
Heatsink for IGBT	Takagi Manufacturing	M-400W
Heatsink for diode	Takagi Manufacturing	P-100S
Liquid cooling system	3R-Systems	Poseidon WCL-04
Copper tube	Hitachi Cable	1/8" square tube with 1/16" square hole
Epoxy adhesive	Konishi	E250 for concrete
Coil holders		Glass epoxy
Water pressure booster pump		

Table 3.4: Components used in the magnetic trap.

Magnetic field at full operation	B'	270 G/cm
	B''	67 G/cm^2
	B_0	≈ 2 G
Voltage drop at full operation	Cloverleaf	27 V
	Curvature	12 V
	Anti-bias	12 V
Trapping frequencies for ^{87}Rb	radial	223 Hz
	axial	10 Hz
Trapping frequencies for ^{41}K	radial	325 Hz
	axial	15 Hz

Table 3.5: Properties of the magnetic trap.

In Table 3.11, we summarize properties of the magnetic trap. All of them are based on numerical calculation by Mathematica, exept the dependence of the bias field at the center of the trap on Anti-bias current. It is experimentally measured by varying the Anti-bias current and observing the minimal rf frequency of evaporative cooling which does not completely remove atoms from the trap.

In Figure 3.11, we show the circuit for Cloverleaf coils of the Ioffe-Pritchard magnetic trap. In order to improve the rising transients of the DC power supply, we attached a large capacitor (15 mF) resistant of high voltage (250 V) as a fast DC power supply. As the capacitor emits its charge by passing current into the coils, the voltage of the capacitor decays. However, it is slow enough that Agilent DC power supply can response and manage to keep the constant voltage (therefore constant current.)

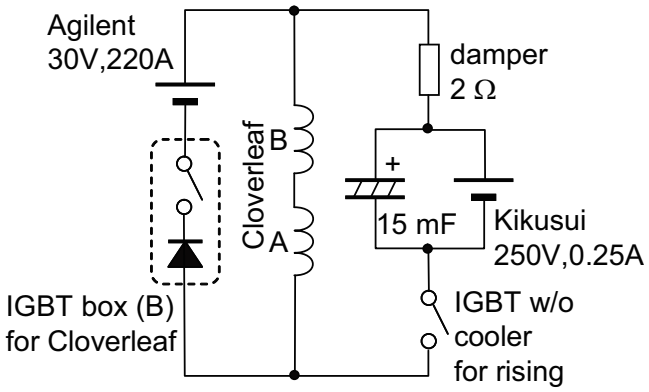

Figure 3.11: The circuit for Cloverleaf coils of the Ioffe-Pritchard magnetic trap.

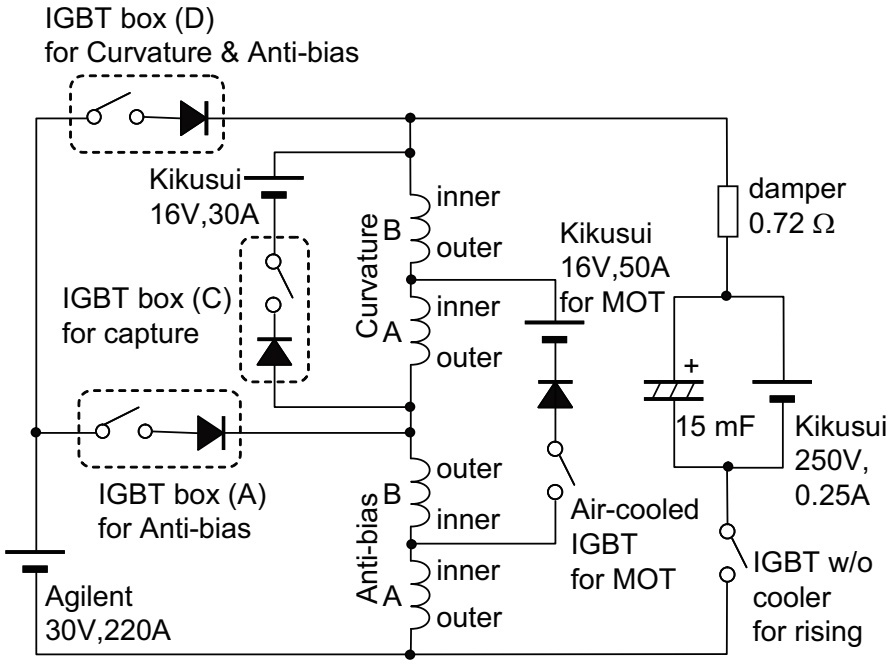

Figure 3.12: Circuit for Curvature and Anti-bias coils of the Ioffe-Pritchard magnetic trap.

Time [s]	0	1	1.1	2	2.1	3			
Frequency [MHz]	87	62	87	62	87	62			
Time [s]	5	13	21	29	35	37	39	40	41
Frequency [MHz]	147	75	38	15	4	1.2	0.6	0.38	0.36

Table 3.6: Typical time sequence of a rf sweep for rf-forced evaporative cooling of ^{87}Rb.

In Figure 3.12, we show the circuit for Curvature and Anti-bias coils of the Ioffe-Pritchard magnetic trap. They are also used for producing a quadrupole magnetic field for MOT (→ Fig. 3.7.) Moreover, Anti-bias coils can be used to produce uniform bias magnetic field (≈ 60 G) to induce Feshbach resonance of ^{41}K.

3.5 RF generator and controller for evaporative cooling

Here we briefly describe the system for applying rf for evaporative cooling. Its details are described elsewhere. Typical sequence of rf sweep is shown in Figure 3.13 and corresponding numerical values are shown in Table 3.6. We use linear interpolation in the region between specified points. Values are separately shown for the first and latter half of the sweep. The first half having zig-zag form is the "cleaning" rf for $|2,1\rangle$ atoms that cause unwanted inelastic loss during evaporative cooling. By three ramping down of the rf, $|2,1\rangle \rightarrow |1,0\rangle$ transition is induced. The latter half is a ordinal rf sweep, as found in JILA's guide[81].

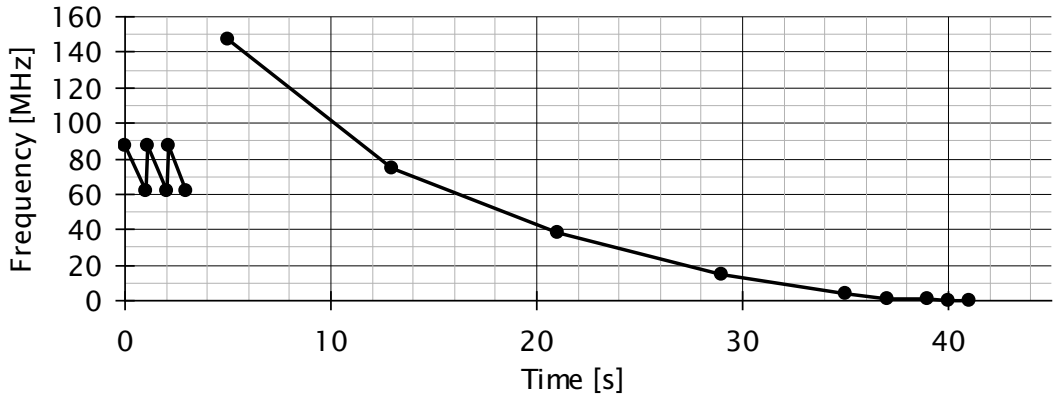

Figure 3.13: A typical time sequence of a rf sweep for rf-forced evaporative cooling of ^{87}Rb. Actual frequencies are the above values plus 6.842 GHz, which is the HFS (hyperfine splitting) of 5 $^2S_{1/2}$ state of ^{87}Rb.

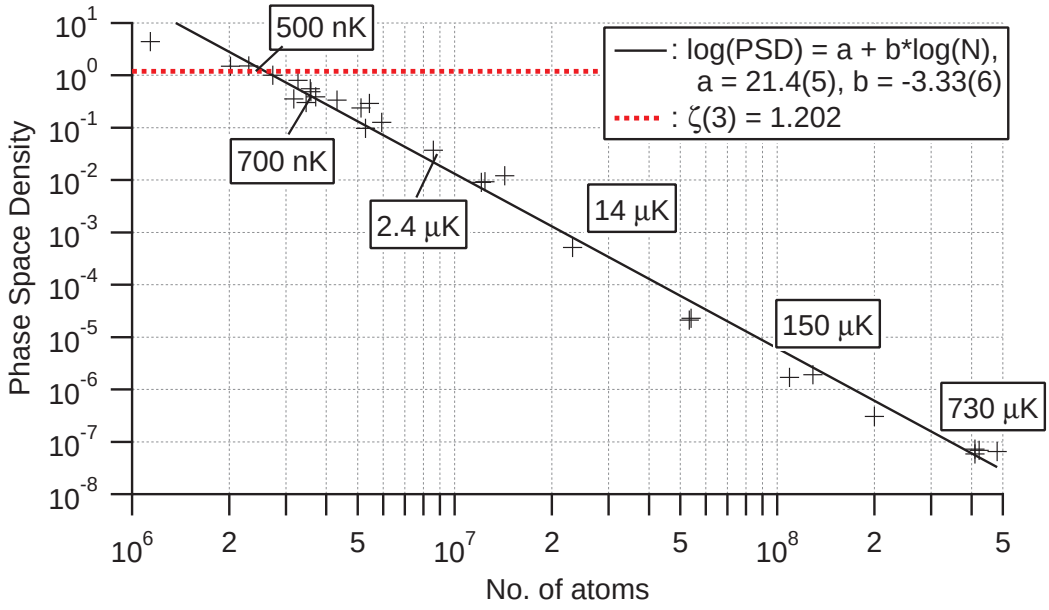

Figure 3.14: A trajectory of a typical evaporative cooling of ^{87}Rb.

The resultant trajectory showing the dependence of PSDon decrease of the number of atoms are shown in Figure 3.14. In the figure, the red broken line indicates the theoretical threshold of BEC transition PSD $= \zeta(3) \approx 1.202$ for ideal Bose gas confined in a harmonic trap. As "hot" atoms, or atoms having the highest kinetic energy among the cloud, are removed from the magnetic trap by spin-flipping caused by rf coupling the initial, weak-field-seeking state that can be tightly trapped by the magnetic trap, to the final, strong-field-seeking state that is repelled from the trap. The trajectory forms an almost straight line. The incline of the line is a measure of efficiency of evaporative cooling[82]. When the points The final frequency at which BEC is produced sometimes fructuates by a few tens of kHz. Especially, the temperature of the laboratory and the magnetic trap affects the final frequency.

For ^{87}Rb, we succeeded to produce BEC by both of the above two methods. In particular, as for the transition between Zeeman sublevels, the loss of atoms due to the inelastic collision between ^{87}Rb atoms in the $|2, 1\rangle$ state is essential factor for this success. Burke *et al.* [83] ascribes the exceptionally small inelastic loss rate to the coincidence between the singlet and triplet scattering length. Scattering lengths for other rubidium isotopes are summarized in the dissertation by Burke [84].

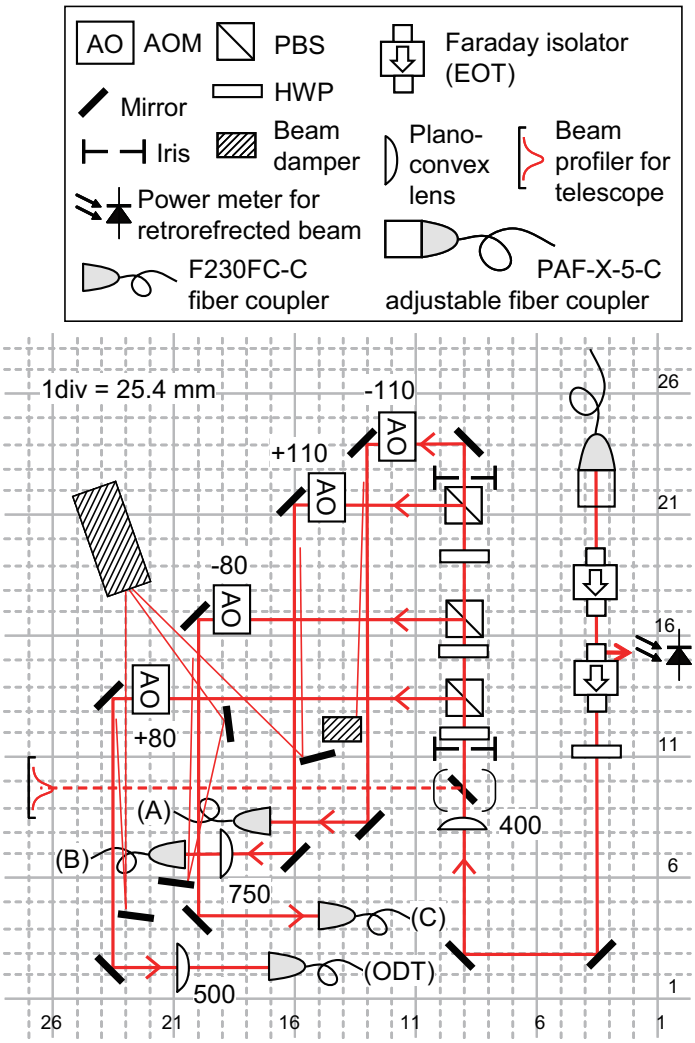

Figure 3.15: Schematics of the optical system for providing laser beam with an optical lattice.

3.6 Optical lattice

3.6.1 1 μm, 5 W fiber laser and an auxiliary optical system

We use a DFB (distributed feedback) fiber laser with MOPA (master-oscillator power amplifier) produced by Furukawa Electric as a laser source. Its linewidth is less than 10 kHz and its output power is 5 W at maximum. We split the emitted laser into four; three for each axis of a 3D optical lattice that is described in later sections, and one for other purposes.

The optical system for splitting is shown in Figure 3.15. In order to show the way how lengths of the four paths are matched, the figure is correctly drawn with respect to lengths between optical components. The grid have distances of 25.4 mm, which is the distance between threaded holes on the optical table.

The output from fiber laser is emitted from a optical fiber attached to a adjustable fiber coupler. It is located at the upper right corner in the figure, directing to the bottom. The adjustable fiber coupler have multiple nobs. Two of them are used to tune transversal position of an aspheric collimation lens with respect to an endpoint of a optical fiber for changing direction of the output beam. Three of them are used to tune longitudinal distance between the collimation lens and the endpoint for changing diameter of the output beam, and the angle of the collimation lens for changing divergence. They are optimized to minimize divergence of the output beam.

Faraday optical isolators

The beam is first coupled to the Faraday optical isorators. When the depth of a standing wave formed by the laser beam is maximized, a considerable portion of the retroreflected beam is coupled to the optical fiber and the AOM, eventually reaching the fiber laser itself. Therefore isolators are necessary to avoid

Figure 3.16: A typical configuration of the telescope.

instability. We use two isolators produced by Electro-Optics Technology with designed isolation of 30 dB each, yielding the total isolation of 60 dB (= 10^{-6}.) Assuming that 1/3 of the emitted power is reflected back to the isolator, we have

$$5 \text{ W} \times \frac{1}{3} \times 10^{-6} = 2 \ \mu\text{W} \tag{3.4}$$

as a maximum power of the retroreflected beam reaching the fiber laser. Moreover, the fiber laser itself has built-in optical isolators. So we may safely conclude that we are free from instabilities caused by the retroreflected beam.

"Telescope"

Nextly, we use lenses (a "telescope") for fine tuning of the diameter and the divergence of the beam, because the efficiency of the AOMs located after it depends on them. The wide space reserved for the telescope is for assurance of its flexibility. A typical configuration is shown in Figure 3.16.

Currently, only a single lens (f = 400 mm) is sufficient for maximizing the efficiencies of the AOMs. That is, it is not a telescope in a strinct sence! The apertures of all the AOMs are about 1 mm square in common, so we tune the telescope so that the beam waist agrees with the locations of the AOMs and the diameter at the waist is 0.8 mm. Then Rayleigh length $\pi w_0^2/\lambda$ (where w_0 is the beam radius at the waist and λ is the laser wavelength) becomes

$$\frac{3.14 \cdot (0.4 \text{ mm})^2}{0.001064 \text{ mm}} \approx 470 \text{ mm}. \tag{3.5}$$

The minimum distance between the AOMs and the telescope is about 500 mm and is comparable to Rayleigh length. So we cannot ignore broadening due to diffraction and need fine tunings of the telescope to avoid power loss at the aperature of the AOM. The radius at the waist is related to divergence θ as

$$\theta = \frac{\lambda}{\pi w_0} \tag{3.6}$$

By the way, we have a choice in the future to replace the fiber laser with a new one with 1080 nm wavelength and 10 W output power. In such a case, we may utilize the flexibility of the telescope to adapt to the new one that emits beam with possibly different diameter and divergence.

When we tune the telescope, we can put a mirror before the iris to reflect to the left. Then we can observe the far-field cross section of the beam with a beam profiler. The space between AOMs and fiber couplers is reserved for that purpose.

A pair of irises

In case of replacement of the fiber laser, we have a pair of irises which indicates the optimal optical path for AOMs and fiber couplers. They can be useful when the fiber laser or mirrors before AOMs are accidentaly moved and need to be fixed to the original configuration.

A series of PBSs and HWPs

We split the beam into four by these PBSs. Relative powers between the four pathes can be tuned by rotating these HWPs. Note that they are not intended for fine tunings. PBSs are air-gapped and therefore resintant to high input power up to about 10 W. They are designed to realize the maximum extinction ratio of 1:1000.

AOMs

The AOMs are used to avoid interference between different axis of the optical lattice and an optical dipole trap for reduction of the density of condensates. We used two kinds of AOMs which are designed for a frequency shift of 80 and 100 MHz, respectively. We use 1st diffracted beam whose frequency is shifted ±80

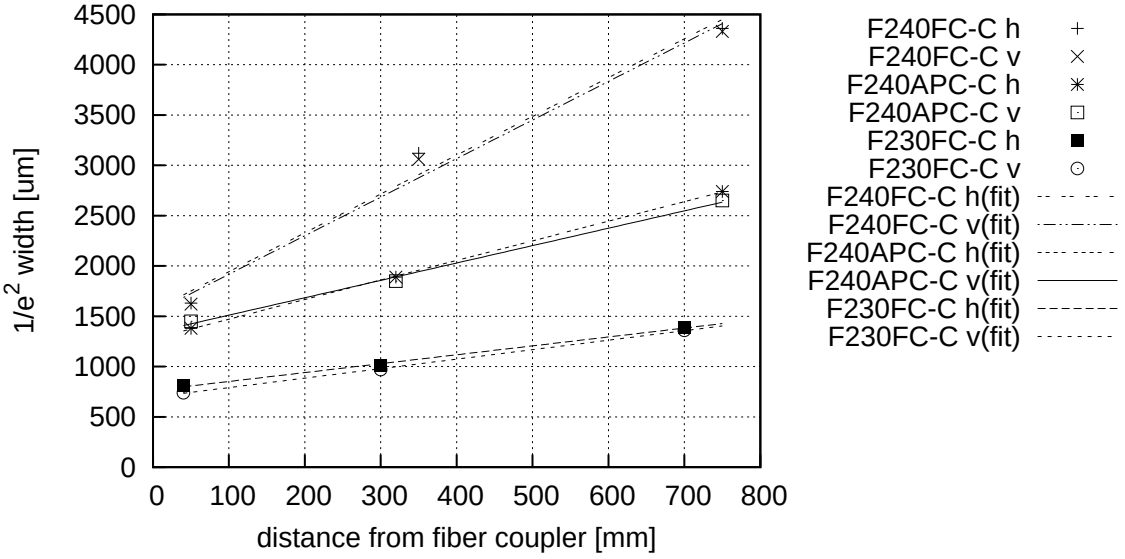

Figure 3.17: The measured $1/e^2$ width of collimated beams by three kinds of fiber couplers. Here suffixes "h" and "v" mean horisontal and vertical width, respectively.

Coupler	Fitting results	
	a [μm/mm]	b [mm]
F240FC-C (h)	3.85(52)	1558(251)
F240FC-C (v)	3.83(46)	1533(218)
F240APC-C (h)	1.95(2)	1277(11)
F240APC-C (v)	1.73(10)	1338(48)
F230FC-C (h)	0.885(49)	763(22)
F230FC-C (v)	0.942(25)	697(11)

Table 3.7: Fitted parameters for data shown in Figure 3.17. Note that, a is so small that it can be used as divergence θ of the ray measured in mili-radian, since $\tan\theta \approx \theta$ when $\theta \ll 1$.

MHz or $\pm$110 MHz for each of the four beams. Therefore the minimal frequency differece between any two of the four beams is $110 - 80 = 30$ MHz, which is enough.

The efficiency of those AOMs are maximized with collimated input beams rather than focused ones. The maximum efficiency ranges from 90 % to 93 %. The dependency of the efficiency on the input power is not observed.

We should note that the maximum efficiency stated above is measured for the stationary case. The efficiency strongly depends on the temperature of the AOM and the temperature itself is affected by the input laser power and the input rf power. So when one changes the rf power to control the power of the diffracted beam, a strong hysteresis is observed with typical period of several seconds. Or we may say that the large-signal slew rate of the AOM is several orders of magnitude smaller than the one for small-signal. Especially, we may need to take care so that the temperature of the AOM is kept high by maintaining input rf power maximum for finer control of the power of the diffracted beam. In such a case we may need to attach mechanical shutters to cut the diffracted beams until they are used in the particular step of the experiment.

Fiber couplers

We choose F230FC-C over F240FC-C and F230APC-C because of its smaller diverngence and easiness to purchace. Those fiber couplers are designed for wide range of wavelength (800–1100 nm) and not adjustable. As a result, the divergence is not optimal for our 1064 nm laser. The measured width of collimated beams by each of those fiber couplers are shown in Figure 3.17. The results of least-square fit of them by linear function $f(x) = ax + b$ is summarized in Table 3.7.

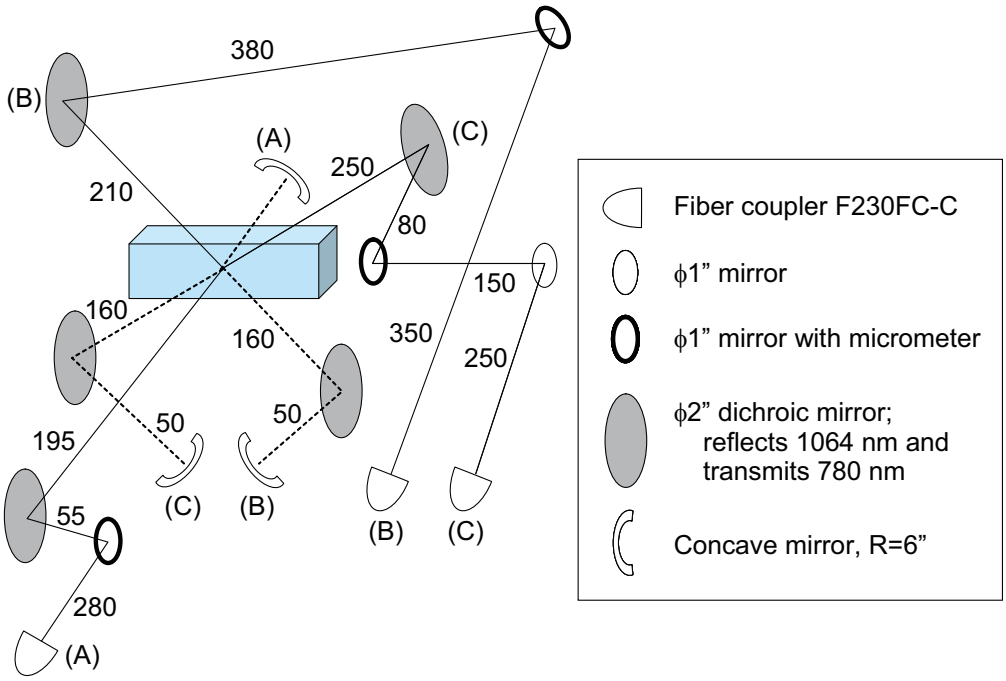

Figure 3.18: Shematics of the optical lattice.

3.6.2 Dimensions of the optical lattice

Our design of the optical lattice is somewhat complicated because of the limited capacity for optical components. The laser beams of the optical lattice must pass through the spaces between optical components aligned around the glass cell and surrounding magnetic trap. Moreover, they need to cross each other at right angle. In order to satisfy these requirements, we used a dichroic mirror which transmits the MOT lasers (780 nm for ^{87}Rb and 767 nm for ^{41}K) and reflects the lattice laser. We inserted them at 45 degrees into each of the three optical path of MOT which are aligned orthogonal to each other. the lattice beams are shined orthogonally to the MOT beams onto the dichroic mirrors and upon reflection their optical paths overlap to those of the MOT beams. Fine tunings of the optical path are done by mirrors inserted before the dichroic mirrors. Their holders are attached with micrometers and their angles can be tuned with accuracy of 0.01 rad per one division of the micrometer. The longest distance between the mirror with micrometer and the center of the optical lattice is about 940 mm of Path (B). In this case, the beam is parallelly moved by

$$2 \times 0.01 \text{ rad} \times 940 \text{ mm} = 18 \ \mu\text{m}.$$

The beam diameter at the beam waist is tuned to 280 μm and Thomas-Fermi diameter of the BEC is 72 μm ($\rightarrow$ Sec. 4.2.) Therefore we can safely rely on them for reproducibility of fine tunings. We use retroreflection by a concave mirror to form standing waves. Thus we first split the lattice beam from the MOT beam by using a dichroic mirror again after it passed the center of the optical lattice, and then place the mirror to retroreflect it.

These three paths are named Path (A), (B), and (C). Schematics of them are shown in Figure 3.18. The lengths in the figure are all measured in milimeters. Note that they have error of several milimeters due to difficulty in measurements because of complex structure of the system. The beam width are configured by telescopic configuration of lenses. Design of telescopes used in each optical path of the optical lattice are shown in Figure 3.19. Calculated lengths for each of three axis are shown in Table 3.8. They are calculated by Maxima based on the formula of Gaussian beams. Here w_0' is the $1/e^2$ radius of intensity at the beam waist inside the telescope. However, the thickness of the lenses are ignored in calculation. Their typical thickness ranges from 5 to 10 mm. We needed fine tunings of the configuration of lenses based on location and width of the beam waist measured by a digital laser beam profiler.

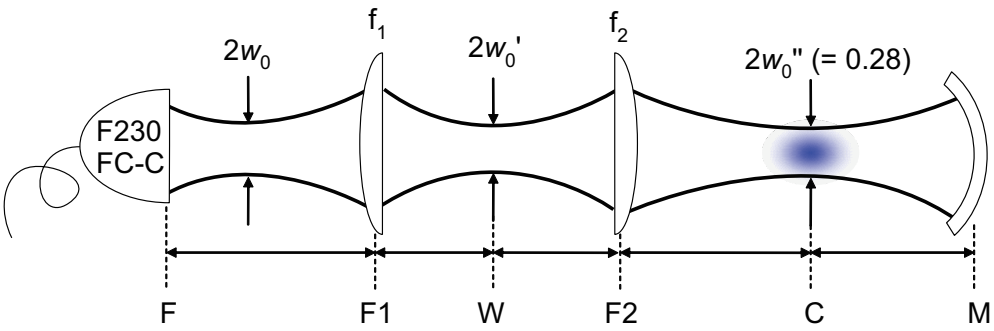

Figure 3.19: Detailed design of telescopes of the optical lattice. See Table 3.8 for actual lengths.

Path	$\overline{\text{F–C}}$	f_1	f_2	$\overline{\text{F–L1}}$	$\overline{\text{L1–W}}$	$\overline{\text{W–L2}}$	$\overline{\text{L1–L2}}$	$\overline{\text{L2–C}}$	w_0'
(A)	530	50	75	51	49	99	148	300	0.042
(B)	940								
(C)	730	50	100	52	49	124	173	505	0.030

Table 3.8: Actual lengths (measured in milimeters) in Figure 3.19, for each path.

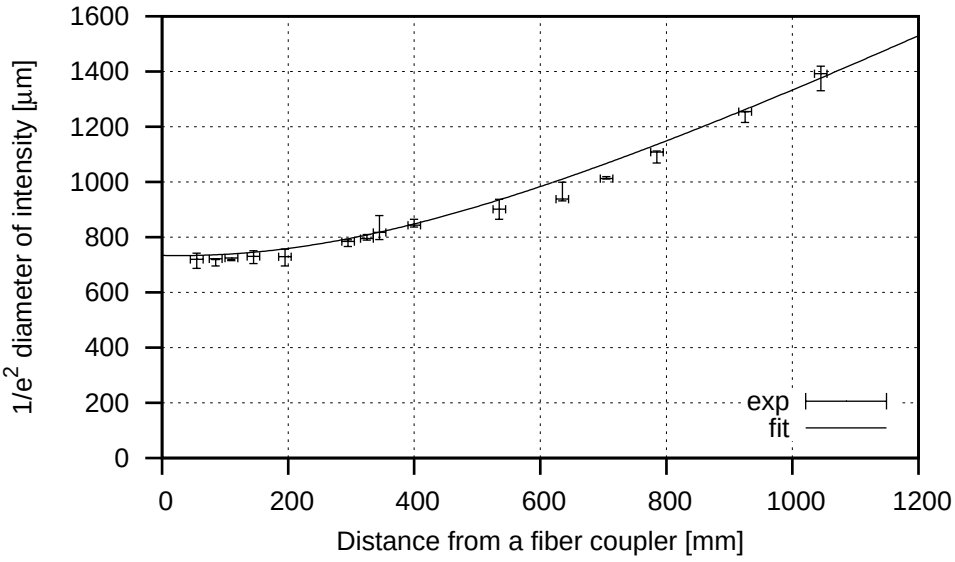

Figure 3.20: An example of measured divergence of output beam from F230FC-C.

$$f(z) = 2 \times w_0 \sqrt{1 + \left(\frac{z - z_0}{z_{\mathrm{R}}}\right)^2}$$

Component	Company	Product ID
Fiber laser	Fitel (Furukawa Electric)	ASF15403
Faraday isolator	Electro-Optics Technology	HP-04-I-1064-000
Mirror	Thorlabs	BB1-E03
Lens	Thorlabs	LA1***-B
Half wave plate		ZOWP-1064-15.00mm-2mntd
PBS	WZW Optics	STR12.7B-LT110
AOM (80 MHz)	Crystal Technology	3080-197
(110 MHz)		3110-197
RF Amplifier	Mini Circuits	ZHL-1-2W
DBM	Mini Circuits	ZAD-1H+
VCO	Mini Circuits	ZOS-150
Optical fiber	Oz Optics	PMJ-3A3A-980-6/125-3-5-1
Fiber coupler	Thorlabs	F230FC-C
Dichroic mirror	CVI Laser	SWP-45-Rs-1064-Tp-780-PW-2025-C
Concave mirror	Edmund Optics	Techspec SPH 1.00IN F/6.0 Gold TS

Table 3.9: Components used in the optical lattice.

3.6.3 Properties of the optical lattice

Here we consider a Gaussian beam. The peak intensity $I_{\mathrm{adv},0}$ at the center of its beam waist is related to its total power P_{adv} as

$$I_{\mathrm{adv},0} = \frac{2P_{\mathrm{adv}}}{\pi w_0^2} = 0.637\frac{P_{\mathrm{adv}}}{w_0^2}, \tag{3.7}$$

where w_0 is the $1/e^2$ radius of intensity at the beam waist. When we make a standing wave, the square of the amplitude of its electric field, $|\boldsymbol{E}(\boldsymbol{r},t)|^2$, reaches its maximum at antinodes around the beam waist. It is four times larger than that of the original Gaussian beam because of constructive interference. We express this fact by saying "a standing wave has a fictious power $P = 4P_{\mathrm{adv}}$ and a fictious peak intensity

$$I_0 = 4I_{\mathrm{adv},0} \tag{3.8}$$

at its antinodes," even though a standing wave carries no power (it is superposition of two waves advancing in opposite directions.) Such a treatment can be justified by the fact that power and intensity (power per unit area) are proportional to the square of the field amplitude.

Now we consider experimental conditions to estimate the upper limit for I_0. The transmittance efficiency of Faraday optical isolators used in our group was about 96 %. We used two isolators in serial, yielding the total transmittance of $(96\ \%)^2 \approx 92\ \%$. The efficiency to produce 1st diffracted beam at the AOM (acousto-optic modulator) is a little more than 90 % at maximum. Fiber coupling efficiency ranges from 80 % to 85 %. Therefore when we split the beam emitted by the fiber laser into four[*3] beams of equal powers and couple them to optical fibers, we have

$$\begin{aligned} P_{\mathrm{adv}} &= 5\ \mathrm{W} \times 92\ \% \times \frac{1}{4} \times 90\ \% \times 80\ \% = \left(5\ \mathrm{W} \times \frac{1}{4}\right) \times (92\ \% \times 90\ \% \times 80\ \%) \\ &\approx 1.25\ \mathrm{W} \times 66\ \% \approx 0.82\ \mathrm{W} \end{aligned} \tag{3.9}$$

for each beam emitted from a fiber. Then the intensity at the center of the beam waist of the emitted beam is

$$I_{\mathrm{adv},0} = 0.637 \times \frac{0.82\ \mathrm{W}}{(280 \times 10^{-6}\ \mathrm{m})^2} = 2.66 \times 10^7\ \mathrm{W/m^2} = 2.66\ \mathrm{kW/cm^2}, \tag{3.10}$$

and the corresponding fictious intensity at antinodes around the center of the standing wave is

$$I_0 = 4I_{\mathrm{adv}} = 10.7\ \mathrm{kW/cm^2}. \tag{3.11}$$

Here we used the measured value $2w_0 = 280\ \mu$m for our optical lattice.

[*3] The fourth beam is saved for other use than the optical lattice. If more than $(5 \times 1/4)$ W is needed for the fourth beam, the above calculation needs to be adapted accordingly.

Power emitted from each fiber	P_{adv}	0.65 W
Beam diameter at the waist	$2w_0$	280 μm
Beam intensity at the waist	$I_{0,\mathrm{adv}}$	1.86 kW/cm^2
Equivalent peak intensity of the standing wave	I_0	7.44 kW/cm^2
Potential depth, divided by k_{B}	^{87}Rb	10.9 μK
	^{41}K	9.85 μK
in the unit of E_{rec}	^{87}Rb	10.9 $E_{\mathrm{rec}}^{(\mathrm{Rb})}$
	^{41}K	9.85 $E_{\mathrm{rec}}^{(\mathrm{K})}$
Photon scattering rate	^{87}Rb	0.04 s^{-1}
	^{41}K	0.03 s^{-1}
Recoil energy, divided by k_{B}	^{87}Rb	96.5 nK
	^{41}K	205 nK
divided by h	^{87}Rb	2.02 kHz
	^{41}K	4.28 kHz

Table 3.10: Properties of the optical lattice.

Using the above value for the maximum intensity of the lattice beam and formulas derived in Sec. 2.3, we have

$$U_0^{(\mathrm{Rb})} \equiv U_{\mathrm{dip}}^{(\mathrm{Rb})} \cdot I = k_{\mathrm{B}} \cdot (11.7\ \mu\mathrm{K}) = h \cdot (220\ \mathrm{kHz}) = 123\ E_{\mathrm{rec}}^{(\mathrm{Rb})}, \tag{3.12a}$$

$$U_0^{(\mathrm{K})} \equiv U_{\mathrm{dip}}^{(\mathrm{K})} \cdot I = k_{\mathrm{B}} \cdot (10.5\ \mu\mathrm{K}) = h \cdot (210\ \mathrm{kHz}) = 51\ E_{\mathrm{rec}}^{(\mathrm{K})}, \tag{3.12b}$$

for the maximum depth of the optical lattice. Here, the recoil energies $E_{\mathrm{rec}}^{(X)}$ for atom X and a laser with wavelength λ are defined as

$$E_{\mathrm{rec}}^{(X)} \equiv \frac{(h/\lambda)^2}{2m_X}. \tag{3.13}$$

The interpretation of this quantity is as follows: Initially there was an atom X with mass m_X which was at rest, and then it is kicked by absorption of a photon with momentum $\hbar k = h/\lambda$ (where k is the wavenumber.) The atoms begins to move with momentum h/λ and the corresponding kinetic energy is $(h/\lambda)^2/2m_X$; the above definition can be understood to refer to this quantity. The formulae below is useful for calculation of the numerical value for recoil energies:

$$E_{\mathrm{rec}}(\tilde{\lambda}, A) = \frac{[h/(\tilde{\lambda}\ \mu\mathrm{m})]^2}{2A\mathrm{u}} = \frac{1.32 \times 10^{-28}}{A\tilde{\lambda}^2}\ \mathrm{J} = k_{\mathrm{B}} \cdot \left(\frac{9.57 \times 10^3}{A\tilde{\lambda}^2}\ \mathrm{nK}\right) \tag{3.14a}$$

$$= h \cdot \left(\frac{200}{A\tilde{\lambda}^2}\ \mathrm{kHz}\right). \tag{3.14b}$$

Here, $\tilde{\lambda}$ is the numerical value of the laser wavelength measured in μm and $A = Z + N$ is the mass number for the atom X. Then $A\tilde{\lambda}^2$ is usually between 10^1 and 10^2. For example, for the lattice beam used in this research, we have $\tilde{\lambda} = 1.064$ (1064 nm,) thus

$$^{87}\mathrm{Rb}: \quad \tilde{\lambda}^2 A_{\mathrm{Rb}} = 1.064^2 \cdot 87 = 98.5 \quad \therefore E_{\mathrm{rec}}^{(\mathrm{Rb})} = k_{\mathrm{B}} \cdot (97.2\ \mathrm{nK}) = h \cdot (2.03\ \mathrm{kHz}), \tag{3.15a}$$

$$^{41}\mathrm{K}: \quad \tilde{\lambda}^2 A_{\mathrm{K}} = 1.064^2 \cdot 41 = 46.4 \quad \therefore E_{\mathrm{rec}}^{(\mathrm{K})} = k_{\mathrm{B}} \cdot (206\ \mathrm{nK}) = h \cdot (4.31\ \mathrm{kHz}). \tag{3.15b}$$

Note that, the accurate mass of these atoms are not exact multiples of atomic mass unit u, or $1.660\,538\,73(13) \times 10^{-27}$ kg[85]. However, deviations from exact multiples[*4] can be safely neglected for our purpose, as done in the above calculations. For example, the accurate mass of ^{87}Rb atoms is $1.443\,160\,60(11) \times 10^{-25}$ kg[86]. This amounts to 86.909 180 520(15) u and the fractional difference is only $86.909\,180\,520/87 = 0.1$ %.

3.7 Imaging system

Our imaging system can be operated in three ways; magnified vertical imaging, reducted vertical imaging, and magnified horizontal imaging (Fig. 3.21.) We can switch between those operation modes by insertion

[*4] These quantities corresponds to the binding energy of the nucleus of an atom, which is the basis for the nuclear fission (and possibly, in the future, nuclear fusion) reactors.

Component	Company	Product Name
CCD camera	Princeton Instruments	PhotonMax
CCD camera driver	Princeton Instruments	WinView
Compiler for fitting program[*1]	Microsoft	Visual Basic 6

Table 3.11: Components used in our imaging system.

Operation mode	Magnification
Magnified vertical	4.2
Reducted vertical	0.3

Table 3.12: Magnification of the imaging system for each operation mode.

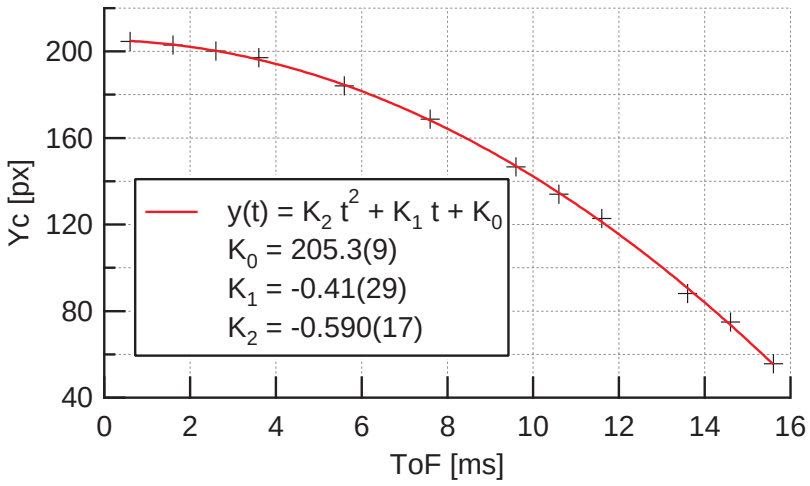

Figure 3.21: Measurement of falling atomic cloud.

and removal of mirrors attached on a magnetic mount. The accuracy of position of the magnetic mounts are well within tolerance, judging from the fact that images are quite reproducible over repeated insersion and removal of those mirrors.

The magnification factors of two vertical imaging mode was measured by imaging thin scale made of paper and comparing its periodicity. That of horisontal imaging was measured by multiple images of falling atomic cloud and comparing its accelaration with gravitational accelaration.

[*1]The program for curve fitting and overall control of the imaging system originates from JILA. It uses Microsoft Automation technology to control WinView. The API (application programming interface) of WinView necessary for programming is described in the manual[87].

Chapter 4

Results and Discussions

4.1 BEC of ^{41}K

After rf-forced evaporation, we obtained a pure sample of ^{41}K BEC[47]. The number of atoms in the condensate N_{BEC} was determined by fitting Thomas-Fermi density profile on the OD data integrated along the radial (tight) axis of the magnetic trap. For a pure condensate, we obtained $N_{\mathrm{BEC}} = 3 \times 10^5$.

We started from a MOT with $N = 1.6 \times 10^9$, $n = 1.6 \times 10^{10}$ cm^{-3} and $T = 5$ mK, corresponding to phase space density of $\rho_{\mathrm{PS}} = 10^{-9}$ (Tab. 4.1). This is two orders of magnitude smaller than that of ^{87}Rb, because of the inefficiency of MOT. The hyperfine splitting of $4\,^2\mathrm{P}_{3/2}$ of ^{41}K has an anomalously small value of only 14 MHz. Therefore if we detune trap and repump lasers of MOT for efficient cooling, the hyperfine states are not resolved and closed transition is violated, leading to the inefficiency mentioned above. To circumvent this undesirable feature, we employed a version of CMOT technique[89], in which the prodecude is split into two stages for different purposes[77].

Compression (usual CMOT) The duration of this stage is 40 ms. We ramp up the magnetic field gradient from about 3 G/cm to about 30 G/cm. Simultaneously, we lower intensity of the trap laser from $5.6 I_{\mathrm{sat}}$ to $0.1 I_{\mathrm{sat}}$ to avoid pressure from spontaneously emitted photons, and lower detuning from 34 MHz to 31 MHz to enhance trapping effect.

Doppler cooling The duration of this stage is 12 ms. At the beginning of this stage, we suddenly lower the magnetic field gradient to 2 G/cm and keep this value until the end of this stage.

After these stagse, phase space density of ^{41}K has a comparable value (1×10^{-6}) to that of ^{87}Rb (6×10^{-6}). The data of ^{87}Rb is adapted from experimental report from MIT group who are regarded to have the current state-of-the-art BEC machine. Thus our result is quite satisfactory.

Then we adiabatically transfere the ^{41}K cloud into the Ioffe-Pritchard magnetic trap (→ Sec. 3.4.) For ^{41}K, we need to scale trap frequencies described in Sec. 3.4 because of the different masses of ^{41}K and ^{87}Rb. Since the mass of ^{41}K is 40.961 825 4(12) u ≈ 41 u (0.09 % error,) the trap frequency differs by a factor of $\sqrt{41/87}$.

As we lower the rf frequency for evaporative cooling, bimodal structure of a ToF image was observed. Figure 4.5 shows such images and vertical sum of OD. Plots (orange dots) below images are OD integrated

	^{41}K in stable MOT	^{87}Rb^{*1} in stable MOT	^{41}K after two-stage CMOT	^{87}Rb^{*1} after CMOT
Splitting between $F' = 2, 3$ [MHz]	14	267		
Natural linewidth of D2 line [MHz]	6.2	6.1		
Temperature [μK]	5000	150	100	10
Density [10^{10} cm^{-3}]	1.6	1	5.1	10
Number of atoms [10^9]	1.6	40	1	≈ 10
Phase space density [10^{-7}]	0.01	100	10	60

Table 4.1: Comparison between MOT of ^{41}K and ^{87}Rb.

*1 Adapted from report of MIT[88].

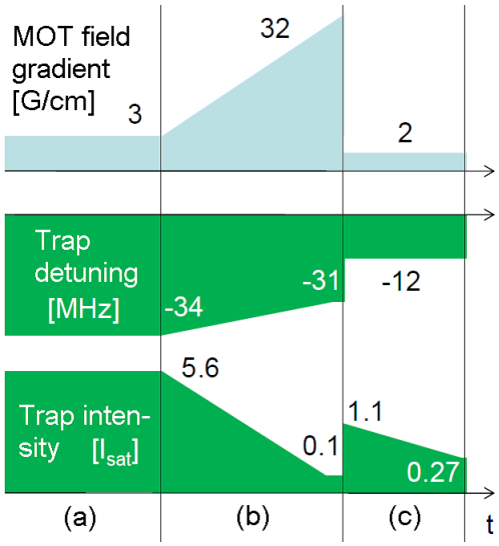

Figure 4.1: Combination of CMOT and following Doppler cooling for ^{41}K. (a) Loading into MOT ($\approx$ 10 s.) (b) CMOT for higher density. (c) Doppler cooling for lower temperature.

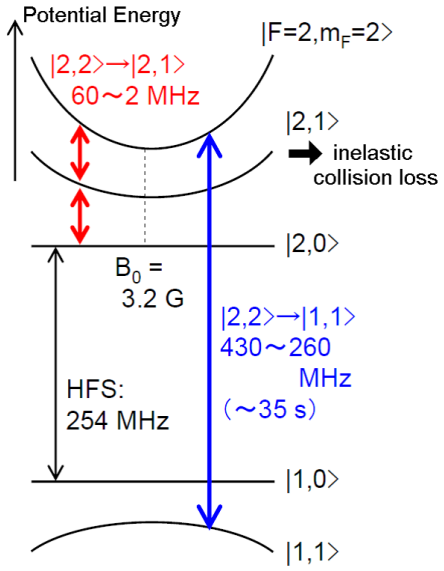

Figure 4.2: Transitions used for rf-forced evaporative cooling of ^{41}K for successful (blue) and unsucsessful (red) methods.

Time [s]	0	16	24	28	32	34.9	35
Frequency [MHz]	300	300	269.2	264.3	260.3	259.48	311

Table 4.2: A typical time sequence of a rf sweep for rf-forced evaporative cooling of ^{41}K.

along the vertical axis (the axis of tighter confinement of magnetic trap) in arbitrary units. Results of least-square fitting by the bimodal density profile function are also shown in red curves.

As a conculusion of this section, we summarize keypoints of our realization of ^{41}K BEC.

- CMOT followed by Doppler cooling was effective to cope with peculiar hyperfine level structure of ^{41}K
- A hyperfine transition $|2,2\rangle \rightarrow |1,1\rangle$ was effective to avoid unwanted inelastic collision $|2,1\rangle + |2,1\rangle \rightarrow |2,2\rangle \rightarrow |2,0\rangle$ which releases energy due to quadratic Zeeman effect.

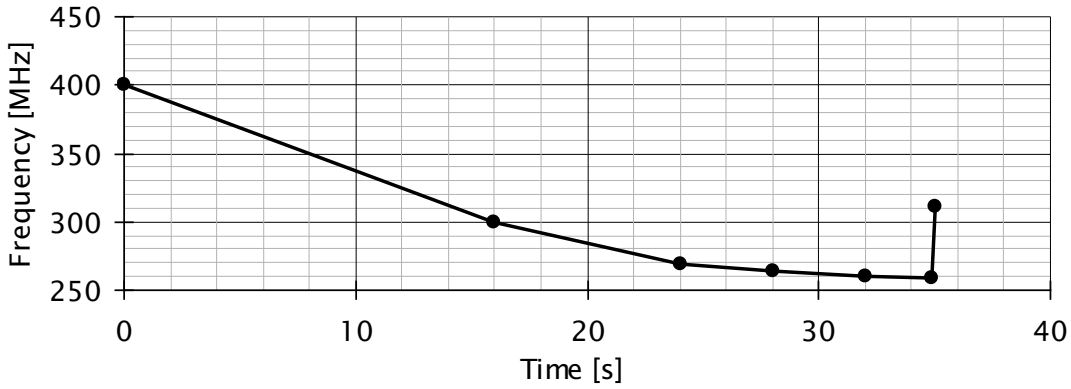

Figure 4.3: A typical time sequence of a rf sweep for rf-forced evaporative cooling of ^{41}K. Note that the HFS of $4\,^2S_{1/2}$ state of ^{87}Rb is 259.0 GHz.

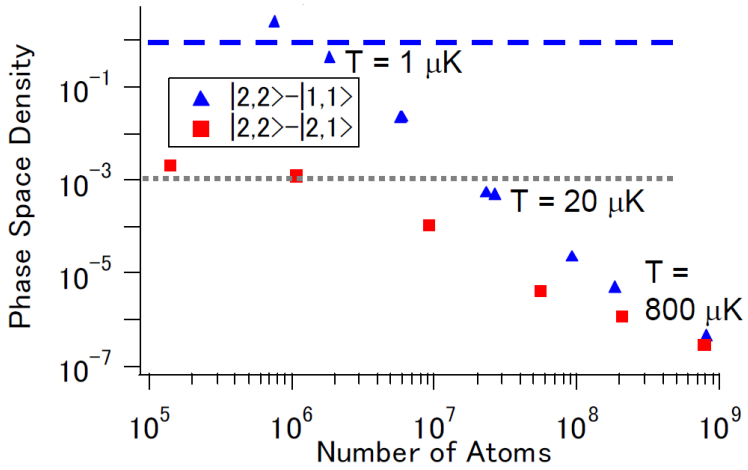

Figure 4.4: Typical trajectory of evaporative cooling of ^{41}K, for successful (blue) and unsucsessful (red) methods.

4.2 Bragg diffraction of the condensate

After rf-forced evaporation, we obtained a pure sample of ^{87}Rb BEC. By the use of absortption imaging, the number of atoms N in the condensate was determined to be $N = 4 \times 10^5$.

In our case, $N = 4 \times 10^5$ and $(\omega_r, \omega_z)/2\pi = (223, 10.3)$ Hz for ^{87}Rb atoms, so Thomas-Fermi radii are

$$\begin{Bmatrix} l_r \\ l_z \end{Bmatrix} = 5.62 \cdot \begin{Bmatrix} 1/2.23 \\ 1/0.103 \end{Bmatrix} \cdot 1.005 \cdot 1.32 = \begin{Bmatrix} 3.34 \\ 72.3 \end{Bmatrix} \ \mu\text{m} \tag{4.1}$$

for the radial and axial direction of the Ioffe-Pritchard magnetic trap. Thus the condensate is split into

$$2 \cdot \begin{Bmatrix} 3.34 \\ 72.3 \end{Bmatrix} \ \mu\text{m} \Big/ \frac{1.064\ \mu\text{m}}{2} \approx \begin{Bmatrix} 13\ \text{(radial)} \\ 270\ \text{(axial)} \end{Bmatrix} \tag{4.2}$$

components for each direction. Then the density of the condensate is estimated to be

$$n = 4 \times 10^{14}\ \text{cm}^{-3}. \tag{4.3}$$

As a preliminary experiment, we performed diffraction experiments of the condensate using optical lattice. First, we worked out in the short-interaction (Kapitza-Dirac) regime, in which an opital pulse gives only phase difference to the atoms, without significant displacement of the atoms. Next, we worked out in the long-interaction (Raman-Nath) regime, in which

By this experiment, we confirmed that the Rabi frequency is about 4 kHz.

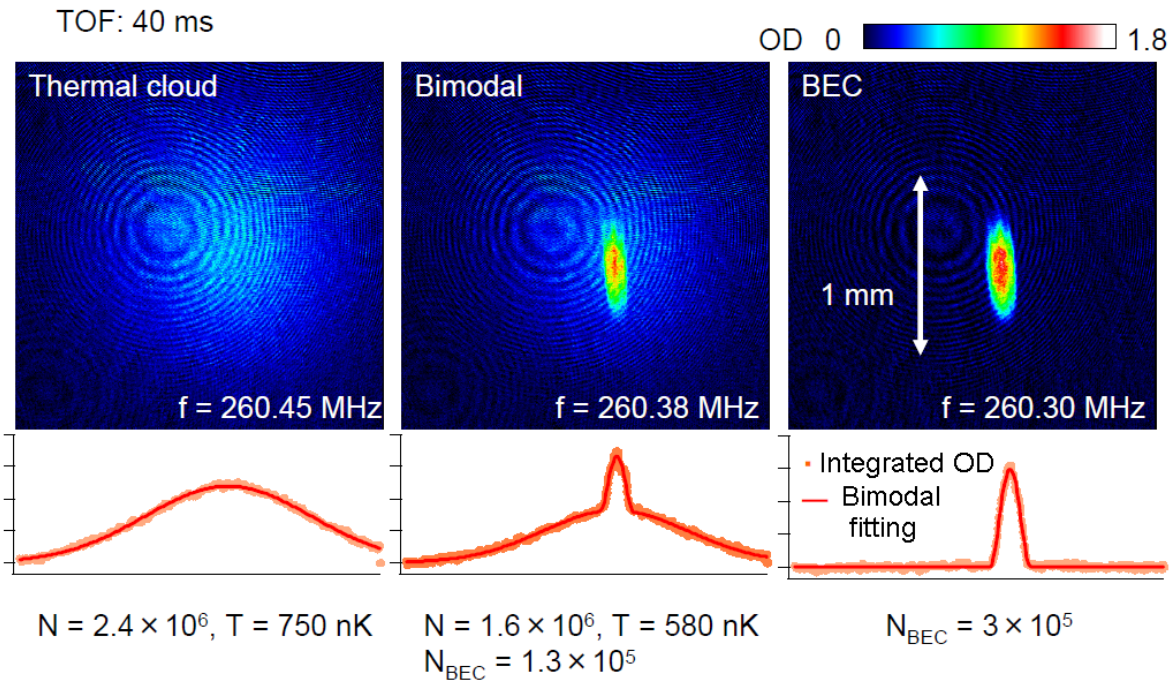

Figure 4.5: Images of ^{41}K BEC, taken after ToF of 40.3 ms. Below those images, vertically integrated OD are plotted. (a) Thermal cloud. (b) Mixture of thermal cloud and BEC. (c) Pure condensate.

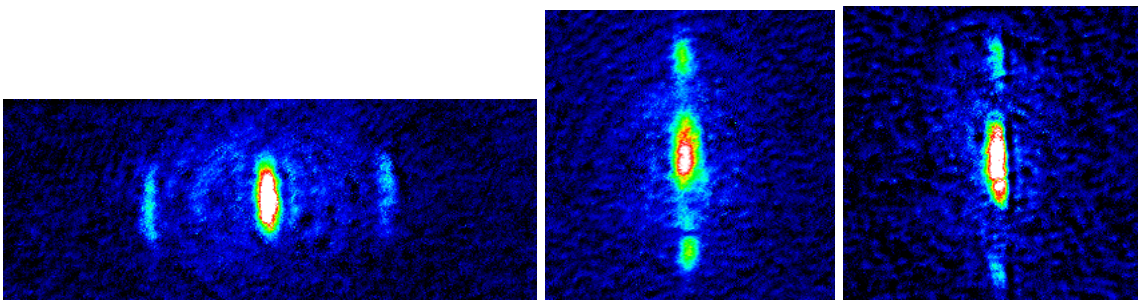

(A) $15E_{\mathrm{rec}}$ (B) $15E_{\mathrm{rec}}$ (C) $15E_{\mathrm{rec}}$

Figure 4.6: Interference pattern of a 1D array of 2D BEC.

4.3 Interference patterns by condensates in 1D optical lattices

In Figure 4.6, we show interference pattern of a 1D array of 2D BEC formed by each of the 1D optical lattices (A), (B), and (C), respectively. These images are taken along the vertical imaging axis.

4.4 Interference pattern of the condensate in 2D lattice

In Figure 4.8, we show interference pattern of a 2D arrays of 1D BEC formed by the 2D optical lattice. Here axes (B) and (C) were used. We can observe 2D interference in figures (b)–(e).

By curve fitting, we can extract the number of atoms in each of the center peak, four diffracted components, and background component. We used the following function:

$$z(x,y) = \sum_{i=\mathrm{c},1,2,3,4} A_i \cdot \mathrm{TF}_2(x - X_i, y - Y_i; l_i) + A_{\mathrm{bg}} \exp\left[-\frac{(x - X_{\mathrm{bg}})^2 + (y - Y_{\mathrm{bg}})^2}{w_{\mathrm{bg}}^2}\right] \tag{4.4}$$

Here, $\mathrm{TF}_2(x, y; l)$ is a density profile of BEC in a harmonic trap obtained using Thomas-Fermi approximation:

$$\mathrm{TF}_2(x,y;l) \equiv \left[\max\left(1 - \frac{x^2+y^2}{l^2}, 0\right)\right]^{3/2} \tag{4.5}$$

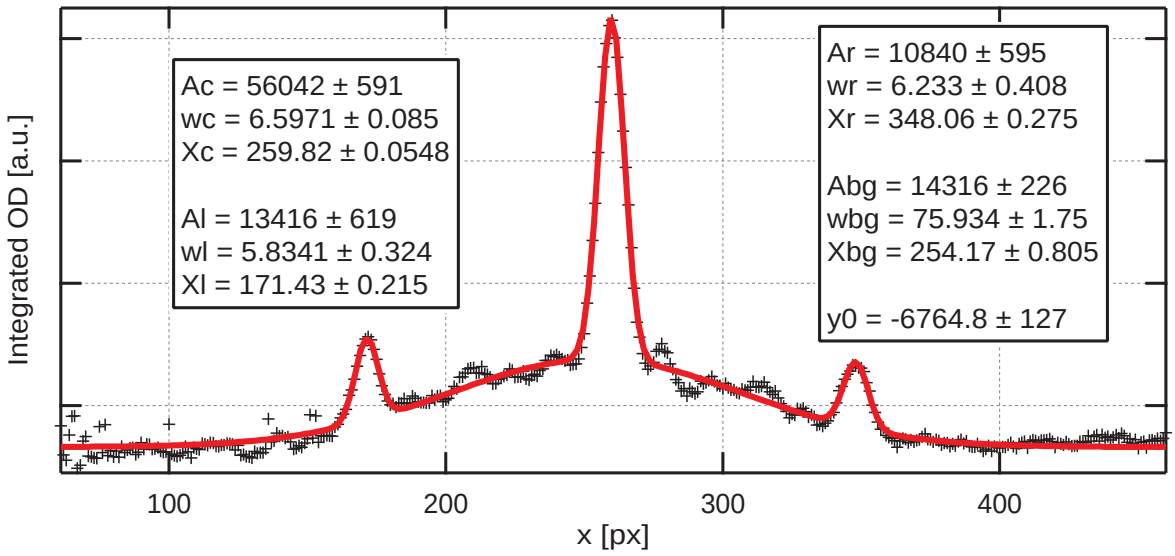

Figure 4.7: Curve fitting on interference pattern by Path (A). 1 px (pixel) corresponds to 4.0(2) μm.

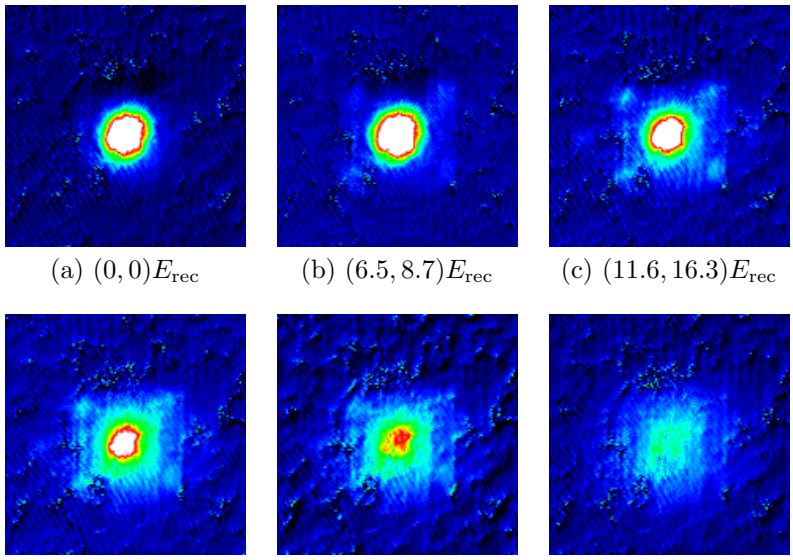

(a) $(0, 0)E_{\mathrm{rec}}$ (b) $(6.5, 8.7)E_{\mathrm{rec}}$ (c) $(11.6, 16.3)E_{\mathrm{rec}}$

(d) $(18.2, 26.6)E_{\mathrm{rec}}$ (e) $(22.8, 33.2)E_{\mathrm{rec}}$ (f) $(34.4, 49.3)E_{\mathrm{rec}}$

Figure 4.8: Interference pattern of a 2D arrays of 1D BEC.

where l is a parameter of the function TF_2 denoting the circular radius of the region filled with a condensate. Here, we assumed that the harmonic trap is isotropic in xy-plane. The derivation of this function is as follows; we have a anisotropic parabolic density profile $n(x, y, z) = n_0 \cdot \mathrm{TF}_3(x, y, z; l_x, l_y, l_z)$, where $n_0 = \mu/U_0$ is the peak density[*1] of the condensate and the function TF_3 is defined as

$$\mathrm{TF}_3(x, y, z; l_x, l_y, l_z) = \max\left(1 - \left(\frac{x}{l_x}\right)^2 - \left(\frac{y}{l_y}\right)^2 - \left(\frac{z}{l_z}\right)^2, 0\right) \tag{4.6}$$

where three parameters d_x, d_y and d_z denotes the radius of the region in the parabola filled with a condensate. In Thomas-Fermi approximation, kinetic energies of atoms are approximated to zero because it is far smaller than the mean-field energy due to interatomic interactions. By absorption imaging, the density profile is integrated along the axis of propergation of a probe laser beam. Therefore we integrate TF_3 along (for example) z-axis,

$$\int_{-\infty}^{\infty} \mathrm{TF}_3(x, y, z; l_x, l_y, l_z)dz = \int_{-l_z\sqrt{1-(x/l_x)^2-(y/l_y)^2}}^{l_z\sqrt{1-(x/l_x)^2-(y/l_y)^2}} \left[1 - \left(\frac{x}{l_x}\right)^2 - \left(\frac{y}{l_y}\right)^2 - \left(\frac{z}{l_z}\right)^2\right] dz \tag{4.7}$$

[*1] in fact, n_0 can be probed to be equal to μ/U_0, where μ is chemical potential of the atomic cloud and U_0 is the strength of δ-like pseudopotential resulting from interatomic interaction.

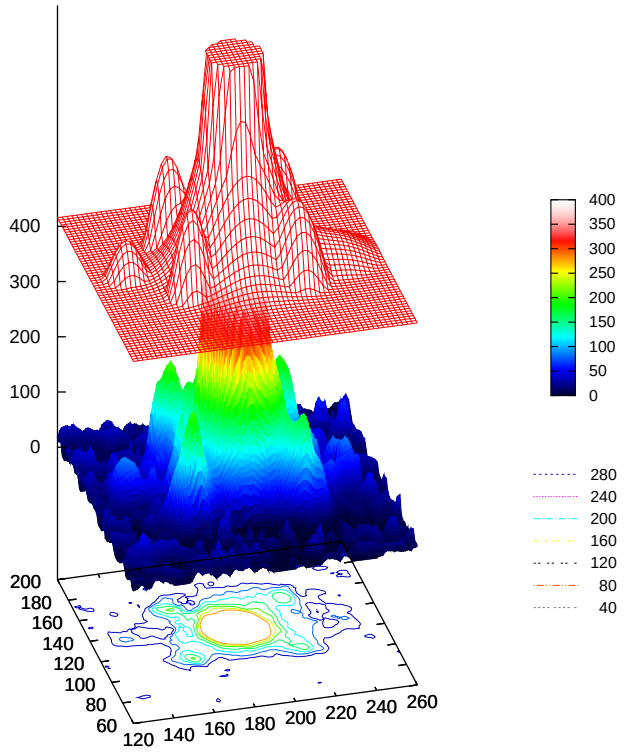

Figure 4.9: Example of curve fitting on the absorption image obtained above.

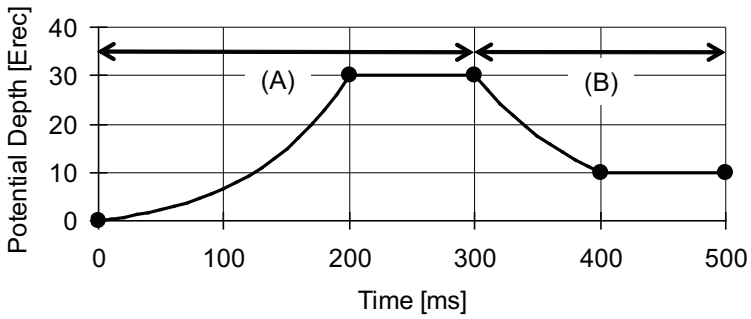

Figure 4.10: Typical time sequence of ramping up and down of the optical lattice.

One can observe that the curve (surface) agrees well with the OD except in the middle-right region. There S/N ratio is not good and one cannot expect good results of curve fitting. The four diffracted components have almost same sizes, with only a slight difference in the lower right peak.

In Figure 4.9, we show three examples of curve fitting, corresponding to (b), (d), and (e) in Figure 4.8. The middle, colored surface is obtained by averaging over nearest 5×5 pixels around a particular pixel in order to reduce noise. As one can see in Figure 4.8, the typical length scale in the original images is more than 10 pixels, so the averaging process does no harm. The lower plane shows a contour plot of the middle surface. The seven countours correspond indicates levels with OD of $\{40, 80, \ldots, 280\}$. The upper mesh is a plot of the result of curve fitting. For visual clarity, the mesh is shifted upwards from the surface. The top of the surface is cropped because the center peak is so high that other lower peaks become hard to see in the figure if it is entirely shown.

A typical sequence is shown in Figure 4.10. The images shown in Figure 4.8 are taken by ToF of 30.7 ms just after the sequence (A), with peak potential depth ($30E_{\mathrm{rec}}$ in the above) varied. We also observed a sharp peak like (a) in Figure 4.8 by ToF after the sequence (B). The peak potential depth was $100E_{\mathrm{rec}}$ at that time.

The TOF image obtained after raising the barrier between sites in the optical lattice shows that there is no coherence between sites. Therefore we conclude that Mott insulator phase is realized. The characteristic time for quantum tunneling τ is estimated to be order of 10 to 100 seconds.

Parameter	Value (d')
A_c	692(5)
l_c	16.85(4)
(X_c, X_c)	(182.2(2),134.3(2))
A_1	125(2)
l_1	13.4(1)
(X_1, Y_1)	(218.62(9),157.6(9))
A_2	141(2)
l_2	11.6(1)
(X_2, Y_2)	(162.42(8),159.30(8))
A_3	135(2)
l_3	11.4(1)
(X_3, Y_2)	(161.61(8),112.33(8))
A_4	115(2)
l_4	14.0(1)
(X_4, Y_2)	(216.7(1),110.6(1))
A_{23}	64(2)
l_{23}	11.3(2)
(X_{23}, Y_{23})	(137.1(2),137.4(2))
A_{bg}	420(3)
w_{bg}	21.66(9)
(X_{bg}, X_{bg})	(190.96(5),135.97(4))
y_0	15.7(2)

Table 4.3: Obtained values for fitting parameters.

Here we compare these results with those observed by Bloch *et al.*[90].

Chapter 5

Conclusion and Outlook

By the standard method, we obtained ^{41}K and ^{87}Rb BEC with the numbers of atoms of $N_{\mathrm{K}} = 3 \times 10^5$ and $N_{\mathrm{Rb}} = 4 \times 10^5$, respectively. Then we superimposed the one- and two-dimensional optical lattice on the ^{87}Rb condensate in the magnetic trap. After release from the combined trap, the condensate formed interferrence patterns. The shape of the patterns agreed well with the prediction from band theory. As the depth of the optical lattice is increased, the visibility of the patterns decreased and finally vanished. This is explained from the suppression of tunneling of atoms between neighboring sites in the optical lattice. Moreover, when we subsequently lowered the depth, the atomic cloud went back to the BEC. This is the proof that the dissapearance of the patterns is not caused by the heating up the atomic cloud. Therefore we conclude that our optical lattice can be used for its final objecitive, namely, confining the mixture of BECs of ^{87}Rb and ^{41}K to produce ultracold heteronuclear molecules by combination of Feshbach resonance and STIRAP.

Appendix A

Theoretical Techniques

Here we describe some of the relevant points to analyze properties of BEC in a optical lattice.

A.1 Classical Optics

A.1.1 ABCD-matrix

Wide range of optical systems can be described in terms of the so-called ABCD-matrices. See standard textbooks such as Yariv [91] for its details.

We define the co-called *q-parameter* $q(z)$, also known as the *complex curvature*, of a Gaussian beam via

$$\frac{1}{q(z)} \equiv \frac{1}{R(z)} - i\frac{\lambda}{\pi w^2(z)} = \frac{1}{z + iz_{\mathrm{R}}}. \tag{A.1}$$

(The last equality follows from the definitions of $R(z)$ and $w(z)$.) Then the effect of an optical apparatus located at z_0 can be written as

$$q'(z - z_0) = \frac{A \cdot q(z - z_0) + B}{C \cdot q(z - z_0) + D} \qquad \left(\text{or, equivalently, } \frac{1}{q'(z - z_0)} = \frac{D/q(z - z_0) + C}{B/q(z - z_0) + A}\right), \tag{A.2}$$

where $q'(z)$ is the q-parameter of the transformed beam, and $A, \ldots, D$ are elements of the ABCD-matrix for that apparatus. That is, by requiring continuity of the q-parameter $q(z)$ for the original beam and $q'(z)$ for the transformed beam at z_0, we obtain the complete specification, *e.g.*, both of the radius w_0' at the beam waist and the Rayleigh length z_{R}', of the transformed beam. Let M_{L} denote an ABCD-matrix for a lens with focal length f. Its elements are given as follows:

$$M_{\mathrm{L}} \equiv \begin{pmatrix} A_{\mathrm{L}} & B_{\mathrm{L}} \\ C_{\mathrm{L}} & D_{\mathrm{L}} \end{pmatrix} = \begin{pmatrix} 1 & \\ -1/f & 1 \end{pmatrix}. \tag{A.3}$$

Moreover, a concave mirror can be treated as a lens, when we define the coordinate system for the reflected beam so that z-axis points the opposite direction of that of the original system.

A.1.2 Effect of thin lens on Gaussian beam

The elementary folmula of the effect of lens is as follows: We are familiar with the

$$\frac{1}{a} + \frac{1}{b} = \frac{1}{f}. \tag{A.4}$$

Here, a and b are respectively the distance between foci and the lens for the incident and transmitted beams. This may be called the *ray approximation*, since this formula assumes that the wave propagates as ray and ignores the finite diameter of the beam waist. By introducing "normalized" lengths

$$\tilde{a} \equiv \frac{a}{f}, \qquad \tilde{b} \equiv \frac{b}{f}, \tag{A.5}$$

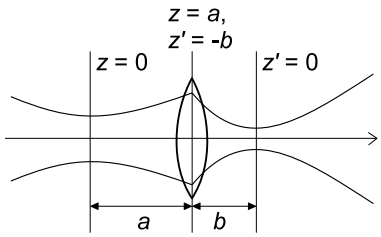

Figure A.1: Coordinate systems to derive the lens formula for Gaussian beams.

we have a more symmetric form of Eq. (A.4) as

$$\tilde{b} = \frac{\tilde{a}}{\tilde{a}-1}. \tag{A.6}$$

Additionally, further transformation leads to $\tilde{b} - 1 = 1/(\tilde{a}-1)$, revealing that it is a hyperbola with its origin at $(\tilde{a}, \tilde{b}) = (1, 1)$.

We want a similar formula for Gaussian beams which propagates through free space under the effect of diffraction. This can be treated using ABCD-matrices as follows. First, we set up coordinate systems for the original and transformed beams, as shown in Figure A.1. Then at the location of a lens, where both $z = a$ and $z' = -b$ are satisfied, we have

$$q'(z'=-b) = \frac{A\cdot q(z=a)+B}{C\cdot q(z=a)+D} \iff -b + iz'_{\mathrm{R}} = \frac{a+iz_{\mathrm{R}}}{(-1/f)(a+iz_{\mathrm{R}})+1}, \tag{A.7}$$

where z'_{R} represents the Rayleigh length of the transformed beam. Dividing both sides by f, we obtain

$$-\tilde{b} + i\tilde{z_{\mathrm{R}}}' = \frac{\tilde{a}+i\tilde{z_{\mathrm{R}}}}{1-\tilde{a}-i\tilde{z_{\mathrm{R}}}} = \frac{(\tilde{a}+i\tilde{z_{\mathrm{R}}})(1-\tilde{a}+i\tilde{z_{\mathrm{R}}})}{(\tilde{a}-1)^2+\tilde{z_{\mathrm{R}}}^2} = \frac{\tilde{a}(1-\tilde{a})-\tilde{z_{\mathrm{R}}}^2+i\tilde{z_{\mathrm{R}}}}{(\tilde{a}-1)^2+\tilde{z_{\mathrm{R}}}^2}, \tag{A.8}$$

where $\tilde{z_{\mathrm{R}}} \equiv z_{\mathrm{R}}/f$ and $\tilde{z_{\mathrm{R}}}' \equiv z'_{\mathrm{R}}/f$. Comparing real and imaginary parts of both sides yields the following two equations:

$$\tilde{b} = \frac{\tilde{a}(\tilde{a}-1)+\tilde{z_{\mathrm{R}}}^2}{(\tilde{a}-1)^2+\tilde{z_{\mathrm{R}}}^2}, \tag{A.9a}$$

$$z'_{\mathrm{R}} = \frac{z_{\mathrm{R}}}{(\tilde{a}-1)^2+\tilde{z_{\mathrm{R}}}^2} \iff w'_0 = \frac{w_0}{\sqrt{(\tilde{a}-1)^2+\tilde{z_{\mathrm{R}}}^2}}. \tag{A.9b}$$

Here, the beam waist size w'_0 of the transformed beam satisfies $z'_{\mathrm{R}} = \lambda/(\pi w_0'^2)$.

By comparing Eqs. (A.6) and (A.9a), we see the effect of Gaussian beam, or effect by Fraunhofer diffraction. The difference becomes significant when $a \to f \iff \tilde{a} \to 1$. In the ray approximation, we have $\tilde{b} \to \infty$; *i.e.*, the focal point can be as far as possible. However, in the Gaussian case, we have $\tilde{b} \to 1 \iff b \to f$ because of $\tilde{z_{\mathrm{R}}}$ in both of the numerator and the denominator. In Figure A.2, Note that this plot does not depend on wavelength of the Gaussian beam. Note also that in the limit of long focal length ($\tilde{z_{\mathrm{R}}} \equiv z_{\mathrm{R}}/f \to 0$,) the effect of diffraction is negligible, thus Eq. (A.9a) reduces to Eq. (A.6).

A.1.3 Numerical evaluation

Since the equation we want to solve is a general cubic equations in z, we should use numerical rather than analytic (symbolic) solutions. Though the latter may be computable by the use of CAS (compter algebra systems,) it is slower and do not have advantage over the former, since we eventually need a numerical value for z. However, there is one thing we care about; among multiple solutions for z, we need to find a "physical" one which leads to positive values for distances between various lenses and foci. Numerical solutions often finds only one of multiple solutions for z. Even if multiple solutions can be simultaneously obtained, there is no difference in that we can often use only one of these solutions.

In order to do so, we begin with parameters for which an obviouslly correct solution can be obtained. Then we slightly vary parameters towards the final value and calculate the corresponding solution. The solution can be used for the seed value for the next calculation with parameters which are more closer to the final values. By repeatedly varying parameters and the seed value for z, we may finally obtain a solution for the condition under consideration.

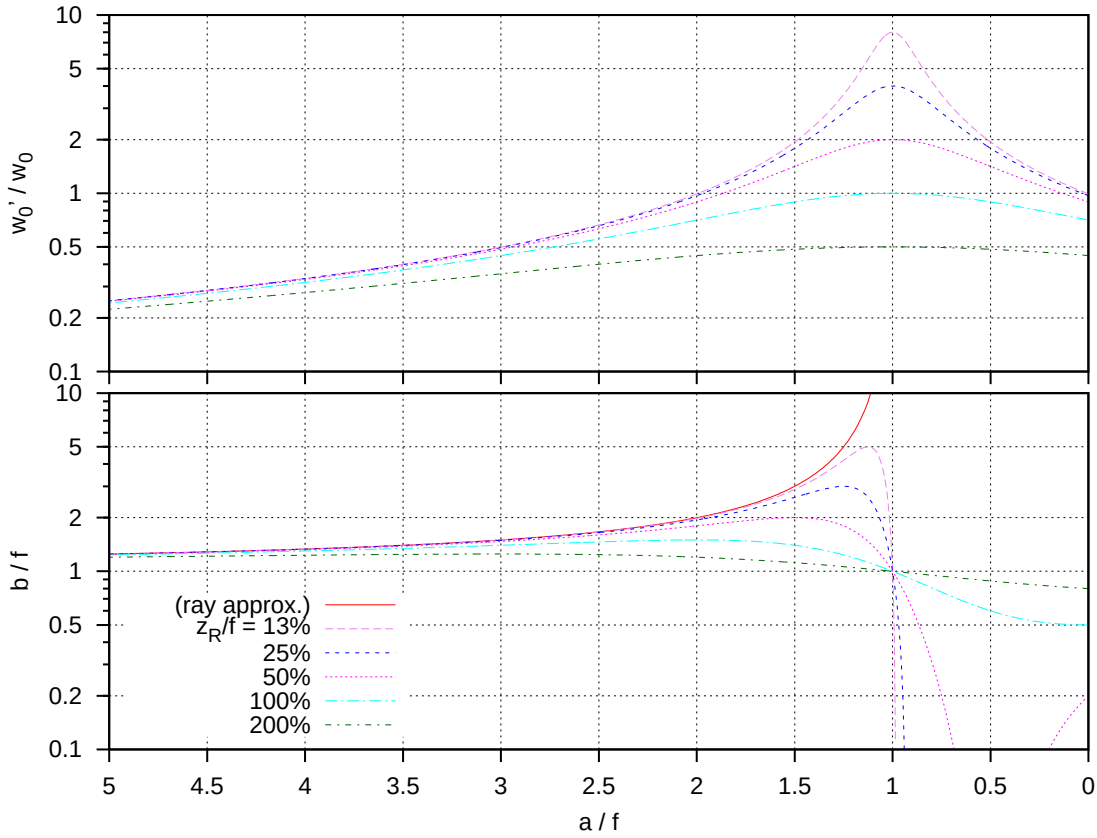

Figure A.2: Plot of Eqs. (A.9).

The following codes can be used to calculate the optimal value for z under fixed parameters. We used GNU Maxima which is a free software. Visit the website of GNU Maxima `http://maxima.sf.net/` for details. However, there are less information on this CAS, so we present the code with comments.

```
lambda:1064e-3 $    ← GNU Maxima denotes asignment by ':' and end of a command by '$'.
new_loc(a,f,w0):=  (  a/f * (a/f-1)    ← ':=' is used to define a function.
                    + (%pi * w0^2 /lambda /f)^2 )
                 / (  (a/f-1)^2    ← Spaces and line-breaks may be inserted anywhere you like.
                    + (%pi * w0^2 /lambda /f)^2 ) $
new_wid(a,f,w0):= w0 / sqrt(  (a/f-1)^2
                            + (%pi * w0^2 /lambda /f)^2 ) $
load(mnewton) $    ← Loading package for Newton's iteration method with multiple variables
fpprintprec:5 $    ← "floating-point-number print precicision" is set to 5 digits.

block(    ← The block clause introduces local variables*1.
[a:93, w0:0.36, L:730, f1:50, f2:100, w02:0.125], ← Asigning values to the local variables.
    mnewton([  b+c+d+e - L,        ← Execution of the mnewton function (See below.)
               c/f1 - new_loc(b-a,f1,w0),
               w01 - new_wid(b-a,f1,w0),
               e/f2 - new_loc(d,f2,w01),
               w02 - new_wid(d,f2,w01)   ],
    [b, c, d, e, w01],[0, 50, 130, 510, 0.05])
);    ← To print a value, use ; at the end of a command instead of $.
```

The function `mnewton([`$e_1,\ldots,e_n$`],[`$v_1,\ldots,v_n$`],[`$i_1,\ldots,i_n$`])` executes Newton's method to find the values of variables $v_1,\ldots,v_n$ for which all expressions $e_1,\ldots,e_n$ vanish, with the initial values of variables set to $i_1,\ldots,i_n$. To solve the coupled equations $f_k(v_1,\ldots,v_n) = g_k(v_1,\ldots,v_k)$ $(k = 1,\ldots,n)$, choose

*1The variables which are "local" to a block cannot be referred outside of that block. They are advantageous in that they are less likely to be confused with variables which accidentally have the same name but are used with different meanings.

$f_k(v_1, \ldots, v_n) - g_k(v_1, \ldots, v_k)$ as e_k.

A.2 Time-dependent Perturbation Theory

Details are found in standard textbooks on quantum field theory. We recommend those written for application for condensed matter systems Feynman [92].

We work out in the convenient *interaction picture* which eliminates obvious dependence on the unperturbed states from calculations. Remember the two different pictures of quantum mechanics: the Schrödinger picture in which state vectors are responsible for all time-dependences, and the Heisenberg picture in which states are time-independent and instead observables carries all time-dependences. Both of the two pictures yield the same value for the expectation values $\langle A \rangle_\psi$ of an observable A for the state ψ:

$$\langle A \rangle_\psi = \langle \psi | A | \psi \rangle. \tag{A.10}$$

If the introduction of the time-dependence is necessary, we can use both of the above two pictures:

$$\langle A \rangle_\psi(t) = \langle \psi(t) | A | \psi(t) \rangle \quad \text{(Schrödinger)} \tag{A.11a}$$
$$= \langle \psi | A(t) | \psi \rangle. \quad \text{(Heisenberg)} \tag{A.11b}$$

Here, $|\psi(t)\rangle$ is defined as the vector which experienced the time-evolution due to (total) Hamiltonian $\mathcal{H}$ from the initial value $|\psi_0\rangle$; that is, $|\psi(t)\rangle \equiv e^{-i\mathcal{H}t/\hbar}|\psi_0\rangle$. However, in performing the time-dependent perturbation for the Hamiltonian $\mathcal{H} = \mathcal{H}_0 + V$, there is a third way to introduce the time-dependence. Beginning with, for example, the Schrödinger picture,

$$\langle A \rangle_\psi(t) = \langle \psi(t) | e^{-i\mathcal{H}_0 t/\hbar} e^{i\mathcal{H}_0 t/\hbar} A e^{-i\mathcal{H}_0 t/\hbar} e^{i\mathcal{H}_0 t/\hbar} | \psi(t) \rangle \equiv \langle \psi^{\mathrm{I}}(t) | A^{\mathrm{I}}(t) | \psi^{\mathrm{I}}(t) \rangle, \tag{A.12}$$

where we defined

$$|\psi^{\mathrm{I}}(t)\rangle \equiv e^{i\mathcal{H}_0 t/\hbar} |\psi(t)\rangle, \tag{A.13a}$$
$$A^{\mathrm{I}}(t) \equiv e^{i\mathcal{H}_0 t/\hbar} A e^{-i\mathcal{H}_0 t/\hbar}. \tag{A.13b}$$

The definitions of $|\psi^{\mathrm{I}}(0)\rangle$ can be understood as follows: In the simplest case of commuting $\mathcal{H}_0$ and V, we have

$$|\psi^{\mathrm{I}}(t)\rangle = e^{i\mathcal{H}_0 t/\hbar} e^{-i(\mathcal{H}_0 + V)t/\hbar} |\psi_0\rangle = e^{-iVt/\hbar} |\psi_0\rangle. \tag{A.14}$$

Thus this can be seen as a solution of the Schrödinger equation with the Hamiltonian V but without $\mathcal{H}_0$. Of cource, things are more complicated in the general case, because $[a, b] \neq 0$ implies $e^a e^b \neq e^{a+b}$. However it remains correct to understand its essence as removing the obvious dynamics due to the unperturbed Hamiltonian.

We can translate the Schrödinger equation into the interaction picture by substitution of $|\psi(t)\rangle$ with $e^{-i\mathcal{H}_0 t/\hbar}|\psi^{\mathrm{I}}(t)\rangle$:

$$i\hbar \partial_t e^{-i\mathcal{H}_0 t/\hbar} |\psi^{\mathrm{I}}(t)\rangle = (\mathcal{H}_0 + V) e^{-i\mathcal{H}_0 t/\hbar} |\psi^{\mathrm{I}}(t)\rangle \iff e^{-i\mathcal{H}_0 t/\hbar} i\hbar \partial_t |\psi^{\mathrm{I}}(t)\rangle = V e^{-i\mathcal{H}_0 t/\hbar} |\psi^{\mathrm{I}}(t)\rangle$$
$$\iff i\hbar \partial_t |\psi^{\mathrm{I}}(t)\rangle = V^{\mathrm{I}}(t) |\psi^{\mathrm{I}}(t)\rangle. \tag{A.15}$$

Incorporating the boundary condition $|\psi^{\mathrm{I}}(t = t_0)\rangle = |\psi_0\rangle$, this differential equation can be rewritten to the integral equation:

$$\int_{t0}^{t} \partial_t |\psi^{\mathrm{I}}(t)\rangle dt$$
$$= |\psi^{\mathrm{I}}(t)\rangle - |\psi_0\rangle = \frac{1}{i\hbar} \int_{t0}^{t} dt V^{\mathrm{I}}(t) |\psi^{\mathrm{I}}(t)\rangle. \tag{A.16}$$

In order to solve this equation, we introduce a unitary operator $U(t, t_0)$ called *propagator* such that $|\psi^{\mathrm{I}}(t)\rangle = U(t, t_0)|\psi_0\rangle$. By substitution, we have the following integral equation for the propagator:

$$[U(t, t0) - 1]|\psi_0\rangle = \frac{1}{i\hbar} \int_{t0}^{t} dt\, V^{\mathrm{I}}(t) U(t, t_0) |\psi_0\rangle$$
$$\iff U(t, t_0) - O[U(t, t_0)] = 1 \iff U(t, t_0) = (1 - O)^{-1} \tag{A.17}$$

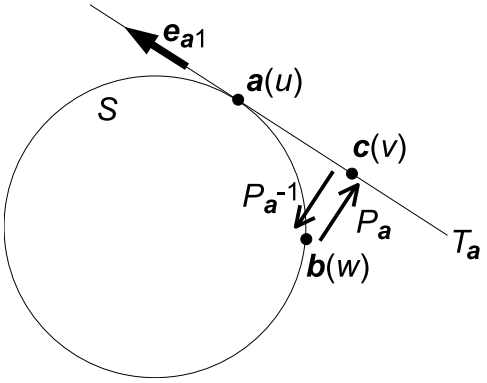

Figure A.3: A one-to-one correspondance between a parametrized surface and its tangent plane.

where we have defined the integral operator O as

$$O[f(t)] \equiv \frac{1}{i\hbar}\int_{t0}^{t} dt\, V^{\mathrm{I}}(t) f(t). \tag{A.18}$$

Here we used t both as the upper limit and as the formal variable of the integration. Their meanings should be understood from the context. Using the familiar expression $(1-a)^{-1} = \sum_{n\geq 0} a^n$ for the geometric series, we have the following formal expansion:

$$U(t,t_0) = \sum_n \frac{1}{(i\hbar)^n}\int_{t0}^{t} dt_n \int_{t0}^{tn} dt_{n-1} \cdots \int_{t0}^{t2} dt_1\, V^{\mathrm{I}}(t_n)V^{\mathrm{I}}(t_{n-1})\cdots V^{\mathrm{I}}(t_1) \tag{A.19}$$

Usually we truncate the infinite sum at the first few terms. Alternatively, we can obtain this formal expansion by iterated substitution. Beginning with Eq. (A.17), we have

$$U(t,t_0) = 1 + O[U(t,t_0)] = 1 + O\{1 + O[U(t,t_0)]\} = 1 + O(1 + O\{1 + O[U(t,t_0)]\}) = \ldots, \tag{A.20}$$

and we can go *ad infinitum*. Again, after a few iteration of substitution, we truncate the infinite sum by substitution of $U(t,t_0)$ with 1. These formal series expansion has the advantage of being able to control how many orders of perturbative term we incorporate in the calculation, and t need not be small. For a theoretical interest, we explain how to use the superoperator of *time-ordering product* $\mathcal{T}$.

$$\begin{aligned}
&\int_{t0}^{t} dt_n \int_{t0}^{tn} dt_{n-1} \cdots \int_{t0}^{t2} dt_1\, V^{\mathrm{I}}(t_n)V^{\mathrm{I}}(t_{n-1})\cdots V^{\mathrm{I}}(t_1) \\
&= \frac{1}{n!}\int_{t0}^{t} dt_n \int_{t0}^{t} dt_{n-1} \cdots \int_{t0}^{t} dt_1\, \mathcal{T}[V^{\mathrm{I}}(t_n)V^{\mathrm{I}}(t_{n-1})\cdots V^{\mathrm{I}}(t_1)]
\end{aligned} \tag{A.21}$$

(A.19)

A.3 n-dimensional Laplacian and Laplace-Beltrami operator

For the arbitrary n-dimensional space ($n \geq 2$,) the Laplacian can always be split into the radial part

$$\frac{1}{r^{n-1}}\partial_r r^{n-1}\partial_r = \partial_r^2 + \frac{n-1}{r}\partial_r \tag{A.22}$$

and the angular part (the Laplace-Beltrami operator) which is free of r and ∂_r. Though this may be proven by a differential geometric calculation based on a metric tensor which gives a complete characterization of an arbitrary surface embedded in the n-dimensional space, it is somewhat lengthy. Instead we give a concise proof focusing on the above relation, following Matano and Jimbo [93].

A.3.1 Gradient operator on a surface

First, we define the gradient operator on a surface. Let S denote an arbitrary $(n-1)$-dimensional smooth surface embedded in the n-dimensional space. For each point $\boldsymbol{a}$ on S, there corresponds a pair $(T_{\boldsymbol{a}}, P_{\boldsymbol{a}})$ where $T_{\boldsymbol{a}}$ is a $(n-1)$-dimensional tangent plane of S at $\boldsymbol{a}$ and $P_{\boldsymbol{a}}$ is a projection from S onto T_a. Because

S is "smooth," there is a finite region around $\boldsymbol{a}$ where $P_{\boldsymbol{a}} : S \to T_{\boldsymbol{a}}$ is not only a projection but also a one-to-one correspondance, and we can go back from $\boldsymbol{c} \equiv P_{\boldsymbol{a}}(\boldsymbol{b}) \in T_{\boldsymbol{a}}$ to the original $\boldsymbol{b} \in S$. ($P_{\boldsymbol{a}}$ is not a one-to-one correspondance only in a region where S and $T_{\boldsymbol{a}}$ are vertical or where a part of S away from $\boldsymbol{a}$ is folded to lie between $\boldsymbol{a}$ and $T_{\boldsymbol{a}}$; See Figure A.3.) Then for any function $f : S \to \mathbb{R}$ and any point $\boldsymbol{a}$ on S, one can associate a composite function $\tilde{f} : T_{\boldsymbol{a}} \to \mathbb{R}$ defined as

$$\tilde{f}(\boldsymbol{c}) \equiv f(\boldsymbol{b}) \equiv f(P_{\boldsymbol{a}}^{-1}(\boldsymbol{c})). \tag{A.23}$$

Since $T_{\boldsymbol{a}}$ is just a $(n-1)$-dimensional Euclidean space, there is no difficulty in calculating the gradient of $\tilde{f}$ at $\boldsymbol{a} \in T_{\boldsymbol{a}}$:

$$\nabla_{T\boldsymbol{a}}\tilde{f}(\boldsymbol{c}=\boldsymbol{a}) \equiv {}^t\left(\ldots, \lim_{h\to 0}\frac{\tilde{f}(\boldsymbol{a}+h\boldsymbol{e}_{\boldsymbol{a}j}) - \tilde{f}(\boldsymbol{a})}{h}, \ldots \right). \tag{A.24}$$

Here, the right hand side is a $(n-1)$-dimensional vector with its j-th element corresponding to directional derivative along j-th basis vector $\boldsymbol{e}_{\boldsymbol{a}j}$ of $T_{\boldsymbol{a}}$. Then this is used to define the gradient operator for $u : S \to \mathbb{R}$; *i.e.*, for each $\boldsymbol{a}$ in S (the domain of f,) we construct a tangent space $T_{\boldsymbol{a}}$ and define the gradient of f on S, or $\nabla_S f(\boldsymbol{a})$, as the gradient of $\tilde{f}$ on $T_{\boldsymbol{a}}$, or $\nabla_{T\boldsymbol{a}}\tilde{f}(\boldsymbol{c})\big|_{\boldsymbol{c}=\boldsymbol{a}}$.

Example: We choose the one-dimensional unit sphere S^1 as S. Then S as a subset of $\mathbb{R}^2$ can be parametrized by $u \in (-1 \ldots 1)$ as

$$S \ni \boldsymbol{a}(u) = {}^t(x(u), y(u)) = \begin{cases} {}^t(u, \pm\sqrt{1-u^2}) & (-1 < x < 1 \text{ and } y \gtrless 0), \\ {}^t(\pm\sqrt{1-u^2}, u) & (-1 < y < 1 \text{ and } x \gtrless 0). \end{cases} \tag{A.25}$$

Each of these four ways of parametrization covering its own region of S is called a *chart* of S, and the whole set of charts is collectively called the *atlas* of S. For the case of the first chart, the tangent space $T_{\boldsymbol{a}}$ is parametrized by $v \in \mathbb{R}$ as

$$T_{\boldsymbol{a}} \ni \boldsymbol{c}(v) = \begin{pmatrix} c_1(v) \\ c_2(v) \end{pmatrix} = \begin{pmatrix} u - \sqrt{1-u^2}v \\ \sqrt{1-u^2} + uv \end{pmatrix}. \tag{A.26}$$

This parametrization indeed satisfies $\overrightarrow{O\boldsymbol{a}} \cdot \overrightarrow{\boldsymbol{ac}} = 0$. Since $T_{\boldsymbol{a}}$ is a one-dimensional space, there is only one vector $\boldsymbol{e}_{\boldsymbol{a}1}$ in a basis of $T_{\boldsymbol{a}}$. For $\boldsymbol{e}_{\boldsymbol{a}1}$, we choose

$$\boldsymbol{e}_{\boldsymbol{a}1} \equiv \begin{pmatrix} -\sqrt{1-u^2} \\ u \end{pmatrix}. \tag{A.27}$$

Note that $\boldsymbol{c}(v)$ can be expressed as $\boldsymbol{a} + v\boldsymbol{e}_{\boldsymbol{a}1}$. Then the gradient operator on $T_{\boldsymbol{a}}$ is expressed as

$$\nabla_{T\boldsymbol{a}} g(\boldsymbol{c}) = \lim_{h\to 0}\frac{g(\boldsymbol{c}+h\boldsymbol{e}_{\boldsymbol{a}1}) - g(\boldsymbol{c})}{h} = \boldsymbol{e}_{\boldsymbol{a}1} \cdot \nabla g(c_1, c_2) = -\sqrt{1-u^2}\frac{\partial g}{\partial c_1}(c_1, c_2) + u\frac{\partial g}{\partial c_2}(c_1, c_2). \tag{A.28}$$

In order to express the gradient operator on S using the above result, we first express the projection from S onto $T_{\boldsymbol{a}}$. That can be done by inner product with $\boldsymbol{e}_{\boldsymbol{a}1}$. For another point $\boldsymbol{b}$ in S whose parameter is w, the projection is

$$\begin{aligned} P_{\boldsymbol{a}}\boldsymbol{b} &\equiv \boldsymbol{a} + [\boldsymbol{e}_{\boldsymbol{a}1} \cdot (\boldsymbol{b}-\boldsymbol{a})]\boldsymbol{e}_{\boldsymbol{a}1} = \boldsymbol{a} + \left[{}^t\begin{pmatrix} -\sqrt{1-u^2} \\ u \end{pmatrix} \begin{pmatrix} w-u \\ \sqrt{1-w^2} - \sqrt{1-u^2} \end{pmatrix} \right] \boldsymbol{e}_{\boldsymbol{a}1} \\ &= \boldsymbol{a} + (u\sqrt{1-w^2} - \sqrt{1-u^2}w)\boldsymbol{e}_{\boldsymbol{a}1}. \end{aligned} \tag{A.29}$$

Its inverse $P_{\boldsymbol{a}}^{-1}$ is obtained by equating the above expression with $\boldsymbol{c}(v)$ and solving for w. That amounts to equating coefficients of $\boldsymbol{e}_{\boldsymbol{a}1}$:

$$v = u\sqrt{1-w^2} - \sqrt{1-u^2}w \qquad \therefore w = u\sqrt{1-v^2} - \sqrt{1-u^2}v. \tag{A.30}$$

Then we have

$$P_{\boldsymbol{a}}^{-1}[\boldsymbol{c}(v)] = \boldsymbol{b}(w = u\sqrt{1-v^2} - \sqrt{1-u^2}v) = \begin{pmatrix} u\sqrt{1-v^2} - \sqrt{1-u^2}v \\ \sqrt{1-u^2}\sqrt{1-v^2} + uv \end{pmatrix} = \sqrt{1-v^2}\boldsymbol{a} + v\boldsymbol{e}_{\boldsymbol{a}1}. \tag{A.31}$$

This is a function of the parameter v of $\boldsymbol{c}$. Using $\boldsymbol{c}(v) = \boldsymbol{a} + v\boldsymbol{e}_{\boldsymbol{a}1}$, we can express v as the function of $\boldsymbol{c}$ as in $v = \boldsymbol{e}_{\boldsymbol{a}1} \cdot \boldsymbol{c}$. Then we can express $P_{\boldsymbol{a}}^{-1}$ as the function of $\boldsymbol{c}$:

$$P_{\boldsymbol{a}}^{-1}\boldsymbol{c} = \sqrt{1-(\boldsymbol{e}_{\boldsymbol{a}1} \cdot \boldsymbol{c})^2}\boldsymbol{a} + (\boldsymbol{e}_{\boldsymbol{a}1} \cdot \boldsymbol{c})\boldsymbol{e}_{\boldsymbol{a}1}. \tag{A.32}$$

Finally, using the results obtained so far, we have

$$\begin{aligned}\nabla_S f(\boldsymbol{a}) &= \nabla_{T\boldsymbol{a}} \tilde{f}(\boldsymbol{c}=\boldsymbol{a}) = \boldsymbol{e}_{\boldsymbol{a}1} \cdot \nabla \tilde{f}(\boldsymbol{c}=\boldsymbol{a}) = \boldsymbol{e}_{\boldsymbol{a}1} \cdot \frac{\partial P_{\boldsymbol{a}}^{-1}}{\partial \boldsymbol{c}}(\boldsymbol{c}=\boldsymbol{a}) \cdot \nabla f(\boldsymbol{a}) \\ &= \boldsymbol{e}_{\boldsymbol{a}1} \cdot \left(-\frac{0}{\sqrt{1-0^2}} \boldsymbol{a}\boldsymbol{e}_{\boldsymbol{a}1} + \boldsymbol{e}_{\boldsymbol{a}1}\boldsymbol{e}_{\boldsymbol{a}1} \right) \cdot \nabla f(\boldsymbol{a}) = |\boldsymbol{e}_{\boldsymbol{a}1}|^2 \begin{pmatrix} -\sqrt{1-u^2} \\ u \end{pmatrix}^t \begin{pmatrix} \partial f(a_1,a_2)/\partial a_1 \\ \partial f(a_1,a_2)/\partial a_2 \end{pmatrix} \\ &= -a_2 \frac{\partial f}{\partial a_1}(a_1,a_2) + a_1 \frac{\partial f}{\partial a_2}(a_1,a_2). \end{aligned} \tag{A.33}$$

During calculation, we used the *dyadic* notation; *e.g.*, $\boldsymbol{a}\boldsymbol{e}_{\boldsymbol{a}1}$ is a second-rank tensor which maps a vector $\boldsymbol{v}$ to another vector $\boldsymbol{a}(\boldsymbol{e}_{\boldsymbol{a}1} \cdot \boldsymbol{v})$. They originates as follows:

$$\frac{\partial P_{\boldsymbol{a}}^{-1}}{\partial \boldsymbol{c}}(\boldsymbol{c}) = \frac{\partial}{\partial \boldsymbol{c}} \left[\sqrt{1-(\boldsymbol{e}_{\boldsymbol{a}1} \cdot \boldsymbol{c})^2} \boldsymbol{a} + (\boldsymbol{e}_{\boldsymbol{a}1} \cdot \boldsymbol{c}) \boldsymbol{e}_{\boldsymbol{a}1} \right] = -\frac{\boldsymbol{e}_{\boldsymbol{a}1} \cdot \boldsymbol{c}}{\sqrt{1-(\boldsymbol{e}_{\boldsymbol{a}1} \cdot \boldsymbol{c})^2}} \boldsymbol{a}\boldsymbol{e}_{\boldsymbol{a}1} + \boldsymbol{e}_{\boldsymbol{a}1}\boldsymbol{e}_{\boldsymbol{a}1}. \tag{A.34}$$

The gradient operator on the one-dimensional surface S^1 (A.33) can be seen as derivative with respect to θ when we parametrize S^1 as $\{(\cos\theta, \sin\theta) \mid \theta \in [0 \dots 2\pi)\}$.

A.3.2 Proof of the theorem

The Laplace-Beltrami operator Δ_S on a arbitrary surface S can be defined as the operator such that the equation

$$\int_S (\nabla_S \psi) \cdot (\nabla_S u) d\sigma = -\int_S \psi \Delta_S u \, d\sigma \tag{A.35}$$

holds for arbitrary functions u and ψ on S. Here, $d\sigma$ denotes the surface element of S. Note that Δ_S is the derivative operator involving coordinates on the surface S only. This definition is delibarately made to look like the following identity (Green's theorem) involving the ordinary Laplacian:

$$\int_V (\nabla \psi) \cdot (\nabla u) dV = \int_{\partial V} \psi (\nabla u \cdot \boldsymbol{n}) dS - \int_V \psi \nabla^2 u \, dV = -\int_V \psi \nabla^2 u \, dV. \tag{A.36}$$

Here, ∂V denotes the boundary of the region V, which is large enough, and $\boldsymbol{n}$ denotes the normal vector pointing towards the outside of V. Moreover, ψ is assumed to have a finite support[*2]; this leads to the last equality, since V is so large that it contains $\operatorname{supp} f$.

A point $\boldsymbol{r}$ in the n-dimensional space $\mathbb{R}^n$ can be written as $\boldsymbol{r} = (r, \sigma)$, where r is the distance from the origin and σ is the direction of the point from the origin; *e.g.*, all the angular coordinates (coordinates except for r) in the n-dimensional spherical coordinates are collectively denoted by σ. Thus any function $f(\boldsymbol{r})$ in $\mathbb{R}^n$ can be seen as a function of r and σ; *i.e.*, $f(\boldsymbol{r}) = f(r, \sigma)$. Note that σ can be seen as a point on the $(n-1)$-dimensional sphere $S^{n-1} \equiv S$. Based the point of view stated above, we consider the following integral involving two arbitrary functions ψ and u, where we assume that ψ has a finite support:

$$\begin{aligned}\int_{\mathbb{R}n} \psi \nabla^2 u \, dV &= -\int_{\mathbb{R}n} (\nabla \psi) \cdot (\nabla u) dV = -\int_0^\infty dr \, r^{n-1} \int_S d\sigma (\nabla \psi) \cdot (\nabla u) \\ &= -\int_S d\sigma \int_0^\infty dr \, r^{n-1} (\partial_r \psi)(\partial_r u) - \int_0^\infty dr \, r^{n-1} \frac{1}{r^2} \int_S d\sigma \, (\nabla_S \psi) \cdot (\nabla_S u). \end{aligned} \tag{A.37}$$

Here we used the fact that n-dimensional volume element dV is written as $r^{n-1} dr d\sigma$, and the identity

$$(\nabla \psi) \cdot (\nabla u) = (\partial_r \psi)(\partial_r u) + \frac{1}{r^2} (\nabla_S \psi) \cdot (\nabla_S u). \tag{A.38}$$

Using integration by parts, we have

$$\int_0^\infty dr \, r^{n-1} (\partial_r \psi)(\partial_r u) = [r^{n-1} \psi (\partial_r u)]_{r=0}^\infty - \int_0^\infty dr \, \psi \partial_r [r^{n-1} (\partial_r u)]. \tag{A.39}$$

Here, the first term vanishes because of the assumption that ψ has a finite support. Thus, for the first term of Eq. (A.37), we have

$$-\int_S d\sigma \int_0^\infty dr \, r^{n-1} (\partial_r \psi)(\partial_r u) = \int_S d\sigma \int_0^\infty dr \, \psi \partial_r [r^{n-1} (\partial_r u)] = \int_{\mathbb{R}n} \frac{1}{r^{n-1}} \psi \partial_r [r^{n-1} (\partial_r u)] dV. \tag{A.40}$$

[*2] The *support* of a function f is the subset of the domain of f such that f is nonzero; $\operatorname{supp} f \equiv \{x \mid f(x) \neq 0\}$. "A function f with a finite support" means that f vanishes outside of some finite region.

For the second term of Eq. (A.37), we use the definition of the Laplace-Beltrami operator (A.35) to obtain

$$-\int_0^\infty dr\; r^{n-1}\frac{1}{r^2}\int_S d\sigma\; (\nabla_S\psi)\cdot(\nabla_S u) = \int_0^\infty dr\; r^{n-1}\frac{1}{r^2}\int_S d\sigma\; \psi\Delta_S u = \int_{\mathbb{R}n}\frac{1}{r^2}\psi\Delta_S u\, dV. \tag{A.41}$$

Using the above results, we have

$$\int_{\mathbb{R}n}\psi\nabla^2 u\; dV = \int_{\mathbb{R}n}\psi\left[\frac{1}{r^{n-1}}\partial_r(r^{n-1}\partial_r u) + \frac{1}{r^2}\Delta_S u\right] dV. \tag{A.42}$$

Since ψ is an arbitrary function, the terms in $[\cdots]$ must coincide with $\nabla^2 u$. Therefore we have proven the main theorem (A.22) of this appendix.

A.4 Contour Integral

Here we summarize how to calculate certain kinds of integrals using the technique of contour integration. See standard textbooks on complex analysis such as Ahlfors [94] for details. We racall that the contour integral $\oint_C f(z)dz$ of a function f defined on a closed path C in the complex plane $\mathbb{C}$ is defined through parametrization of C; *i.e.*, when we write each point z on C as $z(t)$ in terms of $t \in (a \ldots b)$, where the upper and lower limits a and b may be infinite, then

$$\oint_C f(z)dz \equiv \int_a^b f(z(t))\frac{dz}{dt}(t)dt. \tag{A.43}$$

We often split C into multiple curves (lines) $\{I_k \mid k = 0, 1, \ldots, n\}$ such that each curve I_k has its own parametrization $z_k(t) : (a_k \ldots b_k) \to I_k$ and the disjoint sum $\bigsqcup_k I_k$ coincides with C. Then we have

$$\oint_C f(z)dz = \sum_k \int_{a_k}^{b_k} f(z_k(t))\frac{dz_k}{dt}(t)dt. \tag{A.44}$$

The main reason for physicists to be interested in contour integration is that, it is often possible to calculate a difficult real definite integral $\int_l^u f(x)dx$ through a related contour integral which can be more easily calculated. In order to do so, we find an appropriate closed path C satisfying the following conditions:

1. C can be split into multiple curves $\{I_k\}$ such that
   (a) One of I_k's (say I_m) coincides with the domain of integration of the original integral: $I_m = (l \ldots u)$.
   (b) Complex integrals over curves other than I_m can be somehow calculated by standard techniques.
2. C contains only *poles*[*3] of f, rather than its essential singularities.

Then, because the contour integral $\oint_C f(z)dz$ can be calculated using the residue theorem explained below, we know the definite value of the integral $\int_l^u f(x)dx$ as

$$\int_l^u f(x)dx = \int_{I_m} f(x)dx = \oint_C f(z)dz - \sum_{k\neq m}\int_{I_k} f(z)dz. \tag{A.45}$$

The residue theorem is a strong theorem which states that a contour integral $\oint_C f(z)dz$ (for a simple[*4] closed path C) can be calculated as

$$\oint_C f(z)dz = 2\pi i\sum_{k=1}^{N}\mathrm{Res}(f, p_k), \tag{A.46}$$

where $\mathrm{Res}(f, p_k)$ is the *residue* of f at a pole p_k of f enclosed by C, and N is the total number of poles of f enclosed by C. Moreover, the residue $\mathrm{Res}(f, p)$ of f at its *pole* p with order n can be calculated as

$$\mathrm{Res}(f, p) = \frac{1}{(n-1)!}\lim_{z\to p}\frac{d^{n-1}}{dz^{n-1}}[(z-p)^n f(z)]. \tag{A.47}$$

[*3] A pole p of a function f with order n is a point in the domain of f such that f behaves as $f(z) \sim C/(z-p)^n$ around p for some C. However, at an essential singularity a of f, the behavior of f is something like "$C/(z-a)^\infty$." For example, the function $e^{1/z}$ has an essential singularity at $z = 0$.

[*4] A *simple* curve is a curve which does not intersect itself.

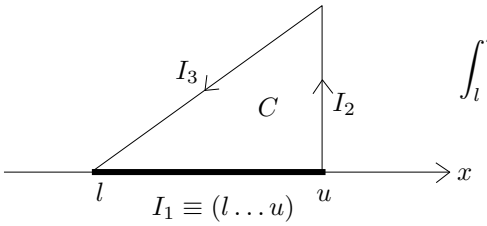

$$\int_l^u f(x)dx = \oint_C f(z)dz - \int_{a_2}^{b_2} f(z_2(t))\frac{dz_2}{dt}(t)dt - \int_{a_3}^{b_3} f(z_3(t))\frac{dz_3}{dt}(t)dt$$

Figure A.4: Calculation of a real definite integral through a contour integral.

This can be understood if we assume that f is expandable into the Laurent series $\sum_{n\in\mathbb{Z}} a_n(x-p)^n$ around p. Those theorems stated above can be proven by Cauchy's integral theorem, but we omit the proofs.

Various examples of the uses of the residue theorem can be found as excersises of complex analysis; see, *e.g.*, Spiegel [95]. Some of them have significance also in physics. For example, the Airy's integral used for decription of the Fraunhofer diffraction can be calculated in this way. Moreover, using the technique of contour integration, Wittig [96] gave a proof for the Landau-Zener formula

$$P = \exp\left(-2\pi\Omega\tau\right) \tag{A.48}$$

describing the probability of the diabatic transition in an time-dependent process. In the context of ultracold atomic physics, the Landau-Zener formula is important in ARP (adiabatic rapid passage) used to flip spin states of an atomic ensemble.

A.5 Mathieu equation

Here we explain mathematical properties of the *Mathieu equation*

$$\frac{d^2f}{dz^2}(z) + [a - 2q\cos(2z)]f(z) = 0. \tag{A.49}$$

Its details are found in the standard references like Sin [97, Sec. 10], Barrett [98], and Meixner and Schäfke [99].

The Mathieu equation is a homogeneous linear second-order differential equation characterized by the functional coefficient $[a - 2q\cos(2z)]$ of $f(z)$ with two parameters a and q. This form[*5] is particularly called the *normal form* of the equation. It was introduced by Mathieu [100] in 1868 in order to analyze the vibration of elliptical membranes. The equation is notorious for its difficultness in the field of differential equations. But by setting $q = 0$, it reduces to the familiar equation of a harmonic oscillator with frequency $\sqrt{a}$. Therefore we see that the difficulties arise from the "modulation" $2q\cos(2z)$.

In the context of ultracold atomic physics, its significance is twofold: (a) the classical equation of motion describing parametric oscillation of an atom confined in a time-dependent harmonic potential[*6], and (b) the Schrödinger equation of an atom moving within an optical lattice (mimicking that of an electron moving within a crystal lattice.) The case (a) is described by the time-domain Mathieu equation

$$m\frac{d^2x}{dt^2}(t) + [m\omega^2 + K_1\cos(\omega_1 t)]x(t) = 0, \tag{A.50}$$

where m is an atom's mass, $x(t)$ the location of the atom at time t, and ω the trap frequency of the harmonic trap $U(x) = m\omega^2x^2/2$ felt by the atom in the unmodulated case. Moreover, K_1 and ω_1 are respectively the amplitude and the frequency of amplitude modulation of the trap depth; *i.e.* the modulated trap potential $U_1(x)$ is written as

$$U_1(x) = U(x) + \frac{K_1}{2}x^2 = \frac{1}{2}[m\omega^2 + K_1\cos(\omega_1 t)]x^2. \tag{A.51}$$

Eq. (A.50) is obtained from the normal form (A.49) by the substitutions

$$f(z) = x(t), \qquad z = \frac{\omega_1}{2}t, \qquad a = \left(\frac{2\omega}{\omega_1}\right)^2, \qquad q = -2\frac{K_1}{m\omega_1^2}. \tag{A.52}$$

[*5] Unfortunately, different authors use different conventions for the Mathieu equation and related functions.
[*6] Jones [1] discusses its application in design of the Paul trap (a trap for ions.)

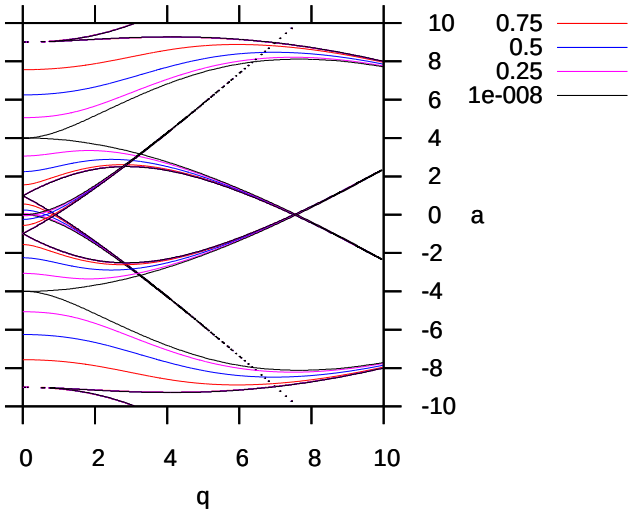

Figure A.5: Plot of stable regions of the Mathieu equation by the C proglam written by Jones [1].

The case (b) is described by the space-domain Mathieu equation

$$\left[-\frac{\hbar^2}{2m}\frac{d^2}{dx^2} + U\sin^2(kx)\right]\phi(x) = E\phi(x) \iff \frac{\hbar^2}{2m}\frac{d^2\phi}{dx^2}(x) + \left[E' + \frac{U}{2}\cos(2kx)\right]\phi(x) = 0, \tag{A.53}$$

where m is an atom's mass, $\phi(x)$ is Schrödinger's (time-independent and, in this case, 1D) wavefunction, $E \equiv E' + U/2$ is the energy eigenvalue, U and $2k = 2\pi/(\lambda/2)$ are respectively the depth and the wavenumber of the sinusoidal potential with period $\lambda/2$ felt by the atom. Eq. (A.53) is obtained from the normal form (A.49) by the substitutions

$$f(z) = \phi(x), \qquad z = kx, \qquad a = \frac{2mE'}{(\hbar k)^2}, \qquad q = -\frac{mU}{2(\hbar k)^2}. \tag{A.54}$$

Observe that a and q can be respectively seen as the ratio of the eigenenergy and the depth of the lattice to the recoil energy of the lattice laser (→ Sec. 2.3.)

In the following, we follow the notation of Meixner and Schäfke [99], except that we use a and q instead of λ and h^2, respectively. Exploiting the periodicity of the modulation in the Mathieu equation, we apply Bloch's theorem in solid state physics, or equivalently, Floquet's theorem in the theory of differential equations, which restricts forms of its solutions. Those theorem states that, for the fixed values of a and $q > 0$[*7], the equation has complex-valued solutions $\mathrm{me}_{\pm\nu}(z)$ called the *Floquet solutions* which have the form of

$$\mathrm{me}_{\pm\nu}(z) \equiv \mathrm{me}_{\pm\nu}(z; a, q) = e^{\pm i\nu z}u_\nu(z). \tag{A.55}$$

Here, ν is a function of a and q called the *characteristic exponent* (also known as the *crystal momentum* or the *quasimomentum* in the field of solid state physics; see Ashcroft and Mermin [101, Ch. 8],) and $u_\nu(z)$ is a periodic complex-valued function with period π which corresponds to the *Bloch function*, and can be determined only up to a multiplicative factor. The periodicity of $u_\nu(z)$ can be understood to originate from that of the modulation $2q\cos(2z)$. The imaginary part of the characteristic exponent determines the *stability* of the Floquet solution, and thus has been subject to intense research by mathematicians. See, *e.g.*, Sträng [102] for algorithms to compute it. Its implementation by Jones [1] in C language yields Figure A.5 which shows regions in the a-q plane corresponding to the real ν and hence stability of the Floquet solution (Contours shows the iso-ν points.) The blank region corresponds to complex ν (instability of the Floquet solution.) We can observe that, in the context of a classical particle moving in a modulated potential, strong parametric heatings occur at $a = \pm n^2$ for an integer n; that is, the minimal value for the strength q of the potential leading to the stable orbit of the particle approaches zero under such a condition.

As with the case of linear second-order differential equations, one can choose two independent solutions (a *basis* of the solution space) such that general solutions of the Mathieu equation can be obtained by

[*7] The case of $q < 0$ is easily handled by substitution of z with $z + \pi/2$; $2q\cos[2(z+\pi/2)] = -2q\cos(2z)$. The trivial case of $q = 0$ is omitted.

linear combination of them. Except for the special case in which $e^{\pm i\pi\nu}$ is either 1 or -1 (which respectively corresponds to $\nu = 2n$ or $2n+1$ for an integer n,) we can choose $\{\mathrm{me}_\nu(z), \mathrm{me}_{-\nu}(z) = \mathrm{me}_\nu(-z)\}$ for the basis. Alternatively, two real-valued functions called the *Mathieu* (or *elliptic*) *cosine* $y_{\mathrm{I}}(z)$ and *sine* $y_{\mathrm{II}}(z)$ may be chosen[*8]. They are characterized by the normalization conditions

$$y_{\mathrm{I}}(z=0) = 1, \qquad y'_{\mathrm{I}}(z=0) = 0, \tag{A.56a}$$

$$y_{\mathrm{II}}(z=0) = 0, \qquad y'_{\mathrm{II}}(z=0) = 1, \tag{A.56b}$$

and in fact, reduced to the corresponding trigonometic functions for the special case of $q = 0$:

$$y_{\mathrm{I}}(a, q=0; z) = \cos(\sqrt{a}z), \qquad y_{\mathrm{II}}(a, q=0; z) = \frac{\sin(\sqrt{a}z)}{\sqrt{a}}. \tag{A.57}$$

However, the Mathieu cosine and sine are generally not periodic in z. In fact, they can be related to the Floquet solutions by formulae such as

$$y_{\mathrm{I}} = \frac{1}{2}(\mathrm{me}_\nu + \mathrm{me}_{-\nu}). \tag{A.58}$$

There are countably many values of a (that depend on q; thus we may denote the n-th of them by $a_n(q)$ and $b_n(q)$,) leading to the special cases $e^{\pm i\pi\nu} = 0, 1$. Then $\mathrm{me}_\nu(z)$ and $\mathrm{me}_{-\nu}(z)$ coincides, have true periodicity or antiperiodicity with period π, and become an even or odd function, corresponding to $\nu = 2n$ or $2n+1$.

Mathematical analysis shows that $a_m(q) \sim b_{m+1}(q)$ when $q \to \infty$, *i.e.*, the m-th "allowed" energy range in the band structure gets narrower and narrower in the limit of a deep periodic potential (it indeed approaches a flat "band," which is obtained in the case of a simple harmonic oscillator.) However, there always remains a finite width for the m-th band which can be proven to be

$$b_{m+1}(q) - a_m(q) \sim \frac{2^{4m+5}}{m!}\sqrt{\frac{2}{\pi}}q^{m/2+3/4}e^{-4\sqrt{q}}\left(1 - \frac{6m^2+14m+7}{32\sqrt{q}}\right) \qquad (q \to \infty). \tag{A.59}$$

(A standard reference by Abramowitz and Stegun [103] cites Meixner and Schäfke [99] for this expression, though the latter only presents the result without a proof. The reader may found Dingle and Müller [104] and Liang and Müller-Kirsten [105] helpful.) Applying this expression to the spacial-domain Mathieu equation Eq. (A.53) for an optical lattice yields an approximated formula for the hopping matrix element J in the limit of deep lattice (See, *e.g.*, Bloch *et al.* [106, Sec. II.B])

$$\tilde{J} \sim \frac{4}{\sqrt{\pi}}(\tilde{U})^{3/4}\exp(-2\sqrt{\tilde{U}}) \qquad (\tilde{U} \to \infty). \tag{A.60}$$

Here, we wrote the formula in terms of the "normalized" energies by the recoil energy E_{rec}; $\tilde{J} \equiv J/E_{\mathrm{rec}}$ and $\tilde{U} \equiv U/E_{\mathrm{rec}}$. This formula is based on the fact that the hopping matrix element J for the atoms in the lowest band can be obtained from the width $W \equiv b_1 - a_0$ of the lowest ($m = 0$) band as $J = W/4$ (Jaksch [107, Sec. 7.2].) Then Eq. (A.60) immediately follows from substitution $q = U/(4E_{\mathrm{rec}})$[*9] and $m = 0$.

In addition to the rich mathematical literature on analytic properties of solutions of the Mathieu equation, we may utilize CAS (computer algebra systems) such as Mathematica and Maple which have built-in functions for the Mathieu functions, as well as the characteristic exponent.

[*8] Note that different parameter regions require different elements for a basis for the solution space. See Barrett [98] for details.

[*9] Forget about the sign of q! It is inessential, as explained in p. 56, *ft.*

Appendix B

Converter program from SPE image for WinView to JPEG image

It is convenient when the SPE image files obtained are shown in thumbnail list during a series of runs in which we change one of the parameters to ingestigate the dependence on the parameter. If we convert the SPE image to standard JPEG image, Windows Explorer or Microsoft Image Viewer can show them as thumnail image list. So we made a converter from SPE to JPEG.

Here we show the source code in Java. The program is in the public domain.

```
package spe2jpg;

import java.io.*; import java.util.*; import java.util.regex.*; import java.awt.*; import java.awt.event.*;
import java.awt.dnd.*; import java.awt.datatransfer.*; import java.awt.image.*; import javax.swing.*;
import javax.imageio.*; import javax.imageio.stream.*;

/**
 * @author NODA Kai
 */
public class Main extends JFrame {
    DropTargetAdapter dta;  JTextArea area;  static Pattern pat;

    /**
     * @param args the command line arguments
     */
    public static void main(String[] args) {
        if (args.length == 0) { new Main(); }
        else { convertAux(args, System.out); }
    }

    public Main() {
        super("SPE to JPG converter");
        setSize(new Dimension(600, 400));  setDefaultCloseOperation(JFrame.EXIT_ON_CLOSE);
        area = new JTextArea("Use Drag-and-Drop to convert SPE files.  "
+ "If you DnD a directory, its all entries are processed.\n"
+ "(Altenatively, you can specify files/directries with command-line arguments.)\n"
+ "Please note that, though the pseudo color used in this program looks almost same to that used in WinView, "
+ "they are a bit different.");
        area.setEditable(false);  area.setLineWrap(true);
        JScrollPane sp = new JScrollPane(area);  getContentPane().add(sp);
        dta = new DropTargetAdapterImpl();
        pat = Pattern.compile(".*\\.spe", Pattern.CASE_INSENSITIVE);
        setVisible(true);
    }

    /**
     * A method that does the actual work.
     * Refer to Appendix B of WinView 2.5 User Manual for the binary format of SPE file.
     * @param f  SPE file.
     * @throws java.io.FileNotFoundException
     */
    public static void convert(File f) throws FileNotFoundException {
        try {
            BufferedInputStream is = new BufferedInputStream(new FileInputStream(f));
            byte[] header = new byte[4100];  is.read(header);
            int xDim = ((0xff & header[43]) << 8) | (0xff & header[42]);
            int yDim = ((0xff & header[657]) << 8) | (0xff & header[656]);
            int frames = ((0xff & header[1449]) << 24) | ((0xff & header[1448]) << 16)
                        | ((0xff & header[1447]) << 8) | (0xff & header[1446]);
            int type = header[108];
            // System.out.printf("%d %d %d %d\n", xDim, yDim, frames, type);
            if (frames == 1) {
                byte[] raw = new byte[xDim * yDim * 8];  is.read(raw);
                BufferedImage img = new BufferedImage(xDim, yDim, BufferedImage.TYPE_INT_RGB);
                DataBufferInt db = (DataBufferInt) img.getRaster().getDataBuffer();
                for (int i = 0; i < xDim * yDim; ++i) {
                    long val = ((0xffL & raw[8 * i + 7]) << 56) | ((0xffL & raw[8 * i + 6]) << 48) |
                            ((0xffL & raw[8 * i + 5]) << 40) | ((0xffL & raw[8 * i + 4]) << 32) |
                            ((0xffL & raw[8 * i + 3]) << 24) | ((0xffL & raw[8 * i + 2]) << 16) |
                            ((0xffL & raw[8 * i + 1]) << 8) | (0xffL & raw[8 * i]);
                    // NOTE: Put your own scaling factor here (default: 1e3 == 1000)
                    db.setElem(i, pseudoColor(Double.longBitsToDouble(val) / 1e3));
                }
                Iterator writers = ImageIO.getImageWritersByFormatName("jpg");
                if (writers.hasNext()) {
                    ImageWriter iw = (ImageWriter) writers.next();
                    String origName = f.getAbsolutePath(), jpgName;
                    int pos = origName.lastIndexOf('.');
                    jpgName = origName.substring(0, pos >= 0 ? pos : origName.length()) + ".jpg";
                    ImageOutputStream ios = ImageIO.createImageOutputStream(new File(jpgName));
                    iw.setOutput(ios);  iw.write(img);  iw.dispose();  ios.close();
                }
            } else {
                for (int fi = 0; fi < frames; ++fi) { /* TODO: the case when there are multiple frames */ }
            }
        }
        catch (IOException ex) { ex.printStackTrace(); }
    }

    /**
     * This method is responsible for the pseudo-color.
     * You might well to change the constants to modify the color curve.
     * @param gray  gray-scale value.
     */
    static int pseudoColor(double gray) {
        gray = Math.min(Math.max(gray, 0), 1d);
        float h = 2f / 3 - (float) (Math.min(5d / 6 * gray, 2d / 3));
        float s = (float) (Math.min(15 * (gray - 1) * (gray - 1.1), 1));
        float b = (float) (0.4 + 3 * Math.min(gray, 0.2));
        return Color.HSBtoRGB(h, s, b);
```

```
    }

    static void convertAux(String[] paths, PrintStream out) {
        File[] files = new File[paths.length];
        for (int i = 0; i < paths.length; ++i) { files[i] = new File(paths[i]); }
        PseudoPrintStream pps = new PseudoPrintStream() {
            PrintStream strm;
            public void print(String s) { strm.print(s); }
            public void setDestination(Object o) { strm = (PrintStream) o; }
        };
        pps.setDestination(out);  convertAux2(files, pps);
    }

    static void convertAux(java.util.List<File> files, JTextArea area) {
        File[] arr = new File[files.size()];  int cnt = -1;
        for (File f : files) { arr[++cnt] = f; }
        PseudoPrintStream pps = new PseudoPrintStream() {
            JTextArea ta;
            public void print(String s) {
                ta.append(s);
                ta.setCaretPosition(ta.getText().length());
            }
            public void setDestination(Object o) { ta = (JTextArea) o; }
        };
        pps.setDestination(area);  SwingWorker worker = new SwingWorkerImpl(arr, pps);  worker.execute();
    }

    static void convertAux2(File[] files, PseudoPrintStream out) {
        try {
            for (File f : files) {
                if (f.isDirectory()) {
                    out.print("\n");
                    File[] entries = f.listFiles();
                    for (File e : entries) {
                        if (pat.matcher(e.getName()).matches()) {
                            out.print("\nConverting " + f.getName() + "/" + e.getName() + "...");
                            convert(e);  out.print(" done.");
                        }
                    }
                } else {
                    if (pat.matcher(f.getName()).matches()) {
                        out.print("\nConverting " + f.getName() + "...");
                        convert(f);  out.print(" done.");
                    }
                }
            }
        }
        catch (Exception ex) { ex.printStackTrace(); }
    }

    private class DropTargetAdapterImpl extends DropTargetAdapter {
        public DropTargetAdapterImpl() {
            DropTarget target = new DropTarget(area, DnDConstants.ACTION_COPY_OR_MOVE, this, true);
        }

        @Override
        public void dragEnter(DropTargetDragEvent e) { e.acceptDrag(DnDConstants.ACTION_COPY_OR_MOVE); }

        public void drop(DropTargetDropEvent e) {
            e.acceptDrop(DnDConstants.ACTION_COPY_OR_MOVE);
            try {
                if ((e.getDropAction() & DnDConstants.ACTION_COPY_OR_MOVE) != 0) {
                    Transferable tr = e.getTransferable();
                    java.util.List<File> lst =
                        (java.util.List<File>) tr.getTransferData(DataFlavor.javaFileListFlavor);
                    convertAux(lst, area);  e.dropComplete(true);
                } else { e.dropComplete(false); }
            }
            catch (Exception ex) { ex.printStackTrace(); e.dropComplete(false); }
        }
    }

    private interface PseudoPrintStream {
        public void print(String s);
        public void setDestination(Object o);
    }

    private static class SwingWorkerImpl extends SwingWorker {
        private final File[] arr;  private final PseudoPrintStream pps;

        public SwingWorkerImpl(File[] arr, PseudoPrintStream pps) {
            this.arr = arr;  this.pps = pps;
        }

        @Override
        protected Object doInBackground() throws Exception {
            convertAux2(arr, pps);  return null;
        }
    }
}
```

Bibliography

[1] T. Jones, *Mathieu's Equations and the Ideal rf-Paul Trap* (2008), accesssible at `http://www.physics.drexel.edu/~tim/`.

[2] M. H. Anderson, J. R. Ensher, M. R. Matthews, C. E. Wieman, and E. A. Cornell, "Observation of Bose-Einstein condensation in a dilute atomic vapor," Science **269**, 198 (1995).

[3] K. B. Davis, M.-O. Mewes, M. R. Andrews, N. J. van Druten, D. S. Durfee, D. M. Kurn, and W. Ketterle, "Bose-Einstein condensation in a gas of sodium atoms," Phys. Rev. Lett. **75**, 3969 (1995).

[4] C. C. Bradley, C. A. Sackett, J. J. Tollett, and R. G. Hulet, "Evidence of Bose-Einstein Condensation in an atomic gas with attractive interactions," Phys. Rev. Lett. **75**, 1687 (1995).

[5] L. S. Feuer, *Einstein and the Generations of Science* (Transaction Publishers, 1989), 2nd ed.

[6] R. A. Millikan, *The Autobiography of Robert Millikan* (Prentice-Hall, 1950).

[7] L. Brown, A. Pais, and B. Pippard, eds., *Twentieth Century Physics*, vol. I–III (Taylor & Francis, 1995), 2nd ed.

[8] A. J. Leggett, *Quantum Liquids: Bose Condensation and Cooper Pairing in Condensed-Matter Systems* (Oxford University Press, 2006).

[9] D. Pines, *The Many-Body Problem: a Lecture Note and Reprint Volume* (Benjamin, 1962), 2nd ed.

[10] P. Nozières, *Theory of Interacting Fermi Systems* (Benjamin, 1964).

[11] P. Nozières and D. Pines, *Normal Fermi Liquids*, vol. 1 of *The Theory of Quantum Liquids* (Benjamin, 1966).

[12] L. Tonks, "The complete equation of state of one, two and three-dimensional gases of hard elastic spheres," Phys. Rev. **50**, 955 (1936).

[13] M. Girardeau, "Relationship between systems of impenetrable bosons and fermions in one dimension," J. Math. Phys. **1**, 516 (1960).

[14] H. Tasaki, "The Hubbard model—an introduction and selected rigorous results," J. Phys.: Condens. Matter **10**, 4353 (1998).

[15] B. Baumgartner, "The existence of many-particle bound states despite a pair interaction with positive scattering length," J. Phys. A: Math. Gen. **30**, L741 (1997).

[16] D. Kleppner, T. J. Greytak, T. C. Killian, D. G. Fried, L. Willmann, D. Landhuis, and S. C. Moss, "Bose-Einstein condensation of atomic hydrogen," arXiv:physics/9812038 (1998).

[17] W. C. Stwalley and L. H. Nosanow, "Possible 'new' quantum systems," Phys. Rev. Lett. **36**, 910 (1976).

[18] T. W. Hänsch and A. L. Schawlow, "Cooling of gases by laser radiation," Opt. Comm. **13**, 68 (1975).

[19] D. Wineland and H. Dehmelt, "Proposed $10^{14}\Delta\nu < \nu$ laser fluorescence spectroscopy on Tl^+ mono-ion oscillator III (side band cooling)," Bull. Am. Phys. Soc. **20**, 637 (1975).

[20] E. L. Raab, M. Prentiss, A. Cable, S. Chu, and D. E. Pritchard, "Trapping of neutral sodium atoms with radiation pressure," Phys. Rev. Lett. **59**, 2631 (1987).

[21] H. J. Metcalf and P. van der Straten, *Laser Cooling and Trapping*, Graduate Texts in Contemporary Physics (Springer, 1999).

[22] J. Weiner, "Cold collisions, quatum degenerate gases, photoassociation, and cold molecules," in *Low Temperatures and Cold Molecules*, edited by I. W. M. Smith (Imperial College Press, 2008).

[23] H. F. Hess, "Evaporative cooling of magnetically trapped and compressed spin-polarized hydrogen," Phys. Rev. B **34**, 3476 (1986).

[24] N. Masuhara, J. M. Doyle, J. C. Sandberg, D. Kleppner, T. J. Greytak, H. F. Hess, and G. P. Kochanski, "Evaporative cooling of spin-polarized atomic hydrogen," Phys. Rev. Lett. **61**, 935 (1988).

[25] D. G. Fried, T. C. Killian, L. Willmann, D. Landhuis, S. C. Moss, D. Kleppner, and T. J. Greytak, "Bose-Einstein condensation of atomic hydrogen," Phys. Rev. Lett. **81**, 3811 (1998).

[26] T. Weber, J. Herbig, M. Mark, H.-Ch. Nägerl, and R. Grimm, "Bose-Einstein condensation of cesium," Science **299**, 232 (2003).

[27] C. Chin, V. Vuletić, A. J. Kerman, and S. Chu, "High resolution Feshbach spectroscopy of cesium," Phys. Rev. Lett. **85**, 2717 (2000).

[28] J. Terrien, "News from the International Bureau of Weights and Measures," Metrologia **4**, 41 (1968).

[29] G. Roati, M. Zaccanti, C. D'Errico, J. Catani, M. Modugno, A. Simoni, M. Inguscio, and G. Modugno, "^{39}K Bose-Einstein condensate with tunable interactions," Phys. Rev. Lett. **99**, 010403 (2007).

[30] C. D'Errico, M. Zaccanti, M. Fattori, G. Roati, M. Inguscio, G. Modugno, and A. Simoni, "Feshbach resonances in ultracold ^{39}K," New J. Phys. **9**, 223 (2007).

[31] C. C. Bradley, C. A. Sackett, and R. G. Hulet, "Bose-Einstein condensation of lithium: observation of limited condensate number," Phys. Rev. Lett. **78**, 985 (1997).

[32] A. Robert, O. Sirjean, A. Browaeys, J. Poupard, S. Nowak, D. Boiron, C. I. Westbrook, and A. Aspect, "A Bose-Einstein condensate of metastable atoms," Science **292**, 461 (2001).

[33] G. Modugno, G. Ferrari, G. Roati, R. J. Brecha, A. Simoni, and M. Inguscio, "Bose-Einstein condensation of potassium atoms by sympathetic cooling," Science **294**, 1320 (2001).

[34] Y. Takasu, K. Maki, K. Komori, T. Takano, K. Honda, M. Kumakura, T. Yabuzaki, and Y. Takahashi, "Spin-singlet Bose-Einstein condensation of two-electron atoms," Phys. Rev. Lett. **91**, 040404 (2003).

[35] A. Griesmaier, J. Werner, S. Hensler, J. Stuhler, and T. Pfau, "Bose-einstein condensation of chromium," Phys. Rev. Lett. **94**, 160401 (2005).

[36] T. Fukuhara, S. Sugawa, and Y. Takahashi, "Bose-Einstein condensation of an ytterbium isotope," Phys. Rev. A **76**, 051604(R) (2007).

[37] B. DeMarco and D. Jin, "Onset of Fermi degeneracy in a trapped atomic gas," Science **285**, 1703 (1999).

[38] A. G. Truscott, K. E. Strecker, W. I. McAlexander, G. B. Partridge, and R. G. Hulet, "Observation of Fermi pressure in a gas of trapped atoms," Science **291**, 2570 (2001).

[39] K. Xu, T. Mukaiyama, J. R. Abo-Shaeer, J. K. Chin, D. E. Miller, and W. Ketterle, "Formation of quantum-degenerate sodium molecules," Phys. Rev. Lett. **91**, 210402 (2003).

[40] M. Greiner, C. A. Regal, and D. S. Jin, "Emergence of a molecular Bose-Einstein condensate from a Fermi gas," Nature **426**, 537 (2003).

[41] K. E. Strecker, G. B. Partridge, A. G. Truscott, and R. G. Hulet, "Formation and propagation of matter-wave soliton trains," Nature **417**, 150 (2002).

[42] L. Khaykovich, F. Schreck, G. Ferrari, T. Bourdel, J. Cubizolles, L. D. Carr, Y. Castin, and C. Salomon, "Magnetic field control of elastic scattering in a cold gas of fermionic lithium atoms," Science **296**, 1290 (2002).

[43] S. Inouye, M. R. Andrews, J. Stenger, H.-J. Miesner, D. M. Stamper-Kurn, and W. Ketterle, "Observation of Feshbach resonances in a Bose-Einstein condensate," Nature **391**, 151 (1998).

[44] J. L. Roberts, N. R. Claussen, J. P. Burke, Jr., C. H. Greene, E. A. Cornell, and C. E. Wieman, "Resonant magnetic field control of elastic scattering in cold ^{85}Rb," Phys. Rev. Lett. **81**, 5109 (1998).

[45] A. Marte, T. Volz, J. Schuster, S. Dürr, G. Rempe, E. G. M. van Kempen, and B. J. Verhaar, "Feshbach resonances in rubidium 87: Precision measurement and analysis," Phys. Rev. Lett. **89**, 283202 (2002).

[46] J. Werner, A. Griesmaier, S. Hensler, J. Stuhler, T. Pfau, A. Simoni, and E. Tiesinga, "Observation of Feshbach resonances in an ultracold gas of ^{52}Cr," Phys. Rev. Lett. **94**, 183201 (2005).

[47] T. Kishimoto, J. Kobayashi, K. Noda, K. Aikawa, M. Ueda, and S. Inouye, "Direct evaporative cooling of ^{41}K into a Bose-Einstein condensate," Phys. Rev. A (2009), in preparation.

[48] S. Jochim, M. Bartenstein, G. Hendl, J. Hecker Denschlag, R. Grimm, A. Mosk, and M. Weidemüller, "Magnetic field control of elastic scattering in a cold gas of fermionic lithium atoms," Phys. Rev. Lett. **89**, 273202 (2002).

[49] T. Loftus, C. A. Regal, C. Ticknor, J. L. Bohn, and D. S. Jin, "Resonant control of elastic collisions in an optically trapped Fermi gas of atoms," Phys. Rev. Lett. **88**, 173201 (2002).

[50] C. A. Regal, C. Ticknor, J. L. Bohn, and D. S. Jin, "Tuning p-wave interactions in an ultracold Fermi gas of atoms," Phys. Rev. Lett. **90**, 053201 (2003).

[51] S. B. Papp and C. E. Wieman, "Observation of heteronuclear Feshbach molecules from a ^{85}Rb–^{87}Rb gas," Phys. Rev. Lett. **97**, 180404 (2006).

[52] C. Marzok, B. Deh, C. Zimmermann, P. W. Courteille, E. Tiemann, Y. V. Vanne, and A. Saenz, "Feshbach resonances in an ultracold ^{7}Li and ^{87}Rb mixture," Phys. Rev. A **79**, 012717 (2009).

[53] E. Wille, F. M. Spiegelhalder, G. Kerner, D. Naik, A. Trenkwalder, G. Hendl, F. Schreck, R. Grimm, T. G. Tiecke, J. T. M. Walraven, S. J. J. M. F. Kokkelmans, E. Tiesinga, and P. S. Julienne, "Exploring an ultracold fermi-fermi mixture: interspecies Feshbach resonances and scattering properties of ^{6}Li and ^{40}K," Phys. Rev. Lett. **100**, 053201 (2008).

[54] K. I. Petsas, A. B. Coates, and G. Grynberg, "Crystallography of optical lattices," Phys. Rev. A **50**, 5173 (1994).

[55] P. S. Jessen and I. H. Deutsch, "Optical lattices," in *Advances in Atomic, Molecular and Optical Physics*, edited by B. Bederson and H. Walther (Academic Press, 1996), vol. 37.

[56] P. B. Blakie and C. W. Clark, "Wannier states and Bose-Hubbard parameters for 2D optical lattices," J. Phys. B: At. Mol. Opt. Phys. **37**, 1391 (2004).

[57] G. Grynberg and C. Robilliard, "Cold atoms in dissipative optical lattices," Phys. Rep. **355**, 335 (2001).

[58] L. Guidoni and P. Verkerk, "Optical lattices: cold atoms ordered by light," J. Opt. B: Quantum Semiclass. Opt. **1**, R23 (1999).

[59] R. Grimm, M. Weidemüller, and Y. B. Ovchinnikov, "Optical dipole traps for neutral atoms," arXiv: physics/9902072 (1999).

[60] D. A. Steck, *Rubidium 87 D Line Data (ver. 2.1)* (2008), accesssible at `http://steck.us/alkalidata/`.

[61] M. E. Gehm, *Properties of ^{6}Li* (2003), accesssible at `http://www.phy.duke.edu/research/photon/qoptics/`.

[62] L. J. LeBlanc, *Hyperfine structure of ^{40}K* (2006), accesssible at `http://www.physics.utoronto.ca/~jhtgroup/`.

[63] Y. Ralchenko, A. E. Kramida, J. Reader, and NIST ASD Team, *NIST Atomic Spectra Database Version 3.1.5* (2008), accesssible at `http://physics.nist.gov/asd3`.

[64] E. Hecht and A. Zajac, *Optics* (Addison Wesley, 2001), 4th ed.

[65] R. E. Sapiro, R. Zhang, and G. Raithel, "Reversible loss of superfluidity of a Bose-Einstein condensate in a 1D optical lattice," New J. Phys. **11**, 013013 (2009).

[66] R. Zhang, R. E. Sapiro, N. V. Morrow, R. R. Mhaskar, and G. Raithel, "Bose-einstein condensate inside a bragg-reflecting atom cavity," Phys. Rev. A **77**, 063615 (2008).

[67] Z. Hadzibabic, S. Stock, B. Battelier, V. Bretin, and J. Dalibard, "Interference of an array of independent Bose-Einstein condensates," Phys. Rev. Lett. **93**, 180403 (2004).

[68] F. Gerbier, S. Trotzky, S. Fölling, U. Schnorrberger, J. D. Thompson, A. Widera, I. Bloch, L. Pollet, M. Troyer, B. Capogrosso-Sansone, N. V. Prokof'ev, and B. V. Svistunov, "Expansion of a quantum gas released from an optical lattice," Phys. Rev. Lett. **101**, 155303 (2008).

[69] M. Greiner, "Ultracold quantum gases in three-dimensional optical lattice potentials," Ph.D. thesis, Ludwig-Maximilians-Universität München (2003), accesssible at `http://greiner.physics.harvard.edu/`.

[70] J. Weiner, *Cold and Ultracold Collisions in Quantum Microscopic and Mesoscopic Systems* (Cambridge University Press, 2003).

[71] S. Falke, H. Knöckel, J. Friebe, M. Riedmann, E. Tiemann, and Ch. Lisdat, "Potassium ground-state scattering parameters and Born-Oppenheimer potentials from molecular spectroscopy," Phys. Rev. A **78**, 012503 (2008).

[72] A. D. Lange, K. Pilch, A. Prantner, F. Ferlaino, B. Engeser, H.-C. Nägerl, R. Grimm, and C. Chin, "Determination of atomic scattering lengths from measurements of molecular binding energies near Feshbach resonances," Phys. Rev. A **79**, 013622 (2009).

[73] K. M. Jones, E. Tiesinga, P. D. Lett, and P. S. Julienne, "Ultracold photoassociation spectroscopy: long-range molecules and atomic scattering," Rev. Mod. Phys. **78**, 483 (2006).

[74] W. C. Stwalley and H. Wang, "Photoassociation of ultracold atoms: a new spectroscopic technique (special review lecture)," J. Mol. Spec. **195**, 194 (1999).

[75] W. C. Stwalley, Y.-H. Uang, and G. Pichler, "Pure long-range molecules," Phys. Rev. Lett. **41**, 1164 (1978).

[76] A. Chambers, R. K. Fitch, and B. S. Halliday, *Basic Vacuum Technology* (CRC Press, 1998).

[77] K. Aikawa, "Preparation of ultracold atomic sources towards ground state polar molecules," Master's thesis, The University of Tokyo (2008), accesssible at `http://ultracold.t.u-tokyo.ac.jp/`.

[78] W. H. Wing, "On neutral particle trapping in quasistatic electromagnetic fields," Prog. Quant. Electron. **8**, 181 (1984).

[79] D. E. Pritchard, "Cooling neutral atoms in a magnetic trap for precision spectroscopy," Phys. Rev. Lett. **51**, 1336 (1983).

[80] D. M. Stamper-Kurn, "Peeking and poking at a new quantum fluid: studies of gaseous Bose-Einstein condensates in magnetic and optical traps," Ph.D. thesis, Massachusetts Institute of Technology (2000), accesssible at `http://cua.mit.edu/ketterle_group/Theses/`.

[81] H. J. Lewandowski, D. M. Harber, D. L. Whitaker, and E. A. Cornell, "Simplified system for creating a Bose-Einstein condensate," J. Low. Temp. Phys. **132**, 309 (2003).

[82] W. Ketterle and N. J. van Druten, "Evaporative cooling of trapped atoms," Adv. Atom. Mol. Opt. Phys. **37**, 181 (1996), accesssible at `http://cua.mit.edu/ketterle_group/`.

[83] J. P. Burke, J. L. Bohn, B. D. Esry, and C. H. Greene, "Impact of the ^{87}Rb singlet scattering length on suppressing inelastic collisions," Phys. Rev. A **55**, R2511 (1997).

[84] J. Burke, James Patrick, "Theoretical investigation of cold alkali atom collisions," Ph.D. thesis, University of Colorado (1999), accesssible at `http://jilawww.colorado.edu/pubs/thesis/burke/`.

[85] P. J. Mohr, B. N. Taylor, and D. B. Newel, "CODATA recommended values of the fundamental physical constants: 2006," Rev. Mod. Phys. **80**, 633 (2008), accesssible at `http://physics.nist.gov/cuu/Constants/`.

[86] M. P. Bradley, J. V. Porto, S. Rainville, J. K. Thompson, and D. E. Pritchard, "Penning trap measurements of the masses of ^{133}Cs, ^{87,85}Rb, and ^{23}Na with uncertainties ≤ 0.2 ppb," Phys. Rev. Lett. **83**, 4510 (1999).

[87] *WinX/32 Automation 3.X for VB User Manual* (????), accesssible at `http://ftp.roperscientific.com/Public/Software/Examples/WinX32_Automation/`.

[88] E. W. Streed, A. P. Chikkatur, T. L. Gustavson, M. Boyd, Y. Torii, D. Schneble, G. K. Campbell, D. E. Pritchard, , and W. Ketterle, "Large atom number Bose-Einstein condensate machines," Rev. Sci. Instrum. **77**, 023106 (2006).

[89] W. Petrich, M. H. Anderson, J. R. Ensher, and E. A. Cornell, "Behavior of atoms in a compressed magneto-optical trap," J. Opt. Soc. Am. B **11**, 1332 (1994).

[90] M. Greiner, O. Mandel, T. Esslinger, T. W. Hänsch, and I. Bloch, "Quantum phase transition from a superfluid to a Mott insulator in a gas of ultracold atoms," Nature **415**, 39 (2002).

[91] A. Yariv, *Quantum Electronics* (Wiley, 1989), 3rd ed.

[92] R. P. Feynman, *Statistical Mechanics: A Set of Lectures* (Addison-Wesley, 1981).

[93] H. Matano and M. Jimbo, *Heat, Waves and Differential Equations*, Introduction to Modern Mathematics (Iwanami Shoten, 2004), in Japanese.

[94] L. Ahlfors, *Complex Analysis* (McGraw-Hill, 1979), 3rd ed.

[95] M. Spiegel, *Schaum's Outlines: Complex Variables (with an Introduction to Conformal Mapping and Its Applications)* (McGraw-Hill, 1964).

[96] C. Wittig, "The Landau-Zener formula," J. Phys. Chem. B **109**, 8428 (2005).

[97] H. Sin, "Ch. XIV: Special functions," in *Encyclopedic Dictionary of Mathematics: The Mathematical Society of Japan*, edited by K. Ito (The MIT Press, 1993), vol. II, 2nd ed.

[98] W. Barrett, "Mathieu functions of general order: Connection formulae, base functions and asymptotic formulae: I–V," Phil. Trans. R. Soc. Lond. A **301**, 75 (1981).

[99] J. Meixner and F. W. Schäfke, *Mathieusche Functionen und Sphäroidfunktionen, mit Anwendungen auf Physikalische und Technische Probleme*, vol. LXXI of *Die Grundlehren der Mathematischen Wissenchaften* (Springer-Verlag, 1954), in German.

[100] E. Mathieu, "Mémoire sur le mouvement vibratoire d'une membrane de forme elliptique," Journal des Mathématiques Pures et Appliquées **13**, 137 (1868).

[101] N. W. Ashcroft and N. D. Mermin, *Solid State Physics* (Thomson Brooks/Cole, 1976).

[102] J. E. Sträng, "On the characteristic exponents of Floquet solutions to the Mathieu equation," Bull. Cl. Sci. Acad. R. Belg. **6**, 269 (2005), accessible as Ulm report ULM-TP/05-4 at `http://www.physik.uni-ulm.de/theo/qc/`, or arXiv:math-ph/0510076.

[103] M. Abramowitz and I. Stegun, eds., *Handbook of Mathematical Functions with Formulas, Graphs, and Mathematical Tables* (Dover, 1964).

[104] R. B. Dingle and H. J. W. Müller, "The form of the coefficients of the late terms in asymptotic expansions of the characteristic numbers of Mathieu and spheriodal-wave functions," J. reine angew. Math. **216**, 123 (1964).

[105] J.-Q. Liang and H. J. W. Müller-Kirsten, "Anharmonic oscillator equations: treatment parallel to Mathieu equation," arXiv:quant-ph/0407235 (2004).

[106] I. Bloch, J. Dalibard, and W. Zwerger, "Many-body physics with ultracold gases," Rev. Mod. Phys. **80**, 885 (2008).

[107] D. Jaksch, "Bose-Einstein condensation and applications," Ph.D. thesis, Leopold-Franzens-Universität Innsbruck (1999), accesssible at `http://www.physics.ox.ac.uk/qubit/`.